

REPORT DOCUMENTATION PAGE

Form Approved
OMB No. 0704-0188

Public reporting burden for this collection of information is estimated to average 1 hour per response, including the time for reviewing instructions, searching existing data sources, gathering and maintaining the data needed, and completing and reviewing this collection of information. Send comments regarding this burden estimate or any other aspect of this collection of information, including suggestions for reducing this burden to Department of Defense, Washington Headquarters Services, Directorate for Information Operations and Reports (0704-0188), 1215 Jefferson Davis Highway, Suite 1204, Arlington, VA 22202-4302. Respondents should be aware that notwithstanding any other provision of law, no person shall be subject to any penalty for failing to comply with a collection of information if it does not display a currently valid OMB control number. **PLEASE DO NOT RETURN YOUR FORM TO THE ABOVE ADDRESS.**

1. REPORT DATE (DD-MM-YYYY) August 28, 2006		2. REPORT TYPE FINAL Technical Report		3. DATES COVERED (From - To) 1 July 2000 - 30 June 2006	
4. TITLE AND SUBTITLE MURI 2000: "Phonon Enhancement of Optoelectronic and Electronic Devices				5a. CONTRACT NUMBER	
				5b. GRANT NUMBER F49620-00-1-0331	
				5c. PROGRAM ELEMENT NUMBER	
6. AUTHOR(S) G. Belenky (Stony Brook), Q. Hu (MIT), S. Luryi (Stony Brook), H. Maris (Brown), A. Nurmikko (Brown), S-S S. Pei (U. of Houston) and A. Zaslavsky (Brown)				5d. PROJECT NUMBER	
				5e. TASK NUMBER	
				5f. WORK UNIT NUMBER	
7. PERFORMING ORGANIZATION NAME(S) AND ADDRESS(ES) Brown University Center for Advanced Materials Research Box M Providence, RI 02912				8. PERFORMING ORGANIZATION REPORT NUMBER	
9. SPONSORING / MONITORING AGENCY NAME(S) AND ADDRESS(ES) LtCol Todd D. Steiner, PhD Program Manager, Physics and Electronics 4015 Wilson Blvd Arlington VA 22203 Tel: 703 696 7314 todd.steiner@afosr.af.mil				10. SPONSOR/MONITOR'S ACRONYM(S)	
				11. SPONSOR/MONITOR'S REPORT NUMBER(S)	
12. DISTRIBUTION / AVAILABILITY STATEMENT Approved for Public release; distribution unlimited					
13. SUPPLEMENTARY NOTES					
14. ABSTRACT This MURI program began with the premise that extensive opportunities exist to transform the problems generally associated with phonons presenting an overhead into a distinct benefit for substantial enhancement of a broad range of optoelectronic and electronic devices. Our explicit goal and objective is to provide a significant improvement and major technological impact to the performance of a wide spectrum of advanced and novel semiconductor optoelectronic/electronic devices, by explicitly focusing on the role of phonon assisted and phonon dominated processes that control the functionality and applications of such devices. The devices range from quantum cascade and intersubband mid-IR lasers to new THz frequency laser sources, from semiconductor lasers in the blue and near ultraviolet to high power microwave FETs, to novel ultrahigh speed bipolar tunneling transistors. Additionally, new physical phenomena is being studied in which electron-electron interaction, crucial for ballistic and coherent electronic devices, is spectroscopically characterized via the electron-phonon interaction. The multi-university team was organized specifically to integrate a potent core of scientific expertise in phonon science, both experiment and theory in terms of the interaction of phonons with the electronic degrees of freedom in semiconductor nanostructures and high speed, high power devices.					
15. SUBJECT TERMS					
16. SECURITY CLASSIFICATION OF: Unclassified			17. LIMITATION OF ABSTRACT	18. NUMBER OF PAGES 19	Arto V. Nurmikko
a. REPORT	b. ABSTRACT	c. THIS PAGE			19b. TELEPHONE NUMBER (include area code) (401) 863-2869

Phonon Enhancement of Electronic and Optoelectronic Devices

Final Project Report

Prepared for:

Air Force Office of Scientific Research

Grant # F49620-00-1-0331

July 1, 2000 – June 30, 2005

Submitted to:

DISTRIBUTION STATEMENT A
Approved for Public Release
Distribution Unlimited

Optoelectronic Materials Program
Physics and Electronics Directorate
Air Force Office of Scientific Research
801 N. Randolph Street
Arlington, VA 22203-1977

By

A. V. Nurmikko, Principal Investigator
Division of Engineering, Brown University
Providence, RI 02912
Tel: 401-863-1418 FAX: 401-863-9025
e-mail: Arto_Nurmikko@brown.edu

co-participants:

Prof. G. Belenky, University at Stony Brook
Prof. Qing Hu, Massachusetts Institute of Technology
Prof. S. Luryi, University at Stony Brook
Prof. H. Maris, Brown University
Prof. A. Zaslavsky, Brown University

December 2006

Phonon Enhancement of Electronic and Optoelectronic Devices

Final Project Report

TABLE OF CONTENTS

1. OBJECTIVES	1
2. FINAL STATUS OF EFFORT_.....	2
3. ACCOMPLISHMENTS/NEW FINDINGS_.....	2
Team Highlights and Synergy	2
Task #1 Phonon Engineering for the Development of Terahertz Lasers Based On Intersubband Transitions Project Leader: Qing Hu (MIT).....	4
Task #2 Intersubband Lasers and Phonon Assisted Subband Depopulation Project Leaders: Gregory Belenky and S. Luryi (Stony Brook).....	13
Task #3 Phonon Enhancement To Carrier Transport In Interband Cascade Lasers Project Leader: Shin-Shem Steven Pei (U. of Houston).....	37
Task #4 Silicon Technology Compatible Devices Based on Phonon-Assisted Tunneling Project Leader: A. Zaslavsky (Brown).....	80
Task #5 Gallium Nitride FETs – Strain, Giant Piezoelectric Fields, Electronic Confinement and Coherent Phonons Project Leader: Arto Nurmikko (Brown).....	92
Task #6 Phonons and Nonthermal Cooling In Heterostructure Devices Project Leader: Humphrey Maris (Brown).....	96
4 PERSONNEL SUPPORTED.....	100
5 REFERENCES CITED.....	103
6 PUBLICATIONS & BOOK CHAPTERS.....	106
7 INTERACTIONS/TRANSITIONS.....	111
8 NEW DISCOVERIES, INVENTIONS, PATENTS (PENDING)	113
9 HONORS/AWARDS.....	113

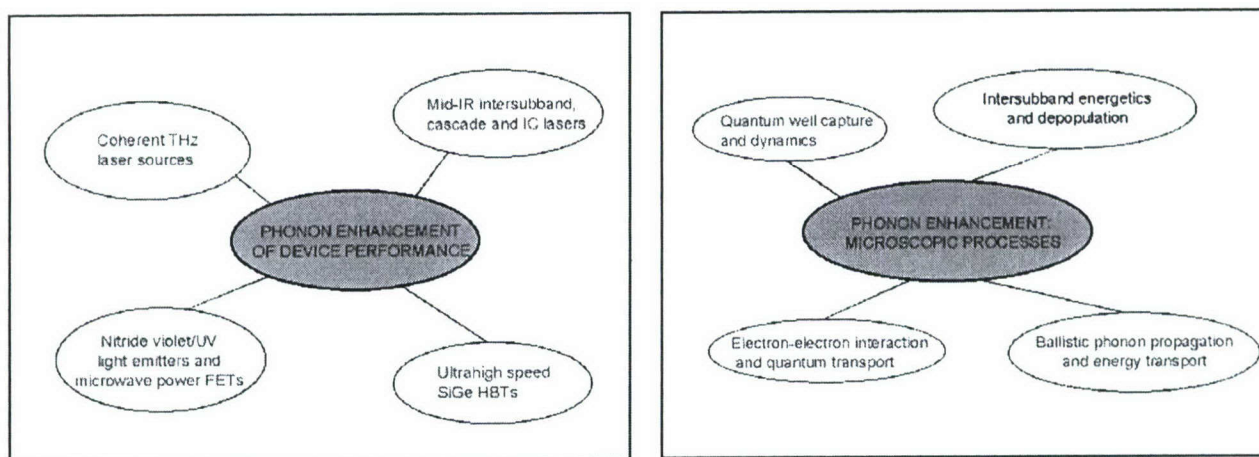


Figure 1. Left: phonon enhancement in strategic heterostructures devices; Right: key

1. OBJECTIVES

This MURI program began with the premise that extensive opportunities exist to transform the problems generally associated with phonons presenting a lossy overhead into a distinct benefit for substantial enhancement of a broad range of optoelectronic and electronic devices. Our explicit goal and objective was to provide a significant improvement and major technological impact to the performance of a wide spectrum of advanced and novel semiconductor optoelectronic/electronic devices, by explicitly focusing on the role of phonon assisted and phonon dominated processes that control the functionality and applications of such devices. The devices ranged from quantum cascade and intersubband mid-IR lasers to new THz frequency laser sources, from semiconductor lasers in the blue and near ultraviolet to high power microwave FETs, to novel ultrahigh speed bipolar tunneling transistors. Additionally, new physical phenomena was studied in which electron-electron interaction, crucial for ballistic and coherent electronic devices, was spectroscopically characterized via the electron-phonon interaction. The multiuniversity team was organized specifically to integrate a potent core of scientific expertise in phonon science, both experiment and theory in terms of the interaction of phonons with the electronic degrees of freedom in semiconductor nanostructures and high speed, high power devices.

The scientific strategy for the program is schematically sketched in Figure 1. The left panel shows the pivotal role of the phonon enhancement processes for the optoelectronic and electronic devices which formed the technological backbone of the program. The right panel identifies the core group of microscopic physical processes for the basic science component of the program. The team pursued two different testbed outlays in applying sophisticated experimental and theoretical tools to the problem areas identified in Figure 1. First, we pursued the growth, synthesis, and nanofabrication of the types of specifically tailored lower dimensional heterostructures where the phonon enhancement issues can be systematically studied. Secondly, in close collaboration with industrial partners, we investigated the incorporation and implementation of the phonon enhancement processes to real optoelectronic and electronic device structures. Advanced experimental probes and device physics modeling was performed

for identifying the microscopies of the impact of the phonon enhancement to these high performance devices.

2. FINAL STATUS OF EFFORT

This project started on July 1, 2000. During the first twelve months, the subcontracts were established and graduate students as well as post-doctoral associates were sought and some hired by the various investigators. The subsequent years were devoted to intense team-oriented research. In addition to internal research exchanges and reviews, the team participated several times in the joint review of the Brown University and U. of Michigan led MURI teams, alternating between Ann Arbor, Michigan and Providence RI. Active and successful research emerged from the MURI team effort, towards the stated objectives. The MURI team accomplished a number of important scientific discoveries which have created considerable new insight to 'phonon engineering' and new/improved optoelectronic and microelectronic devices. These advances are summarized next.

3. ACCOMPLISHMENTS/NEW FINDINGS

In this section we describe the scientific progress and accomplishments achieved by the MURI team by first describing the whole team synergy and then summarizing results from each of the program technical thrust areas.

Team Highlights and Synergy:

The main objective of the MURI team was to provide significant improvements and impact to the performance of several categories of semiconductor-based optoelectronic and microelectronic, by controlling and focusing on the role of phonon assisted and phonon dominated processes that either limited or dictated the functionality of such devices. The very rationale of the team composition was initially selected to include expertise from basic semiconductor physics to applied device sciences to phonon specialists. At the same time, we focused selectively on a very diverse set of device candidates, in an attempt to reach meaningful synergy and scientific cross-fertilization. In addition to concrete successes in the MURI research, it is also important to underscore the longer terms value and impact which this program had on its participants. Among the faculty involved, new collaborations and collegial contacts developed which have led to subsequent project interaction, joint research grant proposals etc. For example, Luryi and Zaslavsky have continued to advance the tunneling-based high speed novel transistor. Likewise, several of our graduate students had the opportunity to visit each others' laboratories (e.g. between Brown and MIT groups), and this has led to valuable scientific contacts and professional relationships after the students graduation.

In terms of the MURI program highlights and outcome, the following merit special mention:

(a) the project area involving Terahertz lasers (Task #1, led by Qiang Hu at MIT) led to world leading and pioneering results with this new compact semiconductor optoelectronic device technology. As an application example, these devices are being employed in prospective imaging schemes for medical and security diagnostics. For this this project, main support for the group at MIT came through the MURI grant, including an important postdoctoral fellowship for

Benjamin Williams. As for synergy, the constant interactions, often on an informal basis (as though within a single research group) between the experimental efforts by Prof. Hu, and Profs. Luryi (Stony Brook) and Maris (Brown), offered valuable insight to the THz laser project in terms of the complex superlattice design where electron-phonon interaction for resonant energy transfer and relaxation were the two key physical parameters to optimize. Serge Luryi offered much theory insight into the electron-phonon interaction in lower dimensional materials, enabling realistic simulations to be applied to the THz emitter design, while Humphrey Maris' Task area #6 provided valuable input to the considerable and challenging heat management issues (including the complex problem of heat transport across interfaces - Kapitza resistance etc).

(b) the discovery that high power gallium nitride FETs emit copious amounts of their operational energy as coherent acoustic phonons was a discovery uniquely credited to the support by the MURI grant (Task #5). The group of A. Nurmikko (Brown) was able to design an all-optical experiment on GHz range GaN/AlGaIn FETs with considerable input from H. Maris (modulation spectroscopy; coherent phonon generation expertise), as well as employ carrier injection levels to study and formulate the observed effect by input from S. Luryi (screening of the e-phonon interaction by 2D electron gas). This research may lead to better management of the thermal energy and device heating issues by utilizing the coherent phonon propagation as a means to "self-extract" dissipation from the active region of future high performance, high power GaN microwave FETs.

(c) the innovation of three classes of ultra high speed tunneling based transport devices, all operating at room temperature and hence involving phonon-assisted processes, were investigated during the course of the MURI project (Task#4). The original idea for the project emerged from theoretical concepts by S. Luryi (Stony Brook), and was implemented by A. Zaslavsky (Brown). The two colleagues began by working on multiemitter interband tunneling heterojunction bipolar transistors (HBTs), and subsequently fabricated by team in collaboration with Agere Systems. As described in detail for Task #5, these multiemitter Si/SiGe HBTs provided the high current gain available in standard HBTs, but with simplified processing as well as additional logic functionality. Encouraged by the success in the MURI program, coupled by the ascendancy of silicon-on-insulator (SOI) technology, Zaslavsky and Luryi have investigated two classes of SOI-based tunneling transistors: the lateral interband tunneling transistor (LITT) and the vertical tunneling transistor (VTT).

(d) the modeling and experiments of thermal transport through multilayer nanostructures by H. Maris (Brown, Task #6). All of the micro- and optoelectronic devices addressed in the MURI research required understanding the thermal transport through multilayer semiconductor heterostructures. The "phonon transport" research results which emerged from this MURI research have shed entirely new light to the complexity of thermal conductivity in semiconductor superlattices, which was experimentally measured to be substantially reduced relative to the conductivity of the component materials. In short period GaAs/AlAs superlattices, for example, the conductivity is as much as a factor of ten smaller than in bulk GaAs. A part of this reduction can be attributed to the modifications of the phonon dispersion relation that arise from zone folding. The effect of this zone-folding is predicted to give a reduction in conductivity that is greatest for layer thickness around 10 monolayers. Based on the zone-folding effect the conductivity of superlattices would be expected to increase for shorter period superlattices. Yet, experimental measurements in the MURI team (Maris, Nurmikko) showed that the conductivity

decreases monotonically as the layer thickness is reduced in the range 1 to 10 monolayers, and thus disagree with the expectations based on zone folding. To achieve a more complete understanding of how heat flows through a superlattice, a sophisticated molecular dynamics simulation program to model heat flow in multilayered structures. With this modeling approach, a realistic understanding and predictive capability for heat transport was achieved, to aid device designers (such as G. Belenky and S. Pei in the MURI team) to accurately estimate the thermal constraints of their mid-IR laser devices.

Another important part of the MURI outcome was the coupling to industrial and government laboratories. For example, the work on phonon transport and heat management involved a bridge to Intel, the THz work involved a close collaboration with Sandia and Lincoln Laboratories, the mid-IR laser work with the Air Force Research Laboratory (Albuquerque) and Sarnoff Labs.

We now describe in details the scientific and technology achievements of each of the primary thrust (task) areas within the MURI program:

Task #1: Phonon Engineering for The Development of Terahertz Lasers Based On Intersubband Transitions : Project Leader: Qing Hu (MIT)

Co-Participants: S. Luryi (electron-phonon interaction and novel frequency tuning scheme), H. Maris (thermal conductivity measurements), Industry/Gov't Lab Link: Sandia National Laboratory, Lincoln Laboratory

Terahertz (1-10 THz, $\hbar\omega = 4\text{-}40$ meV, and $\lambda = 30\text{-}300$ μm) frequencies are among the most underdeveloped electromagnetic spectra, even though their potential applications are promising in detection of chemical and biological agents, imaging for medical and security applications, astrophysics, plasma diagnostics, end-point detection in dry etching processes, remote atmospheric sensing and monitoring, noninvasive inspection of semiconductor wafers, high-bandwidth free-space communications, and ultrahigh-speed signal processing. This underdevelopment is primarily due to the lack of coherent solid-state THz sources that can provide high radiation intensities (greater than a mW) and continuous-wave (CW) operations. This is because the THz frequency falls between two other frequency ranges in which conventional semiconductor devices have been well developed. One is the microwave and millimeter-wave frequency range, and the other is the near-infrared and optical frequency range. Semiconductor electronic devices that utilize freely moving electrons (such as transistors, Gunn oscillators, Schottky-diode frequency multipliers, and photomixers) are limited by the transit time and parasitic RC time constants. Consequently, the power level of these electronic devices decreases as $1/f^4$, or even faster, as the frequency f increases above 1 THz. Semiconductor photonic devices based on quantum-mechanical interband transitions (such as bipolar laser diodes), however, are limited to frequencies higher than those corresponding to the semiconductor energy gap, which is higher than 10 THz even for narrow-gap lead-salt materials. Thus, the frequency range of 1-10 THz is inaccessible for conventional semiconductor devices.

Semiconductor quantum wells are human-made quantum-mechanical systems in which the energy levels can be designed and engineered to be any value. Consequently, unipolar lasers based on intersubband transitions (electrons that make lasing transitions between subband levels within the conduction band or holes within the valence band) were proposed for long-wavelength sources as early as in the 1970s. However, because of the great challenge in epitaxial material

growth and the unfavorable fast nonradiative relaxation rate, it took more than two decades to realize this proposal experimentally. Electrically pumped unipolar intersubband-transition lasers (also called quantum-cascade lasers (QCLs)) at $\sim 4\text{-}\mu\text{m}$ wavelength were first developed at Bell Laboratories in 1994. Since then, impressive improvements in performance have been made in terms of power levels, operating temperatures, and frequency characteristics at mid-infrared frequencies.

In contrast to the remarkable success of mid-infrared QCLs, the development of THz QCLs below the Reststrahlen band ($\sim 8\text{-}9\text{ THz}$ in GaAs) turned out to be much more difficult than initially expected, because of two unique challenges at THz frequencies. First, the energy level separations that correspond to THz frequencies are quite narrow ($\sim 10\text{ meV}$). Thus, the selective depopulation mechanism based on energy-sensitive LO-phonon scattering, which has been successfully implemented in mid-infrared QCLs, is not applicable. Second, low-loss optical mode confinement, which is essential for any laser oscillation, is difficult to implement at THz frequencies. Conventional dielectric-waveguide confinement cannot be used because the evanescent field penetration, which is proportional to the wavelength and is on the order of several tens of microns, is much greater compared to the active gain medium thickness of several microns.

In October 2001, almost eight years after the initial development of QCLs, the first QCL operating below the Reststrahlen band, at 4.4 THz , was developed. This laser was based on a chirped superlattice structure that had been successfully developed at mid-infrared frequencies. Mode confinement in this THz QCL was achieved using a double-surface plasmon waveguide grown on a semi-insulating (SI) GaAs substrate.

0

Supported by the AFOSR MURI program, Phonon Enhancement of Electronic and Optoelectronic Devices, our group has pursued a different approach to achieve lasing at THz frequencies. We have investigated possibilities of using fast LO-phonon scattering to depopulate the lower radiative level, and using double-sided metal-metal waveguides for THz mode confinement. After an extensive investigation, these efforts finally bore fruit. In November 2002, a 3.4-THz QCL was developed in which the depopulation of the lower radiative level was achieved through resonant LO-phonon scattering. The performance of this laser device was promising, especially in its maximum operating temperature. A laser device fabricated from the very first wafer operated in the pulse mode up to 87 K , producing more than 4 mW of peak power at liquid-nitrogen temperature. When fabricated with the double-sided metal-metal waveguides, THz QCLs based on similar quantum-well structures have demonstrated the highest pulsed operating temperature of 164 K , the highest CW operating temperature of 117 K , and the longest wavelength of $161\text{ }\mu\text{m}$. These records in performance are even more impressive when they are compared with the rest of the field: 116 K for the highest pulsed operating temperature, 80 K for the highest CW operating temperature, and $150\text{ }\mu\text{m}$ for the longest wavelength. In the following, we provide a more detailed summary of this highly productive effort.

THz gain medium based on resonant LO-phonon scattering

The first THz QCLs were designed around chirped superlattice structures, which are characterized by large oscillator strengths. However, the depopulation of the lower lasing level relies on resonant tunneling and electron-electron scattering, which could suffer from thermal backfilling because of narrow subband separations within the lower miniband of a superlattice.

The direct use of LO-phonon scattering for depopulation of the lower state offers several distinctive advantages. First, when a collector state is separated from the lower lasing level by at least the LO-phonon energy $\hbar\omega_{LO}$ (≈ 36 meV, corresponding to 9 THz or ~ 420 K), depopulation can be extremely fast (< 1 ps). Second, the large energy separation provides intrinsic protection against thermal backfilling of the lower radiative state. Both properties are important in allowing higher temperature operation of lasers at longer wavelengths.

While fast scattering out of the lower lasing level is necessary to achieve population inversion, a long upper-state lifetime is also highly desirable. Our earlier designs addressed this problem by making the optical transition diagonal (i. e., between states in adjacent wells), so as to reduce upper-state overlap with the collector state. However, this resulted in a small oscillator strength, and in a broad emission linewidth due to interface roughness. A second design featured a vertical transition, which improved the radiative overlap and had a relatively narrow linewidth (~ 2 meV ≈ 0.5 THz), but depopulation was nonselective and slow, due to the thick barrier needed to reduce parasitic scattering from the upper state to the collector states.

The key element in our current design is to use resonant LO-phonon scattering to selectively depopulate the lower radiative level while maintaining a long upper-level lifetime. This resulted in a breakthrough success. Figure. 1(a) shows the conduction band profile and subband wavefunctions under the design bias of 64 mV/module. Each module contains four quantum wells, shown inside the dashed box, and 175 such modules are connected in series to form the quantum cascade structure. Under this bias, electrons are injected from the injector level 1' to the upper lasing level 5 through resonant tunneling. The radiative transition between levels 5 and 4 is spatially vertical, yielding a relatively large oscillator strength ($f_{54} \approx 0.96$). The depopulation is

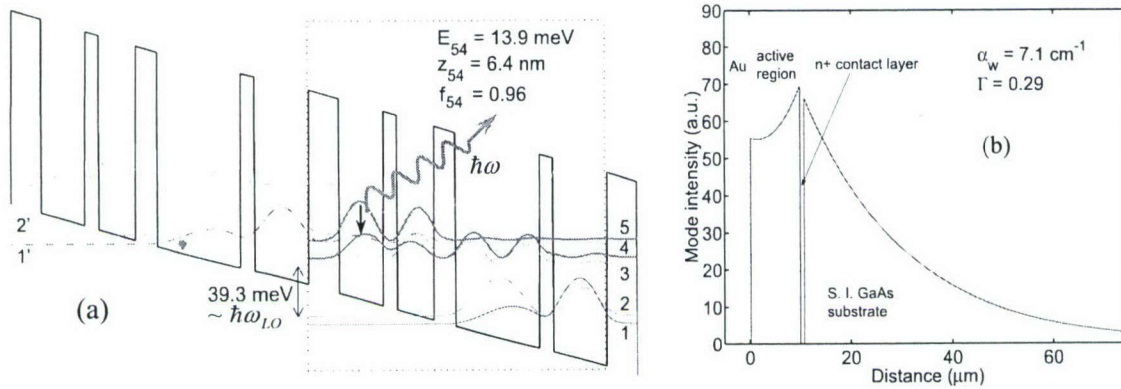


Figure 1: (a) Calculated conduction band profile and subband wavefunctions at a bias of 64 mV/module. (b) Optical mode profile of the surface-plasmon waveguide.

highly selective and fast, as only the lower level 4 is at resonance with a level 3 in the adjacent well, where fast LO-phonon scattering ($\tau_4 \approx \tau_3 \approx 0.5$ ps) takes place to empty electrons in levels 3 and 4 to the injector doublet 1 and 2. Hence the term resonant LO-phonon scattering. Due to a relatively thick barrier, the scattering time of the upper level 5 to the ground states 2 and 1 is quite long ($\tau_{5 \rightarrow 2,1} \approx 7$ ps), which is important to keep the population in level 5 high. Electrons

in level 1 are then injected to level 5 of the following module (not shown here), completing the cascade pumping scheme.

Mode confinement in this laser device was achieved using a double-surface plasmon waveguide formed between the top metallic contact and the bottom heavily doped GaAs layer, as in the case of other THz QCLs. The calculated mode profile and waveguide loss are shown in Figure. 1(b). After the rear facet was high-reflection (HR) coated, lasing was obtained in this device and a typical emission spectrum above threshold is shown in Figure. 2(a). The emission frequency corresponds to a photon energy of 14.2 meV, close to the calculated value of 13.9 meV. Pulsed lasing operation is observed up to 87 K with a power level of 13 mW at 5 K, and ~4 mW even at liquid-nitrogen temperature of 78 K, as shown in Figure. 2(b).

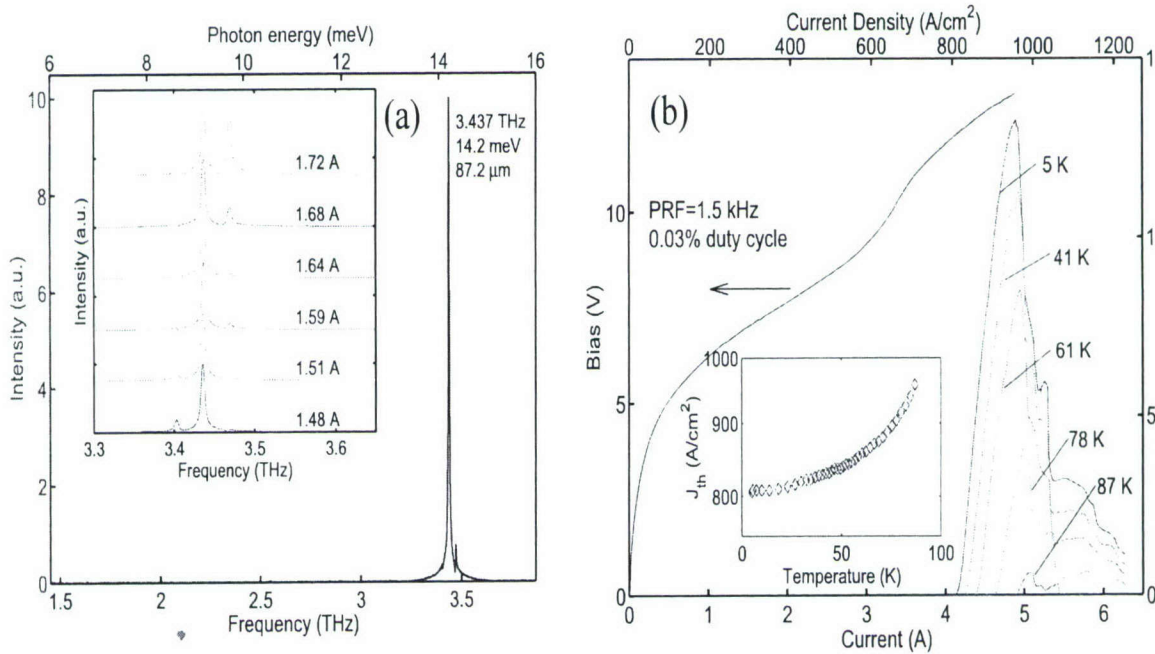


Figure 2: (a) Emission spectrum above threshold. The inset shows a set of emission spectra that are Stark-shifted to higher frequencies with higher bias. The linewidth is limited by the instrumental resolution of the FTIR ($0.125 \text{ cm}^{-1} = 3.75 \text{ GHz}$). **(b)** Pulsed power-current relations taken from a similar (with a larger area) laser device at different heat-sink temperatures.

THz mode confinement using double-sided metal-metal waveguides

Because of the amphoteric nature of silicon dopants in GaAs materials, the maximum attainable electron density is approximately $5 \times 10^{18} / \text{cm}^3$. At this carrier concentration, the field penetration depth is on the order of $1 \mu\text{m}$ at THz frequencies, causing a significant cavity loss if the lower side of the mode confinement is provided by heavily doped GaAs layers. The first successful development of THz QCLs utilized a double surface-plasmon layer grown on semi-insulating GaAs substrate for mode confinement. As illustrated in Figure. 1(b), the presence of the n^+ bottom contact layer enhances the mode intensity in the active region. Although the mode still

extends substantially into the substrate, the overlap with heavily doped regions is small, so the free-carrier loss is minimized. This structure is easy to grow and fabricate, and it provides adequate mode confinement for some of the THz QCLs. However, the mode confinement factor Γ in this scheme is far below unity ($\Gamma \sim 0.2$ - 0.5 for reported lasers).

Following our initial success in developing the 3.4-THz laser, we demonstrated the first terahertz QCL that uses a double-sided metal-metal waveguide for mode confinement. This metal-semiconductor-metal structure is essentially the same as the microstrip transmission lines that are widely used for waveguiding at microwave and millimeter-wave frequencies, and the geometry is compatible with the TM polarization of intersubband transitions. Due to the shallow skin depth in the metal (several hundred Å), the waveguide can be made with very low losses and a confinement factor close to unity. Our current THz lasers with metal-metal waveguide were fabricated using copper-to-copper wafer bonding followed by substrate removal. The schematic of the bonding and substrate removal process is illustrated in Figure. 3.

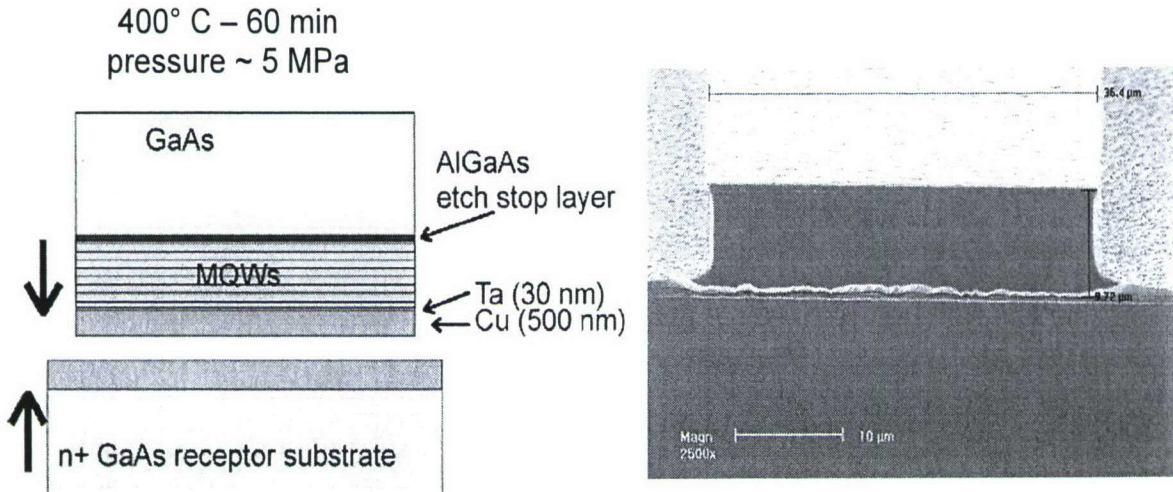


Figure 3: Left: Schematic of the wafer bonding process for double-side metal-metal waveguide. Right: A SEM picture of the fabricated device.

Based on this metal-metal waveguide structure and using improved gain media that reduced the lasing threshold current densities, we have achieved several records in the performance of THz QCLs. These include but not limited to: the highest pulsed operating temperature of 164 K (Figure. 4(a)), the first CW THz QCL operating above the important liquid nitrogen temperature of 77 K ($T_{\text{max}} = 117$ K, Figure. 4(b)), and the longest wavelength QCL to date without the assistance of magnetic fields ($\lambda \approx 161$ μm, corresponding to 1.9 THz (Figure. 4(c)).

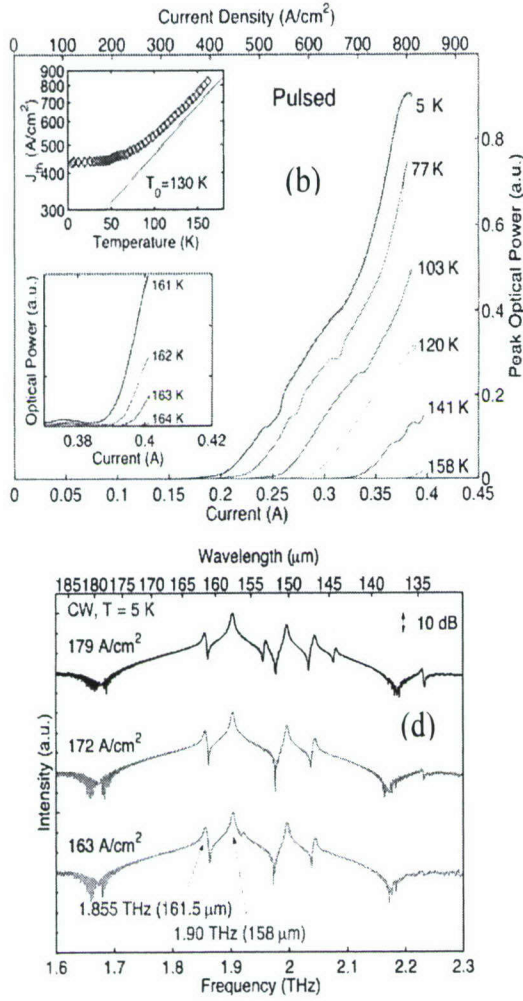


Figure 4. Upper left: Pulsed power-current and voltage-current relations measured up to ~ 164 K heatsink temperature. Upper: CW power-current and voltage-current relations measured up to ~ 117 K heatsink temperature. The inset shows the CW voltage-current and differential resistance-current relations of the device. Left: Lasing emission spectra at 1.9 THz.

Shortly after we successfully developed THz QCLs operating CW above liquid-nitrogen temperature, we were approached by several groups in the U.S. and Europe to test their suitability for local-oscillator applications. These collaborations quickly yielded results that provide positive confirmations. Figure 5 shows the schematic and measurement results of a 2.8-THz HEB heterodyne receiver pumped by a single-mode QCL as the local oscillator. The overall receiver noise temperature of ~ 1400 K is among the lowest at this high frequency. Figure 6 shows the schematic and measurement results of frequency locking of a QCL to the frequency of a far-infrared gas laser. The frequency stability of the QCL is achieved indefinitely, and the FWHM of ~ 65 kHz is more than adequate for astrophysical observations.

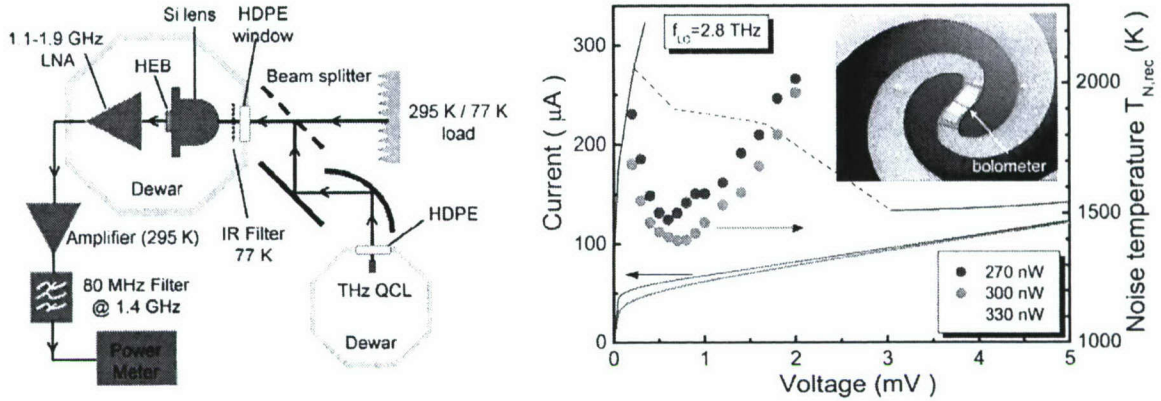


Figure 5: Left: Schematic of a HEB heterodyne receiver pumped by a 2.8-THz QCL as the LO. Right: Current and receiver noise temperature as functions of the voltage at several pump levels.

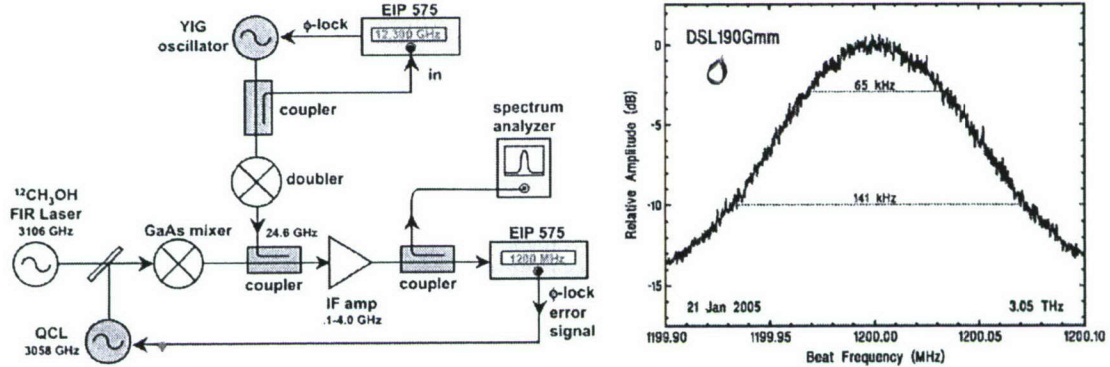


Figure 6: Left: Schematic of a frequency locking system to stabilize the frequency of a QCL respect to of a far-infrared gas laser. Right: A spectrum of the stabilized QCL with FWHM of 65 kHz that is stable indefinitely period of time.

In order to achieve a robust single-mode operation that is essential for sensing applications, we have also developed distributed-feedback (DFB) lasers using first-order gratings (grating period $= \lambda/2$). As shown in Figure. 7, the distributed feedback provided by the corrugated side walls ensure a single-mode operation at all temperature and bias ranges, with side-mode suppression greater than 35 dB. Furthermore, as the inset in the right figure shows, by changing the temperature of the heat sink, we were able to tune the lasing frequency by ~ 12 GHz. This temperature tuning can be useful in fine adjustment of the laser frequency relative to the target spectral lines.

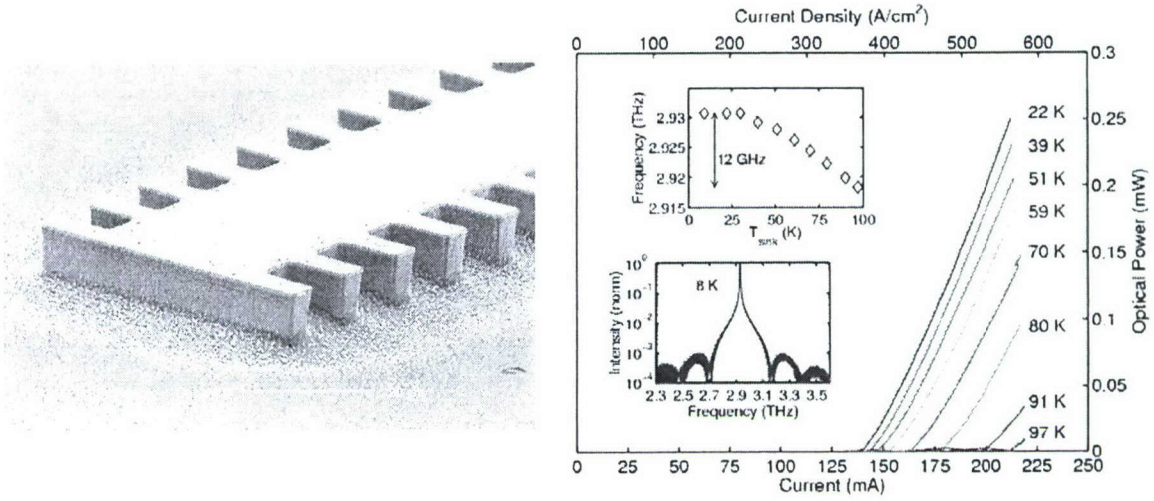


Figure 7: Left: SEM picture of a first-order DFB QCL with corrugated side walls. Right: Power-current of a 2.9-THz DFB laser device measured at different heatsink temperatures. The lower inset shows a single-mode lasing spectrum which is robust at all temperature and bias ranges. The upper inset shows the lasing frequency as a function of the heatsink temperature, with a ~ 12 GHz tunability.

Real-time THz imaging using quantum-cascade lasers and focal-plane array cameras

Due to the relatively modest power levels available in most THz sources and a lack of multi-element THz detectors, the vast majority of THz imaging has been done by mechanically scanning an object through a tightly focused beam – a practice which limits the acquisition time to the mechanical scan rate of the system. With upper limits of 100's of pixels/second for the mechanical scanning, a complete image takes minutes to acquire. It is highly desirable to use focal-plane array cameras that can directly detect the THz signals with sufficient speed. The coherent radiation source can be provided by solid-state frequency multipliers at submillimeter-wave frequencies, and by far-infrared gas lasers or quantum-cascade lasers (QCLs) above 1 THz. Because of their compact sizes, QCLs are especially attractive for multi-spectral imaging applications. Several QCLs with different frequencies can be packaged tightly forming a frequency agile coherent radiation source. When combined with a focal-plane array camera that is capable of video-rate detection, this system can perform frequency-sensitive THz imaging at a rate far greater than current THz imaging systems, allowing real-time THz monitoring and screening.

We have recently demonstrated the use of a 4.3-THz, 50-mW QCL source for real-time imaging with a 320×240 element microbolometer focal-plane array detector. The QCL is cooled to ~ 33 K by a closed-cycle, pulse-tube cryorefrigerator (PT60, Cryomech), and is modulated synchronously with the focal-plane array for differential detection. The differential scheme reduces $1/f$ noise and removes the infrared background, obviating the need for long-wavelength-pass filters. A signal-to-noise (SNR) ratio of ~ 340 and an optical noise equivalent power (NEPO) of $320 \text{ pW}/\sqrt{\text{Hz}}$ are measured. The experimental set-up is shown in Figure. 8, along with

a THz image taken at a video rate of 30 frames/second, demonstrating the feasibility of real-time screening and monitoring, which is crucial for military and security applications.

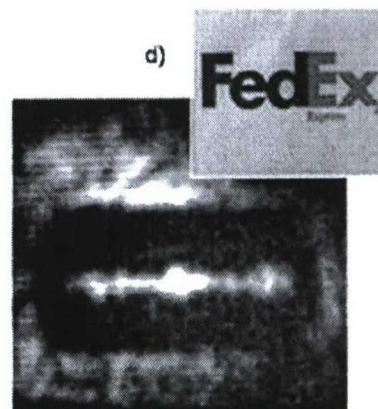
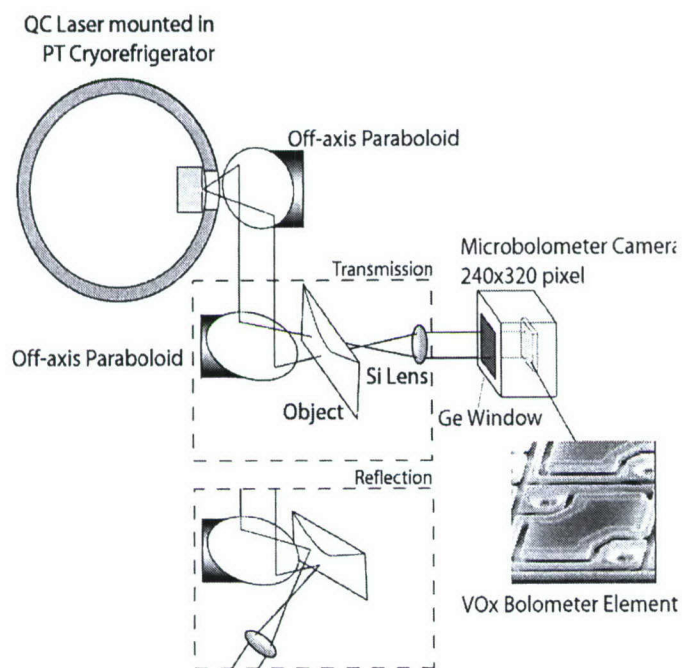


Figure 8.
Left: Schematic of a real-time imaging system with a THz QCL and a 240-by-320 focal-plane array camera.
Top: A real-time image of a razor blade inside a FedEx envelope taken at a video rate of 30 frames/second.

Task #2: Intersubband Lasers and Phonon Assisted Subband Depopulation: Project Leaders: Gregory Belenky and S. Luryi (Stony Brook)

Co-Participants: S.Luryi (electron-phonon interaction), A. Zaslavsky (device fabrication)
Industry Link: Sarnoff Corporation; Gov't lab link: Air Force Research Laboratory, Albuquerque, New Mexico.

Summary of the results

The research program was aimed at the enhancement of the semiconductor MIR laser performance by means of phonon related properties of constitutive materials. Of special interest for this program are type-II and type-I cascade structures which are the most prominent candidates for the high-power high-temperature laser sources in MIR region.

We demonstrated for the first time the possibility to use the LO-phonon-assisted depopulation scheme and showed that the rate of interband electron transitions assisted by LO-phonon emission can exceed the interband tunneling rate through the heterostructure leaky window originally suggested for the depopulation purpose in type-II laser structures.

We showed that phonon engineering allows strong enhancement of the LO-phonon-assisted depopulation of the lower lasing level, which enhances the performance of type-I cascade structures (see Patent #3).

New design of type-II intersubband laser structures with interband LO-phonon assisted depopulation of the lower lasing subband was proposed. The key element of our depopulation scheme is the use of interband electron transition which is indirect in both coordinate and momentum space. We show that strong Van Hove singularities of joint density of states can be designed for such transition thus enhancing the depopulation rate and making the efficiency of the interband electron-phonon depopulation in type-II structures higher than that of the corresponding intersubband process in type-I cascade laser heterostructures. We show that phonon-assisted depopulation can be employed in type-II structures even when the lower lasing level is designed near the upper edge of the heterostructure leaky window, where elastic interband tunneling depopulation becomes inefficient. Our design is beneficial for the type-II laser performance providing the highest value of the matrix element for intrawell optical lasing transition and simultaneously preventing thermal backfilling of the lower lasing states.

Lateral mode spatial filtering technique combined with the Hakki-Paoli approach was developed for gain measurements in broad area type II InAs/GaInSb mid-infrared diode lasers ($\lambda=3-3.1\mu\text{m}$) with W-type active region design. We showed that the main contribution to the temperature dependence of the threshold current is Auger recombination, which dominates the threshold current within almost the entire temperature range studied

New unipolar cascade laser structure with ultra-wide tunability range was proposed (see Patent #2). DFB action is achieved by periodic modulation of the carrier density and the optical gain due to piezo-acoustic wave propagating along the optical axis of a QCL. We predict distributed feedback in such piezo-DFB QCL sufficient for providing the mode suppression ratio over 30 dB. We show that, in contrast to bipolar lasers, the piezoelectric modulation of unipolar carrier density in type-I QCL is not accompanied by a degradation of the average gain. We show also

that the wavelength of the main DFB mode can be continuously tuned in a wide range, which is especially important for spectroscopic applications.

A method of optical gain and loss measurement was developed for type-II InAs/GaInSb interband cascade MIR lasers operating in the 3.4-3.6 μm wavelength range. The maximum temperature of CW operation was found to be limited by strong gain saturation due to active region overheating, while the temperature increase of the total optical loss was relatively small. We revealed a new mechanism of optical loss in mid-IR interband cascade lasers (ICL) – the “leakage” of the optical mode into the substrate. The effect can be eliminated by judicious matching of the laser wavelength and thicknesses of the optical cladding layers.

New method of temperature performance analysis was developed for diode semiconductor lasers. The method implies matching the temperature-concentration dependence at the threshold with steady-state temperature-concentration relationship induced by the carrier heating dynamics. We applied our theoretical approach to the type-II MIR cascade lasers and found excellent agreement with our experimental results obtained for 3.7 μm interband cascade (IC) lasers. The method allows optimizing the number of cascades in IC lasers with respect to the highest achievable operating temperature. We proved that the low material gain characteristic of type-II heterostructures and the high resistance of the thermal link to the heat sink are primarily responsible for limiting the continuous-wave (CW) operation to low temperatures.

- An ultra-sensitive single-pass measurement technique was developed for the first time for interband optical absorption measurements in thin layered laser heterostructures. This technique allows absorption measurement even in single-quantum-well laser heterostructures.
- Direct experimental information about the optical matrix elements in type-I and type-II laser structures was obtained by using single-pass interband optical absorption measurements. This information allows identification of the source of temperature sensitivity of the threshold current in type-II mid-IR GaSb-based semiconductor lasers. Our PL experiments also show that the PL temperature decay is noticeably stronger for type-II samples which indicates the presence of strong nonradiative recombination at elevated temperatures.
- New electrically tunable light source based on type-II cascaded structure design was proposed (see Patent #1). Our design combines high tunability of optical emission of type-II heterostructures with our original tunneling limited injection scheme, which enables laser wavelength tuning even after the laser threshold is reached. Laser tuning with the range of 120nm (starting from the initial lasing wavelength $\lambda \sim 3.33 \mu\text{m}$), or 120 cm^{-1} was demonstrated.
- A novel temperature insensitive semiconductor laser was invented. Quantum dot lasers were proposed years ago and one of their main predicted advantages was high temperature stability. Nevertheless, despite significant recent progress, their temperature stability has fallen far short of expectations. We analyzed the origin of this problem and found it was primarily associated with recombination outside the quantum dots. This has led us to propose a novel approach, based on spatially separating the reservoirs of electrons and holes from which the dots are fed with carriers. This can be accomplished in at least two ways by special tailoring of the laser heterostructures. A particularly

favorable way of accomplishing this is by using resonant-tunneling injection of majority carriers into quantum dots.

- Theoretical analysis of the intrinsic mechanism limiting the linearity of lasers with a quantum-confined active region. Carrier density in QD, QWR and QW lasers pins above threshold only in the active region. In the abutting regions from where carriers are fed by a capture process, the carrier density rises with injection current, owing to a nonvanishing capture delay. This “reservoir effect”, combined with the superlinearity of the recombination rate with respect to the carrier density outside the active region, gives rise to a new type of sublinearity of the light-current characteristics at high injection and limits the power performance of semiconductor lasers with a quantum-confined active region.
- We have carried out a theoretical analysis of the threshold behavior of semiconductor lasers with a reduced-dimensionality active region taking a general account of the internal optical loss. In any structure where the free-carrier density in the reservoir abutting the active region does not pin in the presence of light generation and the internal loss depends on this density, we predict the existence of a second lasing threshold. Above the second threshold, there exist two physically distinct steady-state regimes of stimulated emission. Accordingly, the light-current characteristic is two-valued up to a maximum current at which the lasing is quenched. Presented analysis, exemplified in the context of QD lasers, can be used for their optimization, especially for lowering the threshold current density in short-cavity structures.

Phonon-assisted depopulation in type-II intersubband lasers

The process of the lower lasing state depopulation is essential for maintaining the population inversion in the active region of intersubband cascade lasers. For type-II lasers, direct interband tunneling through the heterostructure “leaky window” δ (see Figure 1) has always been considered as a basic depopulation mechanism [1,2].

The rate of this process, Γ_{tun} , is proportional to the small parameter $\eta = \varepsilon(\delta - \varepsilon)/E_{GA}E_{GB}$ [3], where ε is the kinetic energy of the tunneling electron inside the window ($0 < \varepsilon < \delta = 150$ meV for InAs/GaSb interface) and $E_{GA}(B)$ are bandgaps of the constituent semiconductors. The efficiency of interband tunneling, therefore, decreases significantly when the depopulated energy level is located in the upper part of the leaky window, which would be the most favorable configuration from the standpoint of ensuring highest oscillator strength for the lasing transition and preventing thermal backfilling of

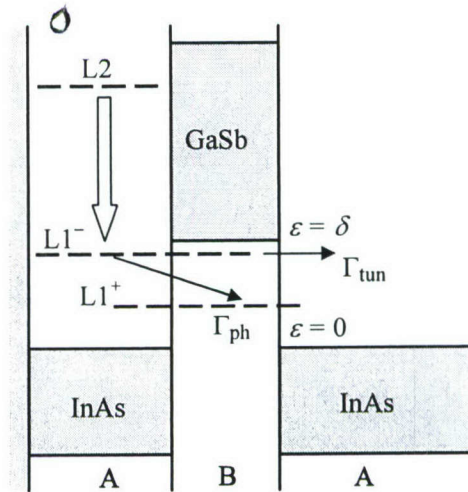


Figure 1: Band diagram of a model active region in a type-II laser heterostructure. Intersubband lasing transition from the upper electron level L2 and interband depopulation processes (Γ_{tun} and Γ_{ph}) through the heterostructure leaky window δ are shown by arrows.

the lowest lasing state. We demonstrate high efficiency of the depopulation process assisted by LO-phonon emission, which has not yet been studied in type-II laser structures. Indeed, the interband LO-phonon assisted tunneling is customarily considered an inefficient process due to the symmetry difference between the initial (electron) and final (hole) states [4]. We show here that this symmetry constraint can be removed by anticrossing the lowest electron-like and the highest light-hole-like levels in coupled InAs and GaSb quantum wells (QWs), so that the depopulation rate by resonant LO-phonon emission, Γ_{ph} , is comparable with that in type-I quantum cascade lasers [5].

To analyze the spectrum of the initial and final electron states participating in the phonon emission process we use a semianalytical approach [3] to the 6-band Kane model. Due to the high valence band offset at the InAs/GaSb interface, which includes the InAs energy gap E_{GA} , the heavy hole states need to be explicitly taken into account only in the GaSb layer B of the

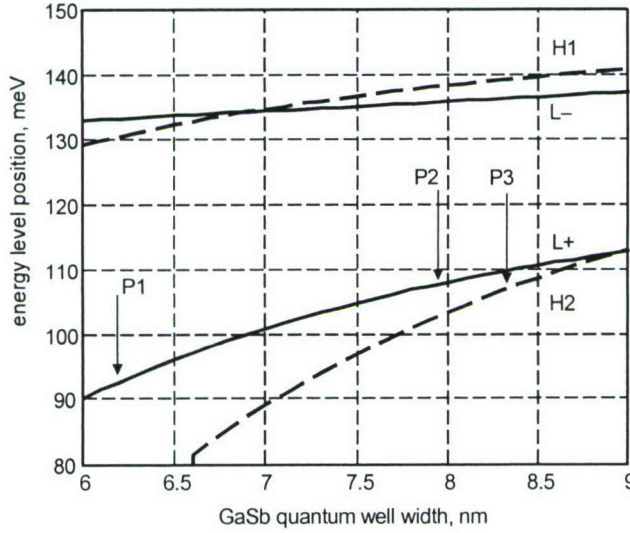


Figure 2: Positions of two highest light-type energy levels (solid lines) and two highest heavy-hole levels (dashed lines) in the leaky window as a function of the width of the GaSb quantum well d_B . The width of InAs quantum well $d_A = 9$ nm. Arrows indicate the onset of the LO-phonon resonant emission process.

The anticrossing condition corresponds to the minimal separation between these levels and, in our example, occurs at the InAs QW width $d_A = 9$ nm. Since the uppermost position of the level L^- decreases the thermal backfilling of the lower lasing states, it would be beneficial to keep its position as high as possible in the leaky window, still providing sufficient overlap with the final electron states in the L^+ subband. For this reason, we calculate and compare the LO-phonon emission rate for two different values, $d_A = 9$ nm and $d_A = 8.5$ nm, the later allowing for the higher position of the level L^- .

width d_B . As a next approximation, the quasibound character of the electron states in the leaky window δ can be neglected. This is reasonable for the InAs/GaSb heterosystem since the effective barrier for the interband tunneling at such an interface includes a combination of the energy gaps of both materials, E_{GA} and E_{GB} , so that the interband tunneling process through the heterostructure leaky window is determined by previously-mentioned small parameter $\eta < 1$.

To optimize the depopulation process, we need to provide the anticrossing between the lowest electron-like and the highest light-hole-like subbands, which is favorable for electron-phonon wave function overlap in the phonon emission process [6]. Figure 2 shows the positions of two highest light-type energy levels in the leaky window, L^- and L^+ , for electron wave vector $K = 0$ as a function of the GaSb QW width d_B .

Figure 3 shows the LO-phonon emission rate calculated according to the Fermi golden rule and assuming the final states for electron transitions to be unoccupied. The initial electron state in L-subband is chosen with the in-plane momentum $K = 0$, therefore the phonon wave vector q determines the momentum transfer in the electron transition. Inasmuch as the polar mode confinement has not yet been studied in the InAs/GaSb heterosystem, we calculate the phonon emission rate using a model bulk-like phonon spectrum, so that the electron-phonon coupling constant β is mostly determined by the overlap integral between normalized electron and phonon envelopes, $I(q)$:

$$\beta_{if}(q) = \left(\frac{1}{\varepsilon(\infty)} - \frac{1}{\varepsilon(0)} \right) I_{if}(q); \quad (1)$$

$$I_{if}(q) = \int dz' \psi_i^*(z) \psi_f(z) \int dz' \psi_f^*(z') \psi_i(z') e^{-q|z-z'|} \quad (2)$$

Since the LO-phonon energies are very close in both constituent materials, $\hbar\omega_{ph} \approx 30$ meV, the coupling constant in our calculations has been averaged with respect to the layer widths, $\beta_{eff} = (\beta_A d_A + \beta_B d_B) / (d_A + d_B)$. The increase of the GaSb QW width d_B in the range from 6 to 9 nm, while keeping the energy position of the initial electron-like state L- practically unchanged, allows “scanning” of all the final hole-like energy levels (light subband L+ and heavy subband H2), which thus move toward the upper part of the heterostructure leaky window.

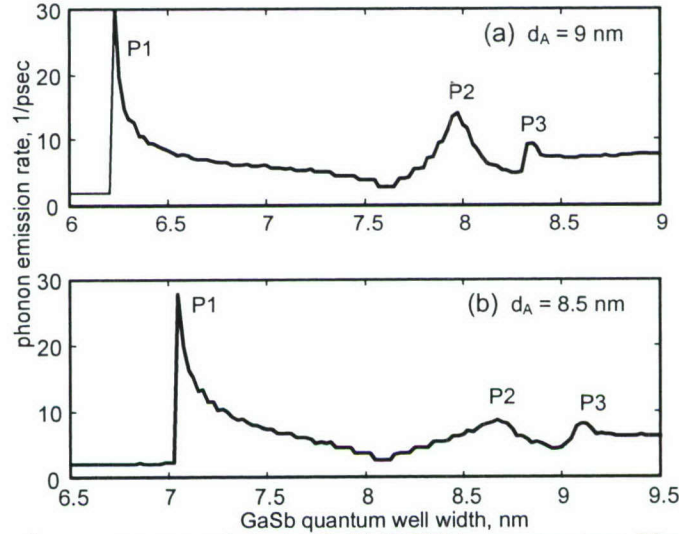


Figure 3: Electron-phonon resonance in InAs/GaSb DQW heterostructure. Three major peaks, P1-P3, correspond to the three different resonant transitions in K-space. **(a)** InAs QW width allows L+/L- subband anticrossing. **(b)** Smaller width of InAs QW providing for higher position of the lower lasing states in the heterostructure leaky window.

Figure 3 clearly demonstrates three peaks of the LO-phonon emission rate. The first, most remarkable resonance, P1, corresponds to the setup of the $L^- \rightarrow L^+$ phonon-assisted transition; see Figure 4a. This transition is indirect in K-space, since the top of the upper light-hole-like subband is displaced to the final value of K due to the presence of linear terms ωK in the subband dispersions inherent to asymmetric InAs/GaSb DQWs. Here the quantum number ω represents the parity of an eigenstate with respect to the reflection in the plane formed by the

main axis of the heterostructure and the two-dimensional wave-vector \mathbf{K} [3]. For illustrative purposes, we show the split subbands with different parities $\omega = \pm 1$, correspondingly, in positive and negative half-planes K . High density of states at the top of $L^+(\omega = +1)$ subband determines the high value of the resonant rate. It is important that this transition is indirect in Brillouin zone. For “vertical” transitions with

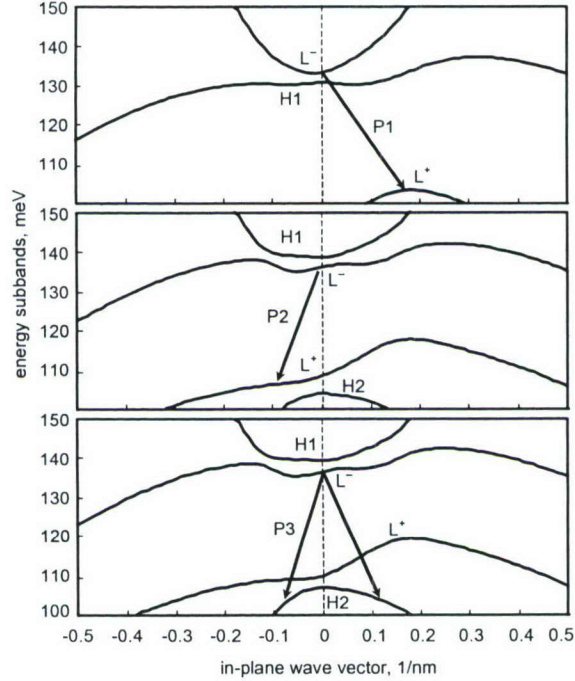


Figure 4: Band diagrams for the three most important resonant transitions with LO-phonon emission P1-P3. **(a)** Resonant transition corresponding to main peak P1, $d_B = 6.2$ nm. Final electron states are located on the ring of $L^+(\omega = +1)$ subband edges. **(b)** Resonant transition corresponding to the second peak P2, $d_B = 8$ nm. Final electron states for this transition are located on the ring of saddle points of the $L^+(\omega = -1)$ subband. **(c)** Resonant transitions $L^- \rightarrow H2$ corresponding to peak P3, $d_B = 8.3$ nm.

zero momentum transfer, the overlap integral (3) would vanish identically, since it is reduced simply to overlap between the orthogonal initial and final electron states. This is readily seen from Figure 5, where the overlap integrals for $L^-(0) \rightarrow L^+(K)$ transition are calculated as functions of the in-plane momentum K of the final state. We can see also that the anticrossing between L^- and L^+ subbands provides for sufficient electron-phonon overlap in this interwell (A \rightarrow B) transition.

With d_B increasing, transitions $L^- \rightarrow L^+$ become less efficient, firstly, because of corresponding decrease of the final density of states, and secondly, due to the suppression of the electron-phonon overlap integral $I(q)$ both at zero momentum transfer, $q \sim 0$, and at large phonon wave vectors $q > 0.2$ nm $^{-1}$. This explains the pronounced minimum in the phonon emission rate at $d_B =$

7.6 nm. Further increase of the GaSb QW width d_B results in the setup of the electron-phonon resonance related to the transitions to the L^- subband with negative parity (peak P2). The final electron states for these transitions belong to the ring of saddle points of the $L^-(\omega = -1)$ subband (see Figure 4b), which are characterized by a relatively high density of states and are favorably located at $K \sim 0.1 \text{ nm}^{-1}$, where the electron-phonon overlap is maximized, see Figure 5. Finally, peak P3 in Figure 3 corresponds to the setup of resonant transitions into the H2 subband, see Figure 4c. The overall peak amplitude is relatively small because the most important transitions to the subband top, characterized by the highest density of states, correspond to inefficient “vertical” transitions with nearly zero overlap integrals.

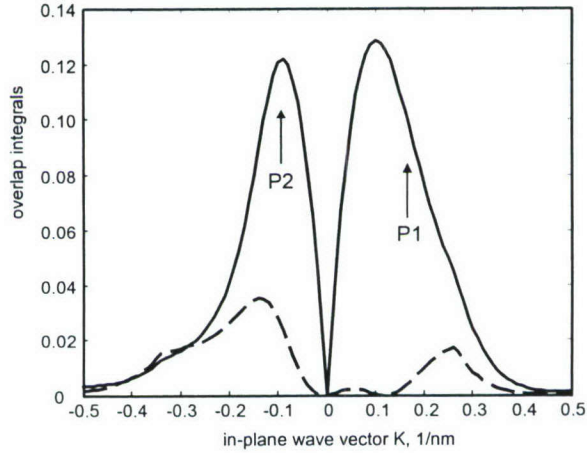


Figure 5: Electron-phonon overlap integrals (squared) for $L \rightarrow L^+$ transitions. The QW widths correspond to the main peak P1 in Figure. 7a, $d_A = 9 \text{ nm}$, $d_B = 6.2 \text{ nm}$. Solid line shows the overlap integrals for normalized electron and bulk-like LO-phonon envelopes. Dashed line shows the overlap integral between the initial and final electron states. Arrows mark the final state wave vectors for corresponding resonant transitions.

Figure 3b shows also the LO-phonon emission rate calculated for a narrower InAs QW width, $d_A = 8.5 \text{ nm}$. The lower lasing level L^- , which we must depopulate, has moved by 8 meV toward the upper end of the leaky window, and, as a result, all the resonances occur at larger values of GaSb QW width d_B . It is important that the amplitude of the main peak P1 remains practically unchanged. This means that the phonon-assisted depopulation can be conveniently employed when the lower lasing level is located in the extreme upper part of the heterostructure leaky window, where direct interband tunneling becomes inefficient. This design is beneficial for the laser performance providing the highest value of the matrix element for intrawell optical lasing transition and simultaneously preventing thermal backfilling of the lower lasing states.

Experimental study of the temperature performance of mid-infrared type-II “W” diode lasers

Type-II diode lasers are very promising for mid-infrared applications [7-9]. W-design of the active region [1] provides sufficiently large optical matrix element and permits wide range of lasing wavelengths which depend on the active region layer thickness and barrier height.

Performance of diode W-QW lasers degrades rapidly with increasing temperature. The highest reported heat sink temperature for CW operation of diode W-QW lasers is 200K [7], while for the optically pumped devices it is 290K [8]. We found that, in contrast with optically pumped devices [10-12], the internal loss in both 5 and 10 period diode devices is almost the same and remains nearly constant in the temperature range from 80K to 160K. The temperature increase of the threshold current can be thus explained by the dominant role of Auger recombination at high carrier concentrations combined with the linear temperature increase of the threshold concentration.

The diode W-QW laser structures were grown by molecular beam epitaxy. An n-type GaSb substrate was followed by a lattice-matched 1.5 μm thick n-type AlGaAsSb optical cladding layer ($N_D=2 \times 10^{17} \text{cm}^{-3}$), a lattice matched 0.6 μm thick AlGaAsSb separate confinement heterostructure (SCH) layer, a hole blocking region (in some structures), consisting of 7 periods 14 \AA AlSb/15 \AA InAs, W-QW active region, consisting of 5 or 10 periods of 80 \AA Al_{0.5}GaAs_{0.5}Sb_{0.95}/15 \AA InAs/27 \AA GaIn_{0.25}Sb/15 \AA InAs, another 0.6 μm AlGaAsSb SCH layer, a lattice-matched 1.5 μm p-type AlGaAsSb optical cladding layer ($N_A=5 \times 10^{18} \text{cm}^{-3}$) and a 50 \AA p⁺-GaSb cap layer. Only 5-W-QW structures had the hole blocking region.

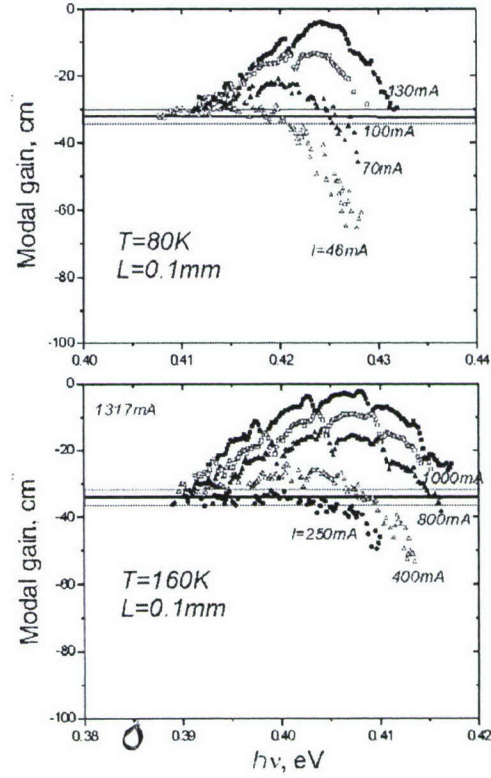


Figure 6: Spectral dependences of the modal gain for the laser with 10 quantum wells at 80K (upper panel) and 160K (lower panel).

Gain-guided lasers with 100 μm -wide stripe contacts were mounted p-side down on a copper heat sink attached to the cold finger of a liquid nitrogen cryostat. The gain spectra were measured using the Hakki-Paoli technique adapted to broad area devices [13]. Modal gain spectra for the 10-W-QW device operated in cw mode at 80K and 160K are shown in Figure 6. The modal gain is $g = N\Gamma G - \alpha_{\text{tot}}$, where N is the number of W-QWs, Γ the optical confinement factor per well and G the material gain. The total loss α_{tot} has been estimated from the low energy side of the modal gain spectra, where the material gain G is small, so that $g \sim -\alpha_{\text{tot}}$. This gives $\alpha_{\text{tot}} \sim 33\text{-}35 \text{cm}^{-1}$. One facet of each device was coated for high reflection and the other antireflection with reflectivities of $R_h=0.95$ and $R_a=0.05$, respectively. This corresponds to a mirror loss of $\alpha_m \sim 15 \text{cm}^{-1}$. Subtraction of α_m from the measured α_{tot} gives an internal loss of $\alpha_{\text{int}} \approx 18\text{-}20 \text{cm}^{-1}$. The temperature increase from 80 to 160K leads to an apparent broadening of the gain spectrum and

red shift of the gain maximum from 0.412eV to 0.397eV, with the linear temperature tuning coefficient $\beta \approx -2 \times 10^{-4}$ eV/K. The full width at half maximum of the gain peak increases from 12meV at 80K to 20meV at 160K. Measurements of the total loss at 160K give the same value within the experimental accuracy (Figure 6). The internal loss measured on 5-W-QW lasers is the same within experimental accuracy.

There are three major reasons for the temperature increase of the threshold current. These are: a temperature increase of α_{tot} , a temperature decrease of the differential gain dg_n^{max}/dJ and a temperature increase of the leakage current into the cladding region. It was shown previously, that at temperatures as high as 80C, the hole heterobarrier leakage current in GaSb-based lasers with similar waveguide and cladding materials is small and cannot be a limiting factor for the high-temperature performance [13]. We can specify two contributions to the total loss α_{tot} . First is the free-carrier absorption in the quantum wells. This mechanism is found to be dominant in multiperiod (50-80 periods) optically pumped devices, where it is responsible for more than a two-fold increase of α_{int} in the temperature range from 80K to 160K [10-12]. The second contribution is the loss due to modal overlap with the cladding material and light scattering in the waveguide. The fact that the internal loss does not depend strongly on either the number of wells (5 or 10), or temperature leads to the conclusion that the total loss in these electrically pumped W-QW lasers is the waveguide and cladding loss.

Since α_{tot} is independent of temperature, a possible reason for the temperature increase of the threshold current can be in the temperature dependence of dg_n^{max}/dJ . One can see (Figure 7) that as the temperature increases from 80K to 160K, the average dg_n^{max}/dJ decreases from $\sim 0.29 \text{ cm}^{-1}/\text{mA}$ to $\sim 0.03 \text{ cm}^{-1}/\text{mA}$. The behavior of dg_n^{max}/dJ for 5-W-QW samples is qualitatively the same, except that the magnitude of dg_n^{max}/dJ is larger, viz. $\sim 0.4 \text{ cm}^{-1}/\text{mA}$ (80K) and $\sim 0.1 \text{ cm}^{-1}/\text{mA}$ (120K) for the lasers without the hole blocker; and $\sim 0.7 \text{ cm}^{-1}/\text{mA}$ (80K) and $\sim 0.07 \text{ cm}^{-1}/\text{mA}$ (160K) for the lasers with the hole blocker. This indicates an inhomogeneous carrier distribution among the wells in the 10 W-QW devices, which reduces the effective number of wells [14] and suppresses dg_n^{max}/dJ .

The net gain maximum g_n^{max} can be expressed in terms of 2D carrier concentrations as (see, for example [15,16]):

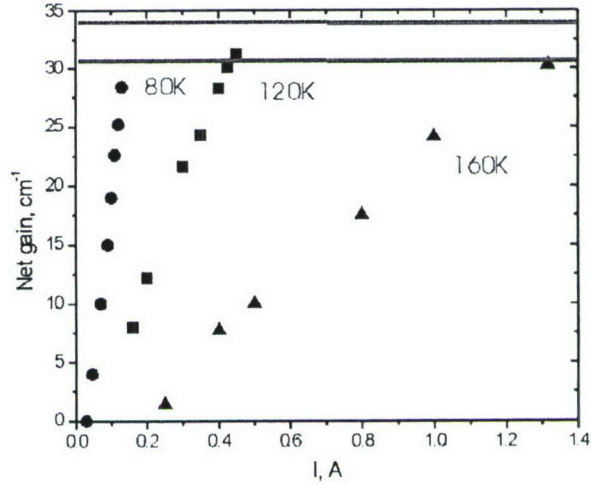


Figure 7: Dependences of the net gain maxima on current for the sample with 10 quantum wells at three different temperatures. Horizontal lines indicate α_{tot} .

$$g_n^{\max} = NTG_0 \left[1 - \exp\left(-\frac{\pi\hbar^2}{m_c^*} \frac{n(J,T)}{T}\right) - \exp\left(-\frac{\pi\hbar^2}{m_v^*} \frac{p(J,T)}{T}\right) \right] \quad (3)$$

Here, G_0 is a very weak function of T [16], $n, p(I, T)$ are the electron and hole concentrations in the wells, and m_c^*, m_v^* are the electron and heavy hole effective masses. The electron and hole concentrations are assumed to be equal and, for simplicity, broadening of the energy levels is not taken into account. To obtain information about the current and temperature dependences of the carrier concentration $n(J, T)$ we analyzed the spontaneous emission (SE) spectra collected from a side of the device [17]. A 0.5 mm slit was used to filter out the stimulated emission contribution from the laser facets. Dependences of the integrated spontaneous emission intensity I_{sp} on current below the threshold are shown in Figure 8. The dependence $I_{sp}(J)$ is linear at 80K, while at higher

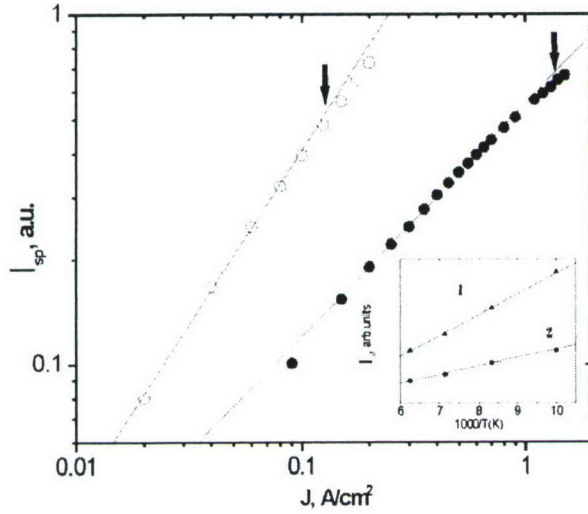


Figure 8: Current dependences of the integrated luminescence intensity I_{sp} at 80K (open circles) and 160K (solid circles). The arrows mark the lasing thresholds. The fitting lines are: $I_{sp} \sim J$ for 80K and $I_{sp} \sim J^{2/3}$ for 160K. The inset is the dependence of I_{sp} on inverse temperature for $I=0.1$ A (1) and 0.3 A (2).

temperatures a region $I_{sp} \sim J^{2/3}$ appears as the threshold increases. This dependence can be interpreted as a result of bimolecular radiative recombination when the carrier concentration is controlled by the Auger process [17]. The radiative recombination rate coefficient in the 2D case is proportional to $1/T$. One can see that within experimental accuracy I_{sp} is a linear function of $1/T$ (Inset in Figure 8), even at the current of 300mA, where Auger recombination already dominates. This means that within the temperature range from 80 to 160K the carrier concentration in the active area does not depend strongly on temperature at a fixed current, so we can neglect the temperature dependence of the Auger coefficient. A slow variation with T is consistent with previous findings [18]. For fixed α_{tot} the threshold carrier concentration n_{th} must be proportional to T in order to fulfill the threshold condition $g_n^{\max} = \alpha_{tot}$. A linear temperature increase of n_{th} defines the temperature dependence of the threshold current, associated with Auger recombination as $I_A \sim T^3$. Figure 4 shows dependences of the threshold current on

temperature in the samples with 5- and 10-W-QWs. The approximation $J_{th} \sim T^3$ is in very good agreement with experiment, i.e. I_A gives the main contribution to the J_{th} .

To obtain information about the effect of laser heating on the experimental results, we estimated an additional temperature increase ΔT of the active area in CW mode from the energy shift between the SE spectra recorded in pulsed (100ns, 2% duty cycle) and CW modes at (160K). Although ΔT is relatively small (<5 K) at CW currents below 800mA, it reaches 15-20K at the current ~ 1.3 A. This corresponds to a specific thermal resistance of $\sim 11 \text{ Kcm}^2/\text{kW}$.

In conclusion, we have experimentally investigated the optical gain and internal loss in $3\mu\text{m}$ type II W diode lasers. The internal optical loss is $18\text{-}20\text{ cm}^{-1}$ for devices with both a 5- and 10- W- QW active regions and remains nearly constant within the temperature range 80-160K. This implies that the main contribution to the internal optical loss is the waveguide and cladding loss rather than free carrier absorption in the wells. Analysis of the spontaneous emission spectra shows that the reason for the temperature increase of the threshold current is Auger recombination.

Piezoacoustic modulation of gain and distributed feedback for type-I cascade lasers

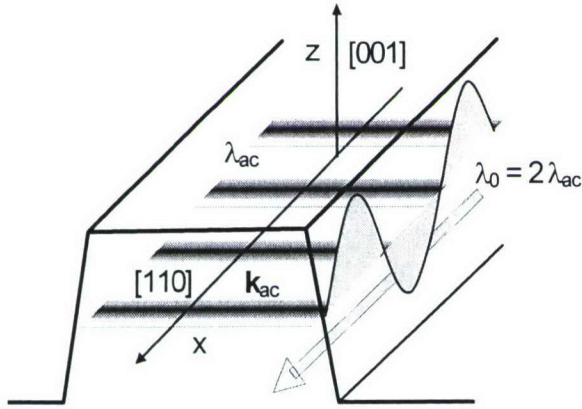


Figure 9: Piezoacoustic-DFB modulation geometry.

The quantum cascade laser (QCL) is the most promising candidate for mid-infrared atmospheric spectroscopy in 3-12 μm wavelength range.

Recent reports have demonstrated broadband emission in the wide range of 5 to 8 μm and single-mode DFB operation with the side-mode suppression ratio exceeding 30 dB. Generally, most trace-gas sensing applications also require reasonable operational tunability of the lasing wavelength, which at this time can be achieved only by varying the heat-sink temperature and/or pumping current.

This approach, based on the temperature dependence of the mode refractive index, has the drawback of extremely limited tuning range, which seldom exceeds a hundred nanometers. In this part of project we considered the possibility of an ultra-broadband tuning of the type-I QCL lasing wavelength by means of piezoacoustic modulation of the optical gain in the laser active region. We show that due to piezoelectric properties of III-V materials, an acoustic wave propagating along the optical axis of a unipolar laser (see Figure.9) produces a periodic modulation of the carrier density and the optical gain, sufficient for providing distributed feedback with the mode suppression ratio exceeding 30 dB. In contrast to bipolar lasers, the piezoelectric modulation of unipolar carrier density is not accompanied by a degradation of the average gain. Inasmuch as the acoustic frequency can be easily changed, the wavelength of the main DFB mode can be tuned in a wide range (see Figure.10). This property should be very attractive for spectroscopic applications of the quantum cascade laser.

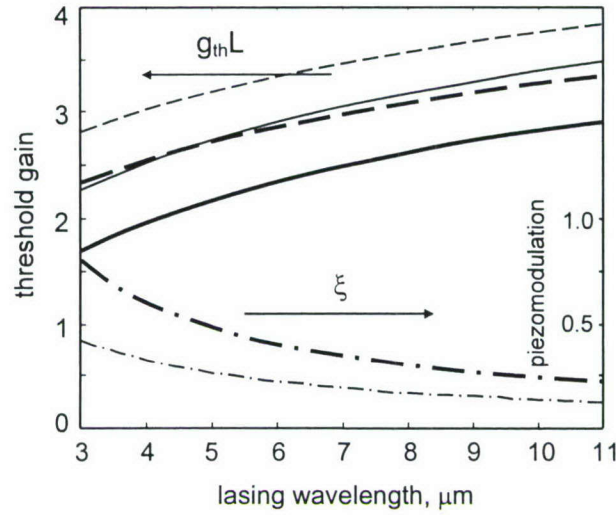


Figure 10: Spectral dependence of the gain threshold $g_{th}L$ and mode selectivity for QCL implemented in two material systems, based on In(Al)GaAs (thin lines) and GaAlN (thick lines). Solid lines: gain thresholds for the main Bragg modes; dashed lines: threshold gain for the next mode. Two lower curves (dash-dotted lines) represent piezomodulation strength ξ . The assumed acoustic power and doping level are, respectively, 5 KW/cm² and 5×10^{16} cm⁻³ for both systems.

Experimental study of the optical gain and loss in mid-infrared type-II interband cascade lasers

High performance mid-infrared type-II interband cascade lasers (ICL) with $\lambda = 3.7 \mu\text{m}$ have been recently demonstrated under continuous wave (CW) operation above 77K [19]. To understand physical mechanisms limiting high temperature performance of the device one needs to analyze temperature dependencies of device parameters which determine the threshold current. These parameters include optical gain, loss and current leakage. Estimation of the internal optical loss α_i in mid-IR ICL based on the dependence of inverse external quantum efficiency on cavity length was presented in [20]. In this paper we present experimental study of optical loss and gain of mid-IR type-II ICL using the Hakki-Paoli approach adapted for broad area lasers [13]. This method allows measuring the optical gain and loss in one single device without extracting it from the data taken at series of samples. We found that together with slight

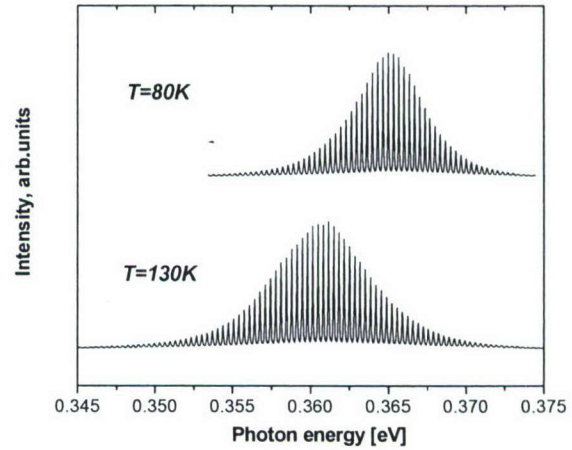


Figure 11: ASE spectra of the interband cascade laser M19.

temperature increase of the total optical loss there is strong saturation of the gain with the current at higher temperatures. This effect plays crucial role in limiting CW temperature performance

Typical amplified spontaneous emission (ASE) spectra at 80K and 130K are shown in the Figure 11. A spatial filtering technique was used to select on-axis emission. The modal gain spectra obtained from the fringe contrast are shown in the Figure 12. Total optical loss estimated from the low energy part of the gain spectra is about $58\text{-}60\text{ cm}^{-1}$ at 80K and remains almost constant up to 140K. A further temperature increase up to 200K increases the total loss to 84 cm^{-1} . The reflection coefficient from uncoated laser facets ($r \sim 0.33$) was calculated using the effective refraction index extracted from the frequency spacing between the fringes. This gives the mirror loss $\alpha_m \sim 22\text{ cm}^{-1}$, so that the internal loss are $\alpha_i \sim 36\text{-}38\text{ cm}^{-1}$ ($T=80\text{ K}$) and $60\text{-}62\text{ cm}^{-1}$ ($T=200\text{ K}$).

The dependence of the modal gain maximum on the current density (Figure 13) shows strong gain saturation at high temperatures (140K). This effect is explained by the active area heating. We show that the temperature increase of optical loss and gain saturation effect are responsible for the device temperature performance. The temperature of the active area was estimated from the difference in threshold currents and emission spectra, taken in cw and pulse regime with low duty cycle (Figure 14). Considerable overheating of the active area at higher heat sink temperatures was observed. This effect provides positive feedback between increasing loss, increasing threshold current, and increasing active region temperature, thus limiting the maximum operating temperature of the ICL.

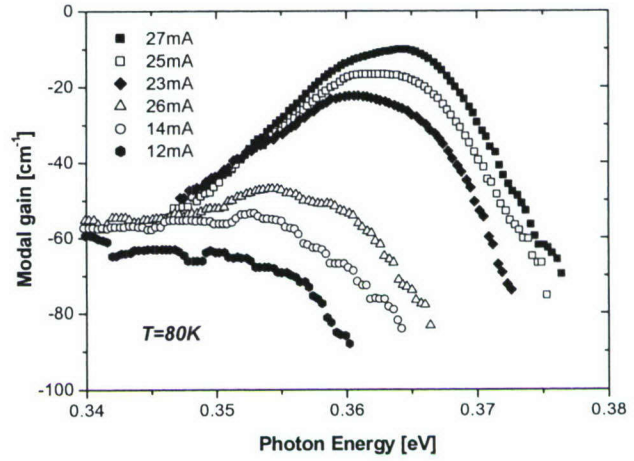


Figure 12: Modal gain spectra for ICL M19.

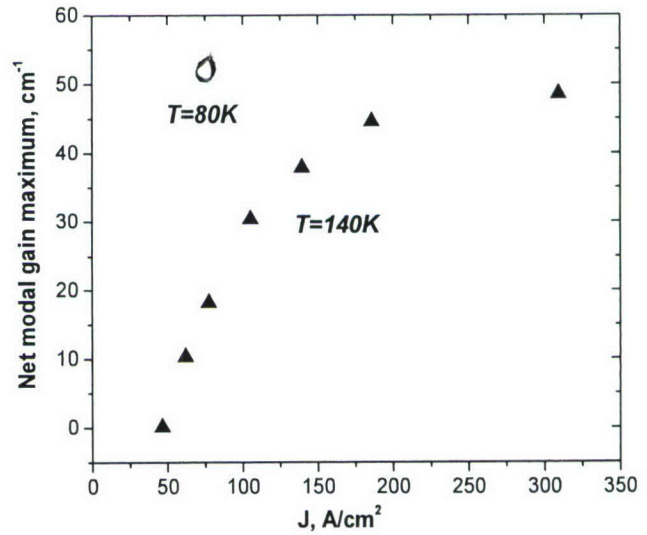


Figure 13: Modal gain maximum vs current density for ICLM19.

Strong periodic modulation of both ASE and the gain spectra have been observed in some samples (Figure. 15). The gain modulation minima move with the increasing sample temperature which excludes interference effects from outside the sample.

We show that the gain modulation is due to the optical mode leakage through the cladding [21,22], which leads to the appearance of periodic and wavelength-dependent contribution to the total loss as well as to periodic modulation of the optical confinement factor. The effect is very

sensitive to the cladding thickness and the emission wavelength. No modulation was observed in the devices with shorter wavelength and thicker cladding layers (Figure. 11). The mode leakage leads to the strong reduction of the modal gain at certain frequencies and can decrease the overall laser performance.

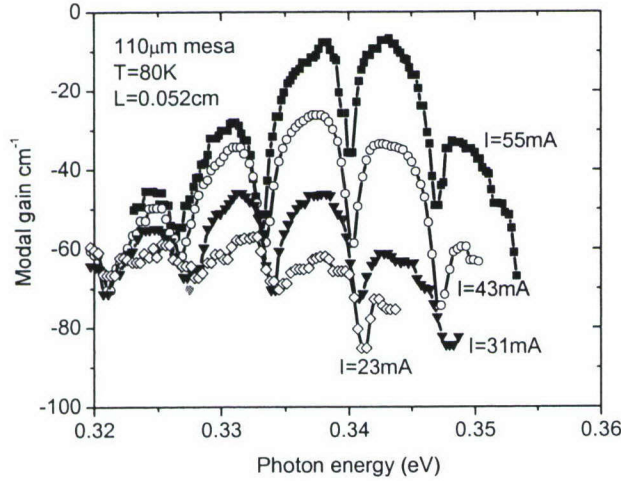


Figure 15. Modal gain spectra at different current values for ICL4.

current. At some point, this leads to a lasing failure. For design purposes, it is very important to understand the main "trigger" mechanism of such a failure – whether it is the Joule heating of the crystal lattice or the Auger-related heating of the electron subsystem.

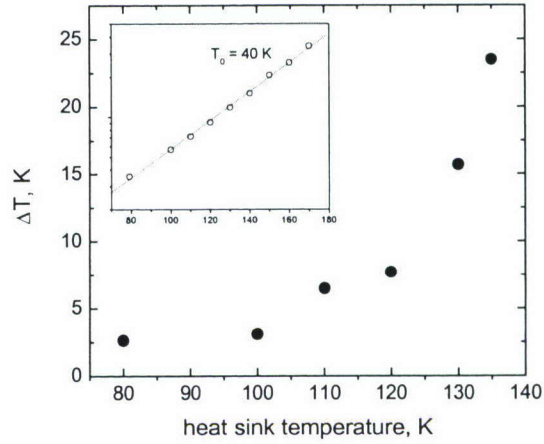


Figure 14: Temperature difference between active region and heatsink (ΔT) versus heatsink temperature for cw operation of a 3.4 μm 65 μm mesa device at threshold. Inset: threshold current density versus heatsink temperature for a 3.4 μm 65 μm mesa device operated in low duty cycle pulsed mode.

Achieving CW room-temperature operation of ICL is still unsolved problem. In mid-infrared lasers, the modal optical gain is a strong function of both the carrier concentration and the carrier temperature, $g(n_e, T_e)$. Any increase of the laser operating temperature is accompanied by a compensating rise of the carrier concentration in the active region, which in electrically injected lasers implies a corresponding increase of the threshold current. The later in turn induces additional Joule heating, while the concentration build-up enhances the non-radiative (Auger)

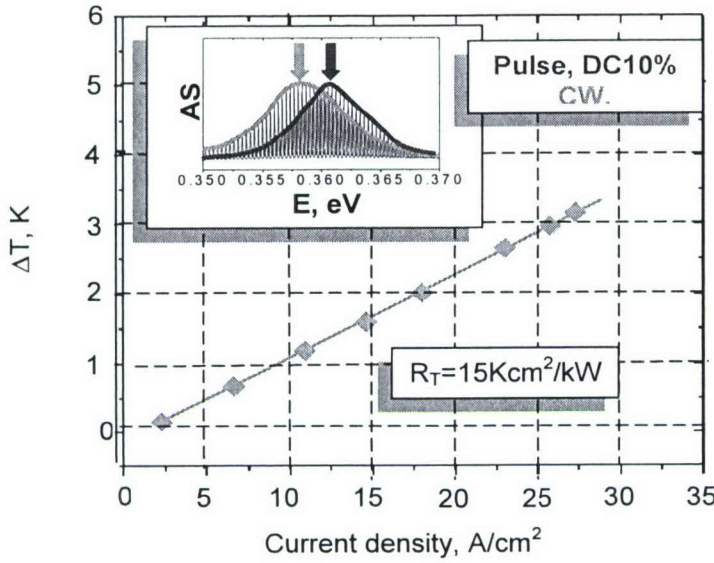


Figure 16. Active area overheating ΔT can be obtained as a function of injection current density.

area temperature. The active area overheating ΔT can be obtained from the spectral shift between amplified spontaneous emission (ASE) spectra taken at low duty cycle and CW modes. The inset in the Figure 16 shows a pronounced red shift of the ASE spectrum taken in the CW mode in comparison with this taken at 10% duty cycle. The ASE spectral shift as a function of temperature was measured in low duty cycle mode to provide the calibration curve. The typical temperature coefficient of the ASE spectrum position is 0.1 meV/K. The specific thermal resistance obtained for this sample was 15 Kcm²/kW. One can see from the Figure. 16 that at the bias current density about 270 A/cm², ΔT is more than 30K thus explaining strong temperature performance degradation of the device.

Figure 17 shows the laser spectra taken in CW mode at two different temperatures – 77K and 214K. The CW operation temperature of 214K is the highest reported CW operation temperature among electrically pumped lasers emitting between 3 and 4 μm . In the higher temperature spectra (blue line) one can see periodical structure which may point on optical mode leakage into the substrate. A relatively low $T_0=40K$ obtained in the low duty cycle

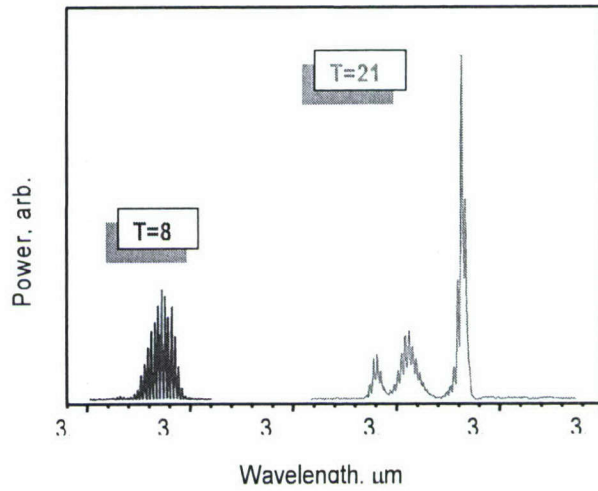


Figure 17: Laser emission spectra in CW operation mode. In the higher temperature spectra (red line) one can see periodical structure which may point on optical mode leakage into the substrate.

regime and the absence of strong temperature dependence of the external efficiency point on the Auger recombination as a process, which determines nonradiative lifetime in this devices.

The Auger recombination is commonly believed to be the basic physical mechanism limiting their CW operation to low temperatures, especially at high injection levels, typical for near-room-temperature operation.

Our theoretical analysis shows however that the high value of the specific thermal resistance in antimonide based ICLs can equally determine the ultimate cause of the device failure [23] This agrees well with our experimental data for 3.7 μm type-II cascade lasers.

The increase of the number of cascade stages N results in the sharp increase of the temperature performance with N at small $N < 20$ due to the increase of the confinement factor and the modal gain.

Further increase in the number of stages, however, proportionally increases the threshold voltage and the heat dissipation in the active region. Since both the confinement factor and the modal gain saturate at large N , this leads to device overheating and gradually decreases the maximum operating temperature T_{max} for $N > 30$. We have shown that an optimum number of stages exists in ICLs with respect to the highest possible heat-sink temperature T_{max} . This number lies in a rather wide range between 20 to 30 cascades (see Figure 18), so that additional optimization with respect to the output optical power is also possible [25].

In summary, the effect of the operation and design parameters of IC laser on the maximum CW operation temperature of the device has been analyzed experimentally and theoretically. We found that:

1. The low material gain characteristic of type-II heterostructures and the high resistance of the thermal link to the heat sink are primarily responsible for limiting the continuous-wave (CW) operation of the ICL to low temperatures.

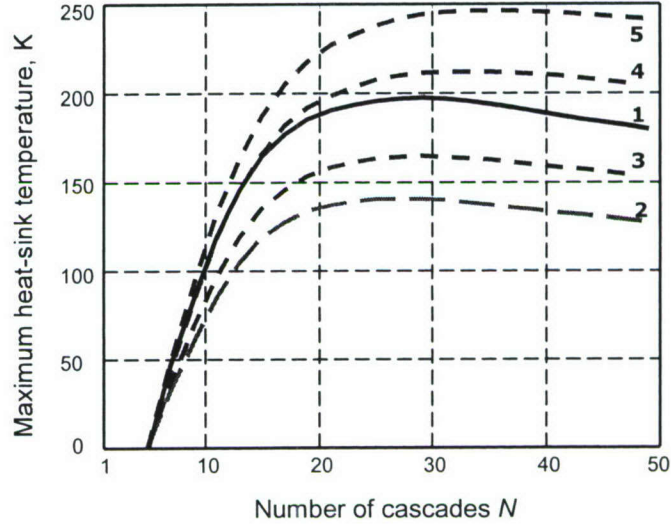


Figure 18: Maximum heat-sink temperature vs. number of cascades N for type-II ICLs. The long-dashed curve demonstrates the strong depression of the maximum operation temperature by Auger recombination. The short-dashed curves illustrate the recovering effect of the lower thermal resistance. Room temperature operation become feasible at the lowest thermoresistance value $\rho_T < 3 \text{ K}\cdot\text{cm}^2/\text{kW}$ even for an Auger coefficient as high as $C = 10^{-26} \text{ cm}^6/\text{s}$ (curve 5).

2. The number of cascades in type-II ICL can be optimized with respect to the highest achievable operating temperature. We have proved experimentally that the devices with narrower stripes (down to 4-8 μm) having also lower thermoresistance values demonstrate higher maximum CW operation temperature. We show, however, that further reduction of the stripe width leads to threshold current increase due to the enhanced contribution of the edge recombination.

Mechanism of the temperature sensitivity of mid-IR GaSb based semiconductor lasers

Type-II band alignment provides an opportunity to control wavelength in a wide spectral range by changing the quantum well widths rather than material composition. However, the temperature performance of type-II mid-IR quantum well lasers is still a crucial issue for successful fabrication of electrically pumped continuous wave (CW) operated device in the practically important 3-4 μm spectral range. The highest reported CW operation temperatures were 214K ($\lambda=3.4 \mu\text{m}$) [26] and 217K ($\lambda=3.2 \mu\text{m}$) [27]. Being characterized by relatively low threshold current densities at cryogenic temperatures ($J_{th} \sim 10\text{A/cm}^2$, $T=78\text{K}$ in type-II intersubband cascade lasers [26]), type-II mid-IR lasers show strong performance degradation as the temperature increases up to 300K. The typical values of parameter T_0 characterizing exponential increase of the threshold current with temperature were reported for the diode type-II mid-IR lasers in the range of 30-50K [28], which is inferior to both type I quantum well lasers with shorter wavelength ($T_0=85\text{K}$, $\lambda=2.5 \mu\text{m}$) [29] and intersubband quantum cascade lasers with longer wavelength ($T_0=195\text{K}$, $\lambda=4.8 \mu\text{m}$) [30].

The following factors can result in low T_0 of type-II mid-IR devices: i) temperature increase of the optical loss, ii) low differential gain due to reduced electron and hole wave function overlap, iii) thermally activated carrier escape from the active quantum wells due to insufficient hole confinement, and iii) possible enhancement of the nonradiative recombination rate in non-optimized structures. Previous studies [31] exclude the temperature dependence of the optical loss as a reason for low T_0 in mid-IR lasers. In this project, to analyze factors ii) and iii) we compare the optical properties of type-I and type-II Sb-based heterostructures measuring the optical absorption and photoluminescence temperature quenching in the spectral range near the heterostructure optical edge.

Table 1.

The structure parameters

	QW material	QW width nm	Waveguide material	Cladding material	λ (13K) μm	Hole confinement meV
1-I	In _{0.41} GaAs _{0.14} Sb	10	Al _{0.25} GaAs _{0.022} Sb	Al _{0.9} GaAs _{0.075} Sb	1.96	60
2-I	In _{0.53} GaAs _{0.25} Sb	14.5	Al _{0.25} GaAs _{0.022} Sb	Al _{0.9} GaAs _{0.075} Sb	2.49	0
1-II	InAs/In _{0.4} GaSb/InAs	1.65/2.4/1.65	In _{0.2} GaAs _{0.18} Sb	Al _{0.9} GaAs _{0.09} Sb	3.69	80
2-II	InAs	2.4	In _{0.2} GaAs _{0.18} Sb	Al _{0.9} GaAs _{0.09} Sb	3.45	0

We study two groups of samples (group I and group II) with predominantly type-I and type-II band alignment. Each group consists of two structures which are characterized by different hole confinement; see Table 1.

The hole confinement energies were calculated using the material parameters given in work [32]. Calculated band profiles and positions of energy levels participating in optical transition are presented in Figure 19. The structures have been grown by MBE on GaSb substrates. In group I structures, two compressively strained InGaAsSb quantum wells are incorporated in the $\text{Al}_{0.25}\text{Ga}_{0.75}\text{As}_{0.022}\text{Sb}_{0.978}$ waveguide core sandwiched between $\text{Al}_{0.9}\text{Ga}_{0.1}\text{As}_{0.075}\text{Sb}_{0.925}$ cladding layers lattice-matched to GaSb substrate. Group II structures consist of GaSb-matched $\text{In}_{0.2}\text{Ga}_{0.8}\text{As}_{0.18}\text{Sb}_{0.82}$ waveguide with six quantum wells. These wells represent InAs/Ga_{0.6}In_{0.4}Sb/InAs layers (W-type quantum wells, sample 1-II) [33] or a single InAs quantum well layer (sample 2-II) [34]. The cladding material in both cases is $\text{Al}_{0.9}\text{Ga}_{0.1}\text{As}_{0.09}\text{Sb}_{0.91}$. The excitation source is Q-switched Nd:YVO₃ laser, $\lambda=1.064 \mu\text{m}$, with the repetition frequency 200kHz, pulse duration $\sim 80\text{ns}$, and the average power 80-170 mW.

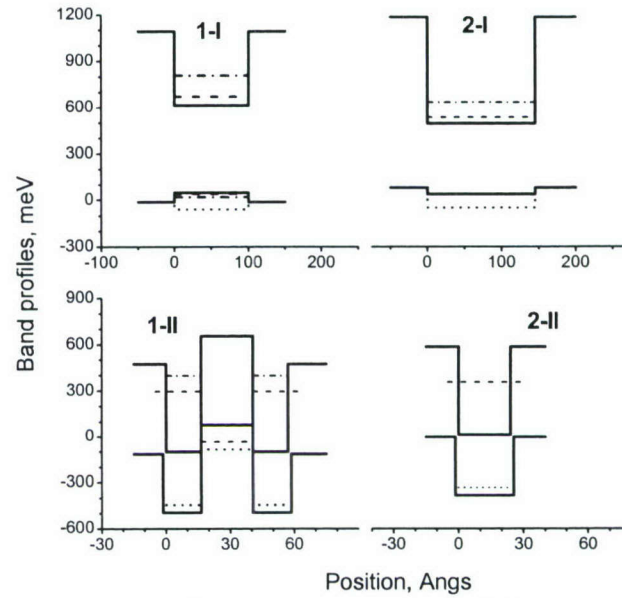


Figure 19. Band profiles and energy levels of the structures. Solid line shows band positions for conduction and heavy-hole bands, dotted line shows the light-hole band split by the strain. Level positions: dashed line – first (lowest) levels of electrons and holes, dashed-dotted lines – second levels.

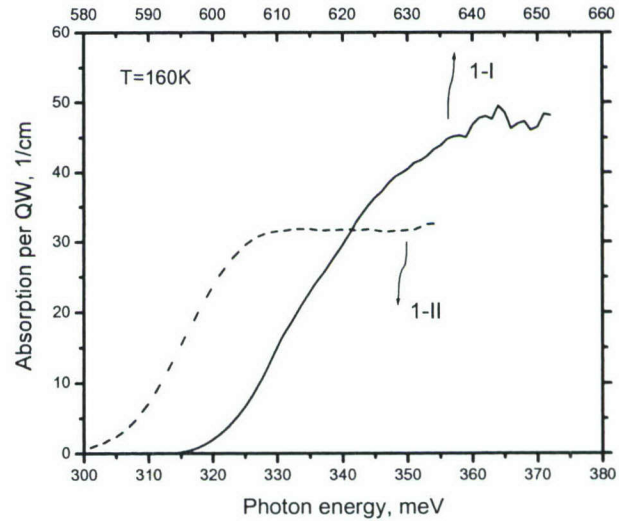


Figure 20. Optical absorption per quantum well for samples 1-I (dashed line) and 1-II (solid line).

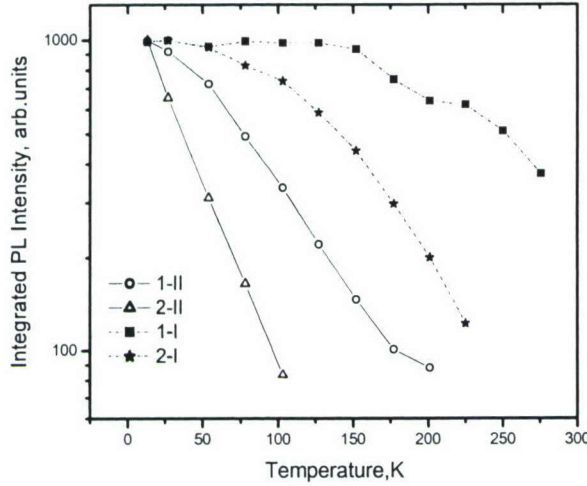


Figure 21. Integrated photoluminescence intensity as a function of temperature. Pumping power density is $\sim 200 \text{ W/cm}^2$ per well.

correlates well with calculations [1]. We, therefore, rule out the reduced optical gain as a mechanism for the inferior temperature performance of type-II mid-IR lasers.

To study the recombination in type-I and type-II structures, we measured the integrated PL intensity as a function of temperature; see Figure 21. For convenience, all the curves are normalized to the lowest-temperature value. The high-temperature decay of the PL is due to thermal depopulation of the quantum wells. Our data are consistent with the model [36,37], data [38] and recent results of Ongstad et al. (to be published in JAP), which demonstrate the important role of the hole escape for temperature performance of type-II lasers. The strength of the PL temperature quenching in each group of structures correlates well with the degree of the hole confinement. The smaller the hole confinement energy, the stronger is the temperature decrease of the PL intensity.

The character of temperature dependence of the PL correlates with T_0 values for studied laser structures. Structure 2-II, intentionally designed with no hole confinement, shows stronger PL temperature decay and lower $T_0=39\text{K}$ [32] than structure 1-II ($T_0=49.3\text{K}$) [33], where the hole confinement energy was calculated as 80 meV. From Figure 21 one can see that temperature decay of PL is generally stronger for type-II samples. Besides, there is a major difference in the shape of the curves between type-I and type-II samples. While in 1-I structure with strong hole confinement the PL decay starts at about 170K, the structure 1-II, where the hole confinement is even higher, shows a decrease in the PL intensity, starting from the lowest experimental temperature of 13K. The same relation holds for structures 2-I and 2-II with no hole confinement. In the structure 2-I the integrated PL intensity is almost temperature independent up to 50K, while in 2-II the PL intensity drops 3 times in the same temperature range. Low temperature sensitivity of integrated PL intensity in type-I structures can be explained assuming that the radiative recombination is the main process determining the steady state carrier

Absorption spectra were obtained from the PL spectra collected from the edge of the sample while a fixed-sized pumped region was moved to a varying distance from the edge [35]. This technique allows measuring the absorption spectrum of a structure containing small number of quantum wells. Figure 20 shows the absorption spectra for type-I (1-I) and W type-II (1-II) samples. The results of the measurements were renormalized with respect to the number of quantum wells and optical confinement in the absorbing structures. The maximum absorption per quantum well in the type I structure was only about 50% higher than in type-II structure. This makes the optical matrix element in type-II structures only 1.2 times lower than in type I structures, which

concentration in the quantum wells. Under this condition, the temperature decrease of radiative recombination rate is compensated by corresponding increase of steady state carrier concentration and the resulting temperature dependence of the integrated PL is weak. At higher temperatures, thermally activated carrier escape leads to PL quenching. The nature of the observed difference in temperature dependencies of photoluminescence for type-I and type-II structures is not yet fully understood. One of the possibilities to be considered is an excessive nonradiative losses which can be associated with interface assisted recombination in narrow QWs [39,40].

Summary

1. An ultra-sensitive single-pass measurement technique was developed for the first time for interband optical absorption measurements in thin layered laser heterostructures. This technique allows absorption measurement even in single-quantum-well laser heterostructures.
2. Direct experimental information about the optical matrix elements in type-I and type-II laser structures was obtained by using single-pass interband optical absorption measurements. This information allows identification of the source of temperature sensitivity of the threshold current in type-II mid-IR GaSb-based semiconductor lasers. Our PL experiments also show that the PL temperature decay is noticeably stronger for type-II samples which indicates the presence of strong nonradiative recombination at elevated temperatures.

Widely tunable type-II interband cascade laser

Tunable semiconductor mid-IR lasers are in high demand for various military and civilian applications, such as free space communication, remote sensing, and environmental monitoring. Electrical tuning is the most direct and robust method of changing the emission wavelength and provides the fastest time response and the finest wavelength adjustment. Two methods of the electrical tuning are often employed in tunable laser design: injection current control of the modal refractive index [41,42], and direct alteration of the laser emission wavelength by an external electric field (Stark effect) [43-46]. The former approach is capable of single-mode tuning that ideally is limited by the spectral width of the material gain. The Stark effect, on the other hand, can provide electrical tuning of the spectral position of the whole gain curve. Above the lasing threshold, however, both methods are severely suppressed by concentration pinning in the laser active region, so that the Stark-effect tuning becomes non-effective and cannot be practically used without imposing significant complications to the laser structure, including, e.g., multi-sectioned waveguide designs [41,45] and the necessity of longitudinal or vertical section integration.

This significant limitation can be avoided by separating the injected carriers into two groups: one that produces the radiation, and the other, accumulated outside the optically active layers, that serves as the source of the controlling electric field. In an earlier work [46] this was accomplished by introducing two additional (electron and hole) accumulation quantum wells grown on both sides of an active type-I quantum well in a diode laser. A significant drawback of the device, however, was its narrow range of tunability (5nm) [46] due to the small second order Stark shift of the energy levels in type-I quantum wells. In this paper, we propose to employ type-II interband cascade structures which are characterized by an inherently strong first-order Stark effect. Indeed, in a type II structure, the recombining electrons and holes are spatially separated, so that there is a nonzero dipole moment in the structure's growth direction even in the absence of the external electric field. Our tunneling-limited injection scheme with a charge accumulation layer outside the optically active type-II heterojunction unclamps the electron-hole concentrations in the active region and allows for an ultra-wide tunable Stark shift of the laser emission even after the laser threshold has been reached.

Each period of the tunable laser cascade structure has 4 separate regions: a digitally graded injector, an (electron) accumulation quantum well, a tunnel barrier, and an optically active type-II heterojunction (see Figure. 22). These regions are designed consistently with one another, so that the emission wavelength depends on the bias current as follows. As the injection current increases above threshold, electrons start accumulating in the superlattice injector well adjacent to the tunnel barrier. (Their concentration determines the tunneling rate into upper energy level, E_2 , of the electron quantum well 2 shown in Figure. 22). Concurrently, injected holes accumulate in the hole quantum well 1. This charge separation results in an electric field (perpendicular to the epi-layers) that increases with the injection current. The energy level positions E_{21} and, hence, the emission wavelength λ , become dependent on the bias current which controls the electric field via charge accumulation. The separation of the charge accumulation layers from the active region [46] enables the wavelength tuning above the laser threshold. At the current densities $J \geq J_{th}$, the maximum net modal optical gain is zero. The concentration in the electron

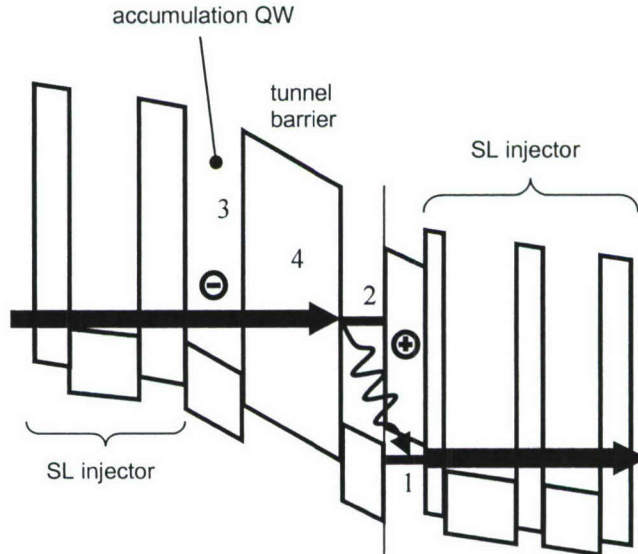


Figure 22: Schematic band diagram of a single period of the IC laser structure under a bias voltage.

accumulation layer 3 can be estimated in a steady state regime by $n_3^{(c)} = J\tau_{\text{tun}}/q$, where τ_{tun} is the tunneling time and q is the electron charge. Using the equation (3), charge neutrality condition, $n_1^{(h)} = n_3^{(c)} + n_2^{(c)}$ and the electron concentration in the active quantum well is related to the injection current density J by the equation:

$$\exp\left(-\frac{n_2^{(c)}}{N_{2D}}\right) + \exp\left(-\frac{n_2^{(c)} + J\tau_{\text{tun}}/q}{P_{2D}}\right) = 1 - \frac{\alpha}{G_0} \quad (4)$$

Note, that as the current density increases above threshold, the electron concentration, $n_2^{(c)}$, in the optically active quantum well (#2 in Figure. 22) slightly decreases and finally saturates at a value determined by the optical loss, temperature, and material constants. On the other hand, the concentration in the electron accumulation layer $n_3^{(c)}$ increases with the current, as does the hole concentration, thus providing the overall charge neutrality and modal gain pinning together with the increase of the electric field in the active type-II heterojunction region. The latter, in turn, affects the laser wavelength tuning above threshold.

The tunable interband cascade (IC) laser structure was grown by MBE on p -doped GaSb substrates. The active region of the laser is a cascade of 14 periods. Each period includes a digitally graded InAs/AlSb injector and InAs/Ga_{0.8}In_{0.2}Sb/GaSb type II heterostructure, separated by a 4nm AlSb barrier. The widths of the InAs and Ga_{0.8}In_{0.2}Sb layers are 2.1nm and 3.1nm, respectively. The active area is sandwiched between InAs/AlSb superlattice claddings. The Ga_{0.8}In_{0.2}Sb layer is followed by a p -doped 5.8-nm GaSb QW which serves as a hole reservoir. The devices are fabricated as deep-etched mesas and soldered, epi-layer side up, to Au-coated copper mounts. The mesas 35 μm wide with 0.5-mm-long cavity lengths with both facets left uncoated. The mounts were attached to the cold finger of a liquid N₂ or He train cryostat. The emission was collected with the reflection optics and analyzed with an FTIR[®] spectrometer. We compared the tuning characteristics of this structure with those of a regular 18-cascade IC laser [26]. The latter had an active region with type II W-like quantum wells and contained no special tunnel barriers for charge accumulation.

The experimental turn-on voltage is ~ 5.2 V and agrees well with the theoretical prediction (4.9V) for an ideal 14-period cascade structure. Calculation shows that

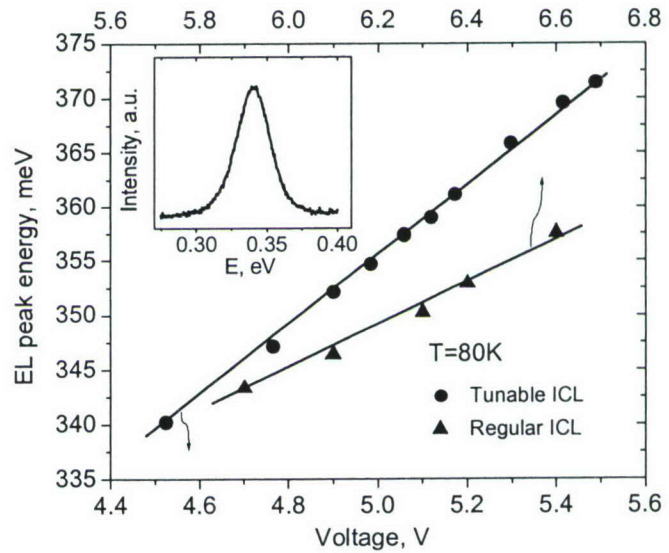


Figure 23: The dependence of the electroluminescence (EL) quantum energy on the bias voltage for a regular IC laser (triangles) and tunable IC laser (circles). The inset shows the EL spectrum at low bias current.

0.35 V voltage drop per each injector region provides for injector level alignment. For 56 nm injectors this corresponds to the turn-on internal electric field of about 65 kV/cm. The width of the tunnel barrier 4 in our design was chosen 4 nm which ensures the alignment of the accumulation level 3 and upper lasing level 2 at turn-on voltage (see Figure. 22). The observed threshold current density is 91 A/cm² at 80 K. The lasers demonstrates cw operation up to 120 K and pulsed operation up to 200 K (pulse duration = 400 ns, duty cycle = 2.4%). The external quantum efficiency is ~250% (80K). The internal loss measured with Hakki-Paoli techniques is ~ 10 cm⁻¹.

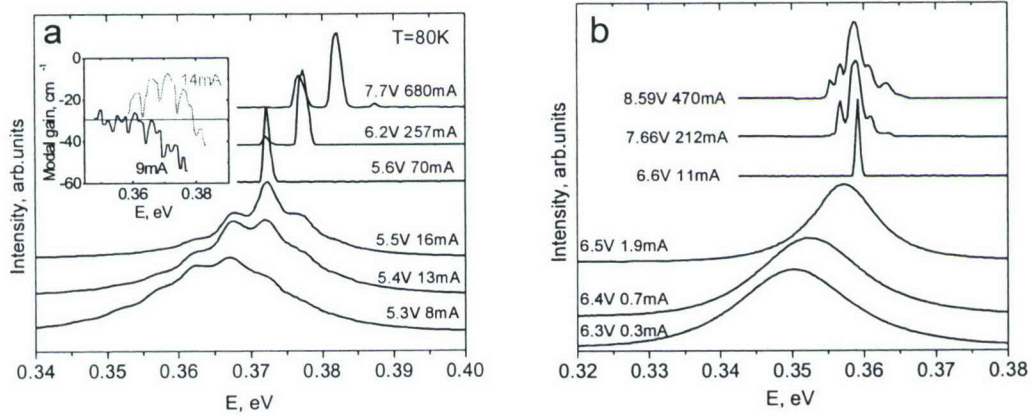


Figure 24: ASE and laser spectra of the tunable IC laser (a) and regular IC laser (b) at different bias currents. The inset in the panel (a) shows the modal gain spectrum of the tunable IC laser.

The electroluminescence (EL) spectrum at low current is shown in the inset of Figure 23. The emission quantum energy is 0.34 eV agrees with the theoretical prediction (0.32eV). The EL spectral maximum energy increases linearly with the bias voltage. Since the dependence is measured in the sub-threshold pumping region, the linear shift can be attributed to the Stark effect that results from charge accumulation in the type II quantum wells of the laser active area. A similar effect has been observed in a regular interband cascade laser (see Figure. 23). The effect is weaker in a regular IC laser due to the lower sensitivity of subband energies in a W-like quantum well with respect to charge accumulation.

Amplified spontaneous emission (ASE) and lasing spectra of both the tunable and the regular IC lasers are shown in Figure 24. In the regular laser, in spite of the ASE blue shift, the laser line spectral position is stable up to high bias currents (~ 220 x threshold values). This is as expected from the pinning of concentration and, hence, of electric field in the active area quantum wells. The lasing spectrum of the tunable laser (see Figure. 24a, three upper curves) demonstrates a clear blue shift. The periodic modulation of the ASE spectrum in the tunable laser is attributed to optical mode leakage into the substrate [24]. This is consistent with the observed strong modulation of the modal gain spectrum with the same period (see Figure. 24a, inset). The spectral positions of the gain maxima and minima are determined by the substrate thickness as well as the effective refraction indices of the active area, claddings and substrate. The dependence of these positions on the bias current is weaker than the direct Stark shift of the gain spectrum. As the bias current increases, the material gain curve shifts with respect to the

modulation extremes and consequently, the modal gain maximum shows a discrete blue shift with the increment equal to the leaky mode modulation period. This behavior takes place at the pumping level far higher than the laser threshold. The lasing spectrum of the tunable laser demonstrates a clear blue shift at increasing bias current. The rate of this shift with respect to the bias current (and voltage) is slower than the rate of ASE tuning in the subthreshold region (approximately 5 meV/V vs. 30 meV/V). This indicates an abrupt change in the tuning mechanism as the bias current exceeds the laser threshold. In the subthreshold regime, the wavelength shift is determined primarily by the carrier accumulation in the optically active quantum wells and is related to the corresponding increase of the internal electric field in the type-II heterojunction. After the laser threshold has been reached, the wavelength tuning becomes determined by the charge buildup in accumulation quantum well 3, which, in turn, depends on the electron tunneling rate through barrier 4. The change in the tuning rate above the threshold indicates that, in the present design, the rate of charge accumulation in quantum well 3 is lower than that in the optically active quantum wells below the threshold. Figure 25 demonstrates the laser spectrum shift recorded throughout the whole range of the injection current (1-42 threshold values) without noticeable saturation. The maximum value of the laser emission tuning range is 15 meV or 120 nm.

In conclusion, we have demonstrated an electrically tunable interband cascade laser that operates in the mid-IR spectral range. The laser design includes an additional charge accumulation layer located outside the optically active quantum wells. This eliminates the electron-hole concentration pinning and thus enables an ultra-wide Stark shift of the optical gain spectrum. The tuning range of our device is 120nm (starting from the initial lasing wavelength $\lambda \sim 3.33 \mu\text{m}$), or 120 cm^{-1} . We believe the laser tuning performance can be further improved by suppressing the gain spectrum modulation due to the substrate leaky modes.

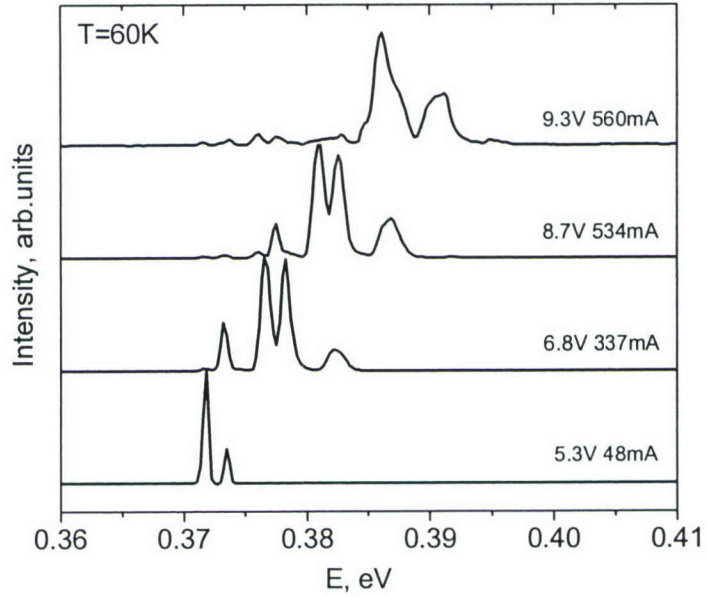


Figure 25: Lasing spectra of the tunable IC laser at different values of the injection current

Temperature insensitive semiconductor quantum dot laser

High temperature stability of operation is an essential feature required of long wavelength semiconductor heterostructure lasers for telecommunications. Commercial lasers with either bulk or quantum well active regions suffer from rather poor temperature stability. The empirical parameter $T_0 = 1/(\partial \ln j_{th}/\partial T)$, which describes the T -dependence of the threshold current j_{th} , rarely exceeds 100 K in best commercial lasers. One of the main advantages of the quantum dot (QD) lasers, proposed years ago was high temperature stability. Although the best results for T_0 in QD lasers are quite respectable, so far they have been nowhere near the predicted “infinite” values that would allow regarding the laser as temperature insensitive.

We proposed [47] and patented [48] a novel approach, based on spatially separating the reservoirs of electrons and holes from which the dots are fed with carriers. This can be accomplished in at least two ways by special tailoring of the laser heterostructures. A particularly favorable way of accomplishing this is by using resonant-tunneling injection of majority carriers into quantum dots, Figure. 26.

In the proposed structure carriers cannot bypass the QDs on their way from one QW to another. Therefore, the density of minority carriers in the abutting reservoirs will be negligible. This means that outside the QDs there will be no region in the structure where both electron and hole densities are simultaneously high. The electron density is high where the hole density is negligible and vice versa. This strongly suppresses the parasitic components of the threshold current, which would otherwise give the main contribution to the temperature dependence. We can expect only a slight residual temperature dependence of j_{th} caused by the inhomogeneous line broadening. The proposed approach has been taken up by several groups [49] with very encouraging results. Our MURI partners from Michigan reported $T_0 = 363$ K at room temperature [50].

Task #3: Phonon Enhancement To Carrier Transport In Interband Cascade Lasers: Project Leader: Shin-Shem Steven Pei (U. of Houston)

Co-participants: H. Maris (theory of ballistic phonons, and thermal management), S. Luryi (theory of tunneling), Industry/Gov't Lab Link: Lincoln Laboratory

1 – INTRODUCTION: CURRENT STATUS OF TYPE-II IC LASERS

Since the concept of the type-II IC laser was first proposed in 1994, many experimental and theoretical works have been reported. Mid-IR ($\sim 4\mu\text{m}$) electroluminescence (EL) was first observed in 1996 from an IC laser structure at temperatures up to 300K. In early 1997, the Sb-based type-II IC laser ($\sim 3.8\mu\text{m}$ at 80 K) was first demonstrated at temperatures up to 170 K. The observed emission wavelength from IC LEDs at room temperature was extended to $15\mu\text{m}$, demonstrating the unique capability of Sb-family type-II QW structures to be tailored over a wide spectral range. Recently, an Army research lab has reported some significant advances on electrically pumped type-II IC lasers comprising 18 cascade stages (lasing wavelength from 3.3

μm to $3.5 \mu\text{m}$ in temperatures ranging from 80K to 300K), achieving high peak output power ($\sim 6 \text{ W/facet}$ at 80K), high operation temperature (up to 300K in the pulsed mode and up to 150 K in the CW mode), and low threshold current density ($\sim 13.1 \text{ A/cm}^2$ and 15 A/cm^2 at 80K under pulsed and CW conditions, respectively)

II – CARRIER TRANSPORT

In order to improve the performance of the electrically-pumped type-II interband cascade laser structure, better understanding of carrier transport under external bias is one of the critical factors in laser design. Due to the unique type-II broken band gap alignment as shown as Figure [1-5] there are several important carrier transport processes between quantum wells, as mentioned in chapter I. They are: the resonant tunnelling from the miniband in the injection region to the electron's ground quasi-bound state in the InAs well of the active region; the interband tunneling from the hole states of the active regions to the miniband of the injection region; the phonon-assisted carrier transition between the hole states of the InGaSb and GaSb wells. In this chapter, these 3 types of carrier transport processes will be discussed in detail.

2.1 Resonant tunnelling from the miniband in the injection region to the electron's ground quasi-bound state in the InAs well of the active region

This resonant tunneling happens between the miniband of the injection region and the electron ground quasi-bound state in the InAs well of the active region (as Figure [1-4]). It's a kind of intraband resonant tunneling within the conduction band. The theoretical basis of the resonant tunnelling process is that both the energy and momentum parallel to the barriers are conserved.

In the case of this intraband resonant tunneling process, the energy and the parallel momentum conserved are shown in figure 2-1. The thick dark lines represent the electrons involved in the resonant tunnelling process, and the two dotted lines represent the top and the bottom of the miniband, respectively. As we know, the tunnelling current density is proportional to the number of the electrons which would take part in the resonant tunnelling process. The dot dash lines E_c are the energy of the electron's ground quasi-bound state in the InAs well of the active region.

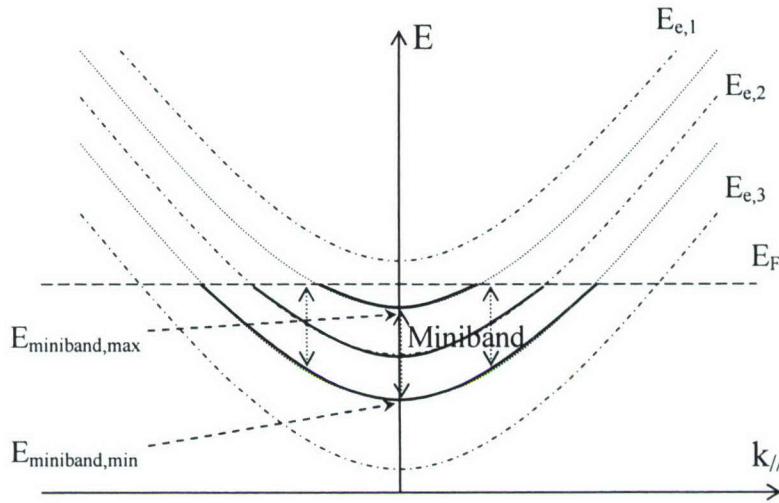


Figure 2-1 the tunnelling process between the miniband and the electron's ground quasi-bound state of the InAs well at the active region. The electron tunneling direction is from E_{miniband} to $E_{e,1}$, $E_{e,2}$, $E_{e,3}$.

If $E_{\text{miniband, max}} > E_e > E_{\text{miniband, min}}$, (as $E_{e,2}$ in figure 2-1), then the resonant tunnelling occurs and the transmission probability almost reaches 100%. When $E_e = E_{\text{miniband, min}}$, a maximum numbers of electrons are involved into the tunneling process which will result in a maximum tunneling current. If the energy E_e of the electron's ground quasi-bound state at the InAs well of the active regions is above the maximum of the miniband of the injection region (as $E_{e,1}$ in figure 2-1) or E_e falls below the minimum of the miniband (as $E_{e,3}$ in figure 2-1), then tunneling probability will decrease exponentially and the tunneling time will increase exponentially with the energy separation of E_e and the miniband.

2.2 Interband resonant tunneling process from the light-hole state of the active region to the miniband of the injection region

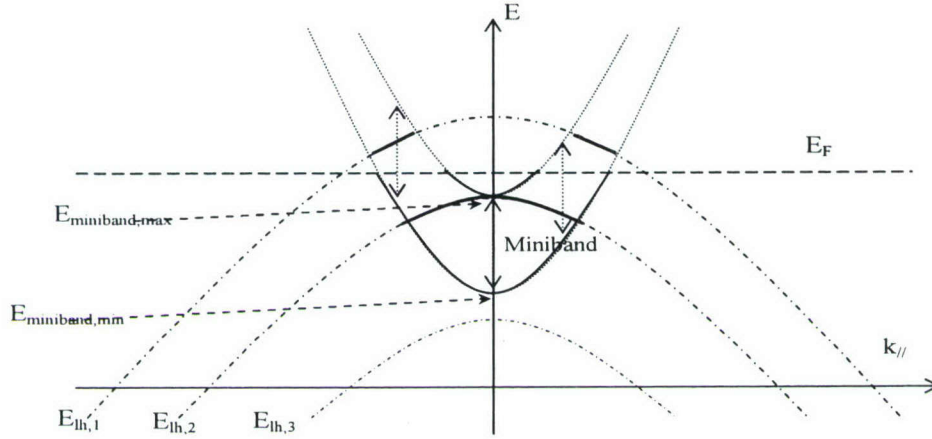


Figure 2-2: The tunnelling process between the light-hole ground quasi-bound state of GaSb and the miniband. The electron tunneling direction is from E_{lh} to $E_{miniband}$.

In the case of interband resonant tunneling process from the light-hole(LH) state to the miniband, the conservation of the energy and the parallel momentum is shown in figure 2-2. In this case, the structure between the hole-wells (InGaSb & GaSb) and the injection regions looks like a kind of p-n junction with a reverse bias. According to $\mathbf{k} \cdot \mathbf{p}$ theory, the coupling between the conduction and light-hole bands is stronger than the coupling between the conduction and heavy-hole (HH) bands near the Brillouin zone center. At $k_{||}=0$, there is only coupling between the conduction and the light-hole bands. Therefore, the light-hole quasi-bound state in GaSb is regarded as the dominative channel to remove the electrons from the active region into the injection region.

If the energy E_{lh} of the light-hole's ground quasi-bound state of GaSb is below the bottom of the miniband of the injection region (as $E_{lh,3}$ in figure 2-2), then the carriers face a barrier as thick as the whole length of the injection region, which will block the carriers of the GaSb wells tunnelling to the injection region and slow down the tunnelling process. If $E_{miniband, max} > E_{lh} > E_{miniband, min}$, (as $E_{lh,2}$ in figure 2-2), then resonant tunnelling occurs and the tunneling time becomes very short. When $E_{lh} = E_{miniband, max}$, the tunneling current reaches the maximum because maximum carriers are involved in the tunneling between the GaSb well and the injection region at this moment; after E_{lh} rises above the top of the miniband (as $E_{lh,1}$ in figure 2-2), the resonant tunnelling current density will decrease but never shut off because the lh energy band whose curvature is opposite to the curvature of e energy band is almost fully occupied by electrons. This case is similar to the p-n structure under a high reverse bias. Under an external bias, the electrons on lh state can go to the e states of the miniband which are not fully occupied. Thus, the alignment of the miniband with electron ground quasi-bound state at InAs of the active region is more critical than with the lh ground quasi-bound state at GaSb.

2.3 Phonon-assisted resonant tunnelling between InGaSb and GaSb

The electrons involved in the resonant tunneling process stay in a quantum well structure for a dwell time ranging from a few tens of femtoseconds to a few hundred nanoseconds depending on the structural parameters. While in the structure, the electrons may suffer from scattering processes which cause momentum and energy relaxations which break the phase-coherence. Several possible causes exist for this sort of phase-coherence breaking scattering: electron-phonon interactions, residual impurity scattering, disorder scattering, and so on.

Interactions between electrons and LO-phonons are in general the most important energy dissipation processes in polar semiconductor systems. The electrons in the quantum well structure may emit or absorb LO-phonons during the resonant tunneling process. As this is an inelastic scattering process the electrons involved do not conserve the components of momentum either parallel or perpendicular to the barriers.

2.4 Carrier transport in type-II ICLs under an external bias based on linear-band approximation

In Chapter I, the schematic carrier transport has been shown in Figure [1-4] under the flat band condition. However, in the electrically pumped type-II IC lasers, how can carrier transport take place when an external bias is present in the real laser devices?

In previous theoretical investigations of the band structure of ICLs, people usually used linear band profiles assuming that the electrical fields are uniform along the whole laser structures. They didn't take into consideration of the built-in electric field generated by the carriers. In the following, the results based on the linear band profile will be shown, and it will be illustrated how the linear band approximation failed to explain the carrier transport in type-II ICLs.

In this dissertation, a typical type-II ICL structure was investigated. In order to satisfy the bound wavefunction condition at both ends, in our calculation we assumed two 200nm thick and 10eV high potential barriers to sandwich three stages of the type-II ICL structure having a total of 66 layers. The two imaginary barrier layers may distort the band profiles of the first and third stages, but have little impact on the band profiles of the second stage, so only the second stage would be discussed in this paper.

Figure 2-3 shows its linear band profile at $T=80\text{K}$ under a 75kV/cm external bias (corresponding to a bias of 0.5V/period), which is the actual device's lasing bias. The dotted line is degenerated light-hole valence band edge under strain.

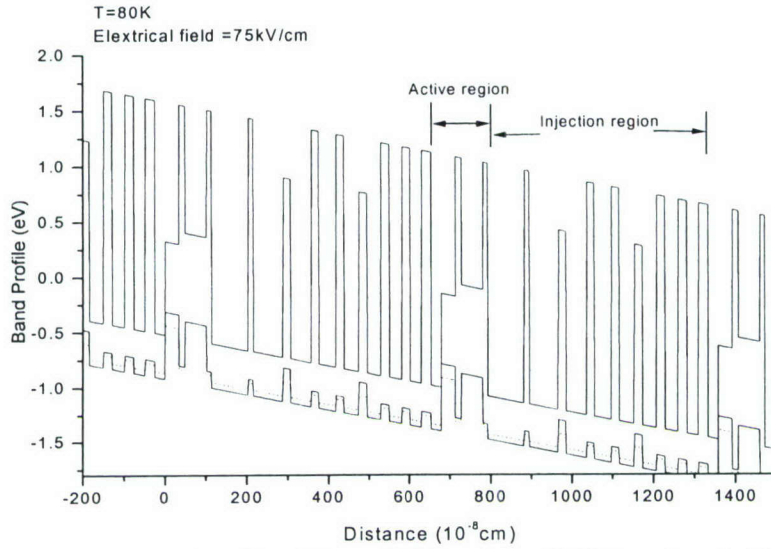


Figure 2-3. The linear band profile of Type-II ICL under a -75kV/cm electrical field at 80K

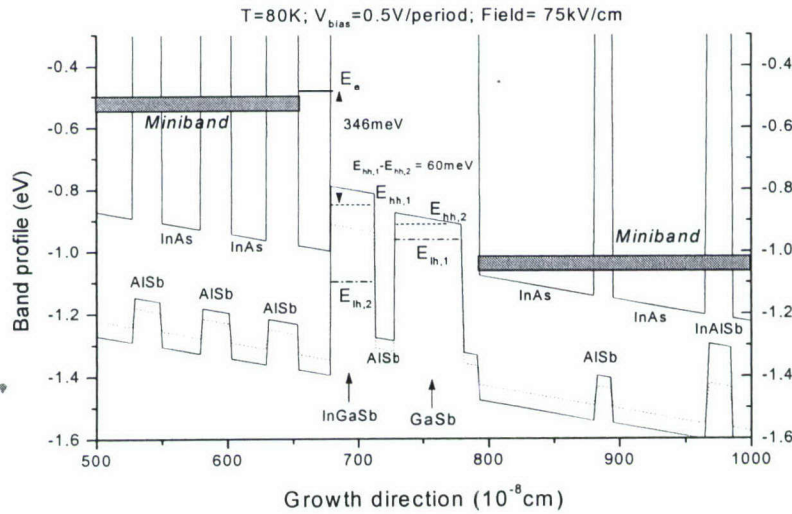


Figure 2-4. Energy levels alignment based on the linear band profile of type-II ICL under a -75kV/cm electrical field at 80K

Figure 2-4 gives the details of energy level alignments based on the linear band profile approximation. The shadow areas are the minibands of the injection regions. The solid short line E_e represents the ground electron state in the InAs well of the active region, the dotted line E_{hh} , and the dash-dotted line E_{lh} respectively represent the heavy hole and the light hole energy states in InGaSb and GaSb wells.

Layer	The Active region				Injection region	Next active region
Energy level	e_l	hh_l	hh_2	lh_l	<i>miniband</i>	e_l
Linear approximation 80K	346	0	-59	-110	-215→-170	-154

Note: "next active region" represents the active region of the next period.

Table 2-1. The energy separation relative to the ground heavy hole energy level hh_l of the active region.
(Unit: meV)

Table 2-1 shows the energy separation relative to the ground heavy hole energy level hh_l of the active region. It shows that the ground electron state e is about 16meV above the top of the miniband at the last injection region. Then the resonant tunneling process won't occur between the miniband and the InAs well of the active region so that the injection efficiency from the injection region to the active region will be low. Additionally, the energy separation between the first two heavy hole states hh_l and hh_2 in InGaSb and GaSb wells is about 59meV, which is much bigger than the interface LO-phonon energy (about 40meV). Neither the resonant tunneling process nor the phonon-assisted resonant tunneling process can happen between the InGaSb and GaSb wells. Then the electrons on the ground heavy hole state HH_l of the InGaSb well can't be expelled to GaSb well quickly. Thus, the population inversion is difficult to achieve.

Obviously the linear energy band profile can't explain the carrier transport in the type-II ICL device during the lasing operation. The reason is that the linear band profile approximation doesn't consider the carrier distribution in the laser diodes. However, the carrier distribution in the laser structure will induce the built-in electric field and bend the energy band profile. Therefore, a more accurate band structure model is highly desirable to achieve the designed wavelength, reduced Auger recombination and optimum carrier transport. In this dissertation, the carrier distribution and the built-in electrical field will be considered, and an improved self-consistent modeling will be presented in the following chapter.

3 – SELF-CONSISTENT MODELING

In order to investigate the effect of carrier distribution on band structure, self-consistent modeling will be applied to the calculation. In this self-consistent calculation, the energy-band diagram and the carrier distribution in type-II ICLs are simulated by simultaneously solving three one-dimensional time-independent Schrödinger equations (eq. 3-1) (respectively for electrons, heavy holes and light holes). and one Poisson equation (eq. 3-2)

3.1. Model:

3.1.1 Schrödinger equation

The effective mass, one-dimensional Schrödinger equation is given by

$$\left[-\frac{\hbar^2}{2} \frac{d}{dz} \left(\frac{1}{m^*(z)} \frac{d}{dz} \right) + V(z)\right] \psi_j(z) = E_j \psi_j(z) \quad (3-1)$$

$$V(x) = V_b(z) + V_H(z) + V_{ex}(z) \quad (3-2)$$

where E_j is the eigenenergy, $\psi_j(z)$ is the wavefunction corresponding to the eigenenergy E_j . m^* is the effective mass, and \hbar is Planck's constant.

$V_b(z)$ is the band profile of the one-dimensional structure. $V_{ex}(z)$ is the local exchange-correlation energy calculation in the LDA approximation using the Hedin-Lundqvist parametrization.

$$V_{ex}(z) = -\frac{R_y^*}{10.5\pi\alpha r} \left[1 + 0.7734 r \ln\left(1 + \frac{1}{r}\right)\right] \quad (3-4)$$

where we have defined

$$\alpha = (4/9\pi)^{1/3}, \text{ and } r = \frac{1}{21} \left(\frac{4}{3} \pi a_B^* n(z)\right)^{-1/3}.$$

$\alpha_B^* = 4\pi\epsilon_0\kappa\hbar^2 / m^* e^2$ and $R_y^* = e^2 / (8\pi\epsilon_0\kappa a_B^*)$ are respectively the effective Bohr radius and the effective Rydberg's constant. κ is the local dielectric constant.

$n(z)$ is the electron density.

$V_H(z)$ is the Hartree potential which is obtained by solving the one-dimensional Poisson equation
3.1.2 Poisson's equation

Poisson's equation can be written as

$$\frac{d^2}{dz^2} V_H(z) = \frac{e}{\epsilon_0\kappa(z)} [N_D(z) - n(z) + p(z) - N_A(z)] \quad (3-5)$$

along with the boundary conditions

$$V_H(z = z_L) = 0, \quad (3-6)$$

$$V_H(z = z_R) = \sum_{i=1}^{n-1} \Delta V_i, \quad (3-7)$$

where ΔV_i is the band offset at the i th interface. N_D , N_A is respectively the dopant and acceptor density. $n(z)$ and $p(z)$ is the carrier (electron and hole) density.

3.1.3 The carrier density and the Fermi level

The electron and hole density $n(z)$ and $p(z)$ can be written as

$$n(z) = \sum_j n_j(z) |\psi_{e_j}(z)|^2 \quad (3-8)$$

$$p_{hh, lh}(z) = \sum_j p_{hh, lh_j}(z) |\psi_{hh, lh_j}(z)|^2 \quad (3-9)$$

where the sum runs over the different subbands.

The subband occupations n_j and p_{hh, lh_j} are given by

$$n_j(z) = \frac{k_B T m_{e_j}^*(z)}{2\pi} \ln[1 + \exp(\frac{E_F - E_{e_j}}{k_B T})] \quad (3-10)$$

$$p_{hh, lh_j}(z) = \frac{k_B T |m_{hh, lh_j}^*(z)|}{2\pi} \ln[1 + \exp(\frac{-E_F + E_{hh, lh_j}}{k_B T})] \quad (3-11)$$

The Fermi level E_F is obtained from the solution of the space charge neutrality condition

$$\int_{z_L}^{z_R} [N_D(z) - n(z) + p_{hh}(z) + p_{lh}(z) - N_A(z)] dz = 0 \quad (3-12)$$

3.2 Dimensionless

Using α_B and R_y as the units of length and energy respectively, we define reduced L and z by rescaling the layer thickness L_0 and the position coordinate Z_0 with the effective Bohr radius α_B ($L = L_0 / \alpha_B$, $Z = Z_0 / \alpha_B$). Furthermore, we introduce reduced E and V by rescaling energies (E) and potentials (V) with the effective Rydberg's constant R_y ($E = E / R_y$, $V = V / R_y$). On the other hand, reduced charge density n , p and temperature T are defined by rescaling charge density N, P , and temperature T with $(a_B)^{-3}$, and R_y . ($n = n / (a_B)^{-3}$, $T = T / R_y$)

With these new variables, previous equations can be rewritten.

Schrödinger equation:

$$[-\frac{1}{m_e^*(z)} \frac{d^2}{dz^2} + V_e(z)] \psi_{e_j}(z) = E_{e_j} \psi_{e_j}(z) \quad (3-13)$$

$$[-\frac{1}{m_{hh}^*(z)} \frac{d^2}{dz^2} + V_{hh}(z)] \psi_{hh_j}(z) = E_{hh_j} \psi_{hh_j}(z) \quad (3-14)$$

$$[-\frac{1}{m_{lh}^*(z)}\frac{d^2}{dz^2} + V_{lh}(z)]\psi_{lh,j}(z) = E_{lh,j}\psi_{lh,j}(z) \quad (3-15)$$

Here, let $m_e^* > 0$, and let m_{hh}^* & $m_{lh}^* < 0$

Poisson equations:

$$\frac{d^2}{dz^2}V_{eH}(z) = \frac{8\pi}{\kappa(z)}[N_D(z) - n(z) + p(z) - N_A(z)] \quad (3-16)$$

Carrier density:

$$n_j(z) = \frac{k_B T m_e^*(z)}{2\pi} \ln[1 + \exp(\frac{E_F - E_{e,j}}{k_B T})] \quad (3-17)$$

$$p_j(z) = \frac{k_B T |m_{hh}^*(z)|}{2\pi} \ln[1 + \exp(\frac{-E_F + E_{hh,j}}{k_B T})] \quad (3-18)$$

The local exchange-correlation energy $V_{ex}(z)$:

$$V_{ex}(z) = -\frac{2m^*}{21\pi\alpha\kappa^2}[\frac{1}{r} + 0.7734r \ln(1 + \frac{1}{r})] \quad (3-19)$$

3.3 Discretization

In our calculation, we calculate 3 periods of active and injection regions, which were sandwiched by two 200nm thick and 10eV high potential barriers. Due to the complexity of type-II IC laser structures, if a uniform mesh was used to discretize the Schrödinger's equation, more than 5000 nodes would be required in the self-consistent calculation. To reduce the computation time and provide faster convergence, a nonuniform mesh was adopted. A denser mesh was used in the active regions, due to the higher accuracy required there, but a less dense mesh was adopted in the less critical regions such as barrier layers. By using the nonuniform mesh, the number of nodes could be decreased by about a factor of 1000, but this would destroy the symmetry of the three 1000×1000 matrices used for the discretized Schrödinger equations. Therefore, a matrix transformation was used to preserve the symmetry of the discretized Schrödinger equations. This method simplifies solving these huge discretized differential equations significantly.

In our calculation, the effective Bohr radius α_B and the effective Rydberg's constant R_y are used as the units of length and energy, respectively.

3.3.1 Formulation for the Schrödinger equation

In order to numerically solve the Schrödinger equation, we discretized the different equations by using a three-point finite difference scheme as the following:

For the nodes, which are not at the interface and not the neighbors of the interface, i.e. $z_i \neq z_{\eta}, z_{\eta-1}, z_{\eta+1}$, where z_{η} is the position of the interface,

$$-\frac{1}{m^* d^2} \psi_j(z_{i-1}) + [\frac{2}{m^* d^2} + V(z_i)] \psi_j(z_i) - \frac{1}{m^* d^2} \psi_j(z_{i+1}) = E_j \psi_j(z_i) \quad (3-20)$$

For the nodes at interface or its neighbors, the current continuity condition $-\frac{1}{m^*} \frac{d}{dz} \psi_j(z) \Big|_{z=z_{\eta}}$ can be discretized as

$$\psi(z_{\eta}) = \frac{\psi(z_{\eta-1}) + \alpha_{LR} \psi(z_{\eta+1})}{1 + \alpha_{LR}} \quad (3-21)$$

where $\alpha_{LR} = m_L^* d_L / m_R^* d_R$, and d_L and d_R are the mesh sizes of the left and right sides of the interface, respectively; m_L^* and m_R^* are the effective masses at the both sides of the interface.

Then the discretized equation at $z=z_{\eta-1}$ and $z_{\eta+1}$ can be written as

$$-\frac{1}{m_L^* d_L^2} \psi_j(z_{\eta-2}) + [\frac{1}{m_L^* d_L^2} (2 - \frac{1}{1 + \alpha_{LR}}) + V(z_{\eta-1})] \psi_j(z_{\eta-1}) - \frac{1}{m_L^* d_L^2} \frac{\alpha_{LR}}{1 + \alpha_{LR}} \psi_j(z_{\eta+1}) = E_j \psi_j(z_{\eta-1}) \quad (3-22)$$

$$-\frac{1}{m_R^* d_R^2} \frac{1}{1 + \alpha_{LR}} \psi_j(z_{\eta-1}) + [\frac{1}{m_R^* d_R^2} (2 - \frac{\alpha_{LR}}{1 + \alpha_{LR}}) + V(z_{\eta+1})] \psi_j(z_{\eta+1}) - \frac{1}{m_R^* d_R^2} \psi_j(z_{\eta+2}) = E_j \psi_j(z_{\eta+1}) \quad (3-23)$$

The above Schrödinger equations can be written in matrix notation as

$$A \psi = E \psi \quad (3-24)$$

$$\begin{pmatrix}
a_{11} & a_{12} & 0 & 0 & \cdot & \cdot & \cdot & \cdot & 0 & 0 \\
a_{21} & a_{22} & a_{23} & 0 & 0 & \cdot & \cdot & \cdot & 0 & 0 \\
0 & a_{32} & a_{33} & a_{34} & 0 & 0 & \cdot & \cdot & 0 & 0 \\
\cdot & \cdot & \cdot & \cdot & \cdot & \cdot & \cdot & \cdot & \cdot & \cdot \\
\cdot & \cdot & \cdot & \cdot & \cdot & \cdot & \cdot & \cdot & \cdot & \cdot \\
\cdot & \cdot & \cdot & \cdot & \cdot & \cdot & \cdot & \cdot & \cdot & \cdot \\
\cdot & \cdot & \cdot & \cdot & \cdot & \cdot & \cdot & \cdot & \cdot & \cdot \\
\cdot & \cdot & \cdot & \cdot & \cdot & \cdot & \cdot & \cdot & \cdot & \cdot \\
\cdot & \cdot & \cdot & \cdot & \cdot & \cdot & \cdot & \cdot & \cdot & \cdot \\
\cdot & \cdot & \cdot & \cdot & \cdot & \cdot & \cdot & \cdot & \cdot & \cdot
\end{pmatrix} \times \begin{pmatrix} \psi(z_1) \\ \cdot \\ \cdot \\ \psi(z_{\eta-2}) \\ \psi(z_{\eta-1}) \\ \psi(z_{\eta+1}) \\ \psi(z_{\eta+2}) \\ \cdot \\ \cdot \\ \psi(z_n) \end{pmatrix}$$

$$= E \times \begin{pmatrix} \psi(z_1) \\ \cdot \\ \cdot \\ \psi(z_{\eta-2}) \\ \psi(z_{\eta-1}) \\ \psi(z_{\eta+1}) \\ \psi(z_{\eta+2}) \\ \cdot \\ \cdot \\ \psi(z_n) \end{pmatrix}$$

$$A = \begin{pmatrix}
a_{11} & a_{12} & 0 & 0 & \cdot & \cdot & \cdot & \cdot & 0 & 0 \\
a_{21} & a_{22} & a_{23} & 0 & 0 & \cdot & \cdot & \cdot & 0 & 0 \\
0 & a_{32} & a_{33} & a_{34} & 0 & 0 & \cdot & \cdot & 0 & 0 \\
\cdot & \cdot & \cdot & \cdot & \cdot & \cdot & \cdot & \cdot & \cdot & \cdot \\
\cdot & \cdot & \cdot & \cdot & \cdot & \cdot & \cdot & \cdot & \cdot & \cdot \\
\cdot & \cdot & \cdot & \cdot & \cdot & \cdot & \cdot & \cdot & \cdot & \cdot \\
\cdot & \cdot & \cdot & \cdot & \cdot & \cdot & \cdot & \cdot & \cdot & \cdot \\
\cdot & \cdot & \cdot & \cdot & \cdot & \cdot & \cdot & \cdot & \cdot & \cdot \\
\cdot & \cdot & \cdot & \cdot & \cdot & \cdot & \cdot & \cdot & \cdot & \cdot \\
\cdot & \cdot & \cdot & \cdot & \cdot & \cdot & \cdot & \cdot & \cdot & \cdot
\end{pmatrix}$$

As we mentioned previous, a nonuniform mesh was adopted in the self-consistent calculation of type-II ICL due to the complexity of its structure. In such a case, where d_L is not equal to d_R in general, then the matrix A in the above equation becomes a non-symmetry tridiagonal $(N-N_L-1) \times (N-N_L-1)$ matrix and more difficult to be solved. Here N is defined as the total number of nodes and N_L is the number of layers. Using a proper matrix transformation allows us to preserve the symmetry of the discretized Schrödinger equation. We define two diagonal matrices M and L ,

$$M_{i,j} = \begin{cases} d_i & i = j \\ 0 & i \neq j \end{cases}, \quad (3-25)$$

$$L_{i,j} = \begin{cases} \sqrt{d_i} & i = j \\ 0 & i \neq j \end{cases}, \quad (3-26)$$

and matrix $B = M \times A$. As the product of a diagonal and tridiagonal matrix, B is tridiagonal. It also is easily seen that B is symmetric. This provides the desired transformation

$$B \psi = M A \psi = E M \psi \quad (3-27)$$

Then we get

$$L^{-1} B L^{-1} L \psi = L^{-1} B \psi = L^{-1} L L A \psi = E L \psi \quad (3-28)$$

Let matrix H and ϕ

$$H = L^{-1} B L^{-1} \quad (3-29)$$

$$\Phi = L \psi \quad (3-30)$$

Then, we have

$$H \phi = E \phi \quad (3-31)$$

It can be seen that

$$H_{i,j} = (L^{-1} B L^{-1})_{i,j} = \sum_k (L^{-1} B)_{i,k} L_{k,j}^{-1} = (L^{-1} B)_{i,j} L_{j,j}^{-1} = L_{i,i}^{-1} L_{j,j}^{-1} B_{i,j} \quad (3-32)$$

therefore H is still a symmetric and tridiagonal matrix. By now, near the interface, the Schrödinger equations can be transformed to:

$$-\frac{1}{m_L^* d_L^2} \phi_j(z_{\eta-2}) + \left[\frac{1}{m_L^* d_L^2} \left(2 - \frac{1}{1 + \alpha_{LR}} \right) + V(z_{\eta-1}) \right] \phi_j(z_{\eta-1}) - \quad (3-33)$$

$$\frac{1}{m_L^* d_L^2} \sqrt{\frac{d_L}{d_R}} \frac{\alpha_{LR}}{1 + \alpha_{LR}} \phi_j(z_{\eta+1}) = E_j \phi_j(z_{\eta-1})$$

$$-\frac{1}{m_L^* d_L^2} \sqrt{\frac{d_L}{d_R}} \frac{\alpha_{LR}}{1 + \alpha_{LR}} \phi_j(z_{\eta-1}) + \left[\frac{1}{m_R^* d_R^2} \left(2 - \frac{1}{1 + \alpha_{LR}} \right) + \quad (3-34)$$

$$V(z_{\eta+1}) \right] \phi_j(z_{\eta+1}) - \frac{1}{m_R^* d_R^2} \phi_j(z_{\eta+2}) = E_j \phi_j(z_{\eta+1})$$

$$(3-35)$$

$$\phi_j(z_\eta) = [\phi_j(z_{\eta-1}) + \alpha_{LR} \cdot \phi_j(z_{\eta+1})] / (1 + \alpha_{LR})$$

For other nodes, the Schrödinger equations are the same as equation (1). Finally, the carrier wavefunction ψ can be obtained by

$$\Psi = L^{-1} \varphi \quad (3-36)$$

In the above Schrödinger equations, $V(x) = V_b(z) + V_H(z) + V_{ex}(z)$.

$V_b(z)$ is the band profile of a one-dimensional structure, $V_{ex}(z)$ is the local exchange-correlation energy, and $V_H(z)$ is the Hartree potential, which is obtained by solving the one-dimensional Poisson's equation. In fact, there are three sets of Schrödinger equations representing electrons (e), heavy holes (hh), and light holes (lh) respectively. For each kind of carriers, the corresponding band profile $V_b(z)$ should be used.

3.3.2 Formulation for Poisson's equation

Poisson equation can be expressed as:

$$\kappa_i [V_H(z_{i-1}) - 2V_H(z_i) + V_H(z_{i+1}))] / d_i^2 = 8\pi [N_D(z_i) - N_A(z_i) - n(z_i) + p(z_i)] \quad (3-37)$$

for $z_i \neq z_\eta$, where κ is the dielectric constant;

And at the interface, Poisson equation can be expressed as:

$$\begin{aligned} \frac{2\kappa_L}{d_L(d_R + d_L)} V_H(z_{\eta-1}) - \left[\frac{2\kappa_L}{d_L(d_R + d_L)} + \frac{2\kappa_R}{d_R(d_R + d_L)} \right] V_H(z_\eta) + \\ \frac{2\kappa_R}{d_R(d_R + d_L)} V_H(z_{\eta+1}) = 8\pi [N_D(z_\eta) - N_A(z_\eta) - n(z_\eta) + p(z_\eta)] \end{aligned} \quad (3-38)$$

where V_H is the Hartree potential, and N_D , N_A are the dopant and acceptor density.

If the boundary condition is known, the Thomas Algorithm can be used to solve those discretized Poisson equations. The details will be introduced in Appendix B.

3.4 Self-consistent calculation procedure:

The self-consistent results were obtained by solving the above Schrödinger and Poisson equations simultaneously. The approach is described as follows:

1. We first set up the mesh with variable sizes and discretize the different equations to numerically solve the Schrödinger equations and Poisson's equation.
2. Define the initial band profiles V_{prof}
3. Compute the Schrödinger equation matrix H for electrons, heavy holes, and light holes, respectively.
4. Diagonalize H to get the eigenvalues E (energy levels) and eigenvectors ψ (wavefunctions) for electrons, heavy holes, and light holes.
5. Use the electrical neutrality condition to obtain the Fermi level E_F .

6. Calculate the carrier concentration for each node.

7. Solve Poisson equation to get V_H^{new} .

8. Let $V = V_{prof} + (1-\lambda) V_H^{old} + \lambda V_H^{new} + V_{ex}$ where λ is the iteration coefficient ($0 < \lambda < 1$).

9. Iterate the steps from (3) to (8) until convergence (E_F becomes stationary: $\|\Delta E_F\| \leq \delta$).

4- SELF-CONSISTENT ANALYSIS ON THE CARRIER TRANSPORT OF TYPE-II INTERBAND CASCADE LASERS

In the chapter 3, the mathematical part of our self-consistent model was introduced. This chapter will describe the physical part of our self-consistent model and show how the self-consistent calculation is applied on the type-II interband cascade lasers. At the same time, some self-consistent results are given, including the band profile, the distribution of the carrier density, the energy level alignment near the threshold, and the carrier transport channel. Moreover, the influence of temperature on carrier transport in type-II ICL structure is discussed and an optimized structure is proposed to improve the carrier transport at higher temperature (300K).

In this chapter, one basic structure of the type-II interband cascade laser (#ICL 2200) is used for our simulation. First of all, the structure of the simulated type-II ICL device and its material parameter are introduced in section 4.1 & 4.2.

4.1 The structure parameter of the calculated type-II ICL basic structure

In this chapter, we calculate 3 periods of active and injection regions, which were sandwiched by two 200nm thick and 10eV high potential barriers to satisfy the boundary conditions of the quasi-bound wavefunctions. The structure parameters of the layers in each period are illustrated in Table 4-1.

Table 4-1. The structure parameters of the layers in each period of the calculated type-II interband cascade laser (#ICL 2200)

	Layer Role	Layer name	Thickness	Doping
Active region	<i>electron</i> well	InAs	25 Å	undoped
	<i>hole</i> well	Ga _{0.7} In _{0.3} Sb	34 Å	undoped
	barrier	AlSb	15 Å	undoped
	<i>hole</i> well	GaSb	53 Å	undoped
Injection region	barrier	AlSb	12 Å	undoped
	1 st <i>electron</i> well	InAs	90 Å	undoped
	barrier	AlSb	12 Å	undoped
	2 nd <i>electron</i> well	n-InAs	73 Å	Si: $6 \times 10^{17} \text{cm}^{-3}$

Injection region	barrier	$\text{Al}_{0.7}\text{In}_{0.3}\text{Sb}$	18 Å	undoped
	3 rd electron well	n-InAs	51 Å	Si: $6 \times 10^{17} \text{cm}^{-3}$
	barrier	AlSb	18 Å	undoped
	4 th electron well	n-InAs	43 Å	Si: $6 \times 10^{17} \text{cm}^{-3}$
	barrier	AlSb	19 Å	undoped
	5 th electron well	n-InAs	37 Å	Si: $6 \times 10^{17} \text{cm}^{-3}$
	barrier	$\text{Al}_{0.7}\text{In}_{0.3}\text{Sb}$	20 Å	undoped
	6 th electron well	n-InAs	34 Å	Si: $6 \times 10^{17} \text{cm}^{-3}$
	barrier	AlSb	21 Å	undoped
	7 th electron well	n-InAs	31 Å	Si: $6 \times 10^{17} \text{cm}^{-3}$
	barrier	AlSb	22 Å	undoped
	8 th electron well	n-InAs	28 Å	Si: $6 \times 10^{17} \text{cm}^{-3}$
	barrier	AlSb	23 Å	undoped

The radiative emission occurs between the ground electron state of InAs and the ground heavy hole state of InGaSb in the active region. The injection region comprises of eight InAs wells (electron wells). The growth direction is from bottom to top. All n-InAs layers were Si doped to about $6 \times 10^{17} \text{cm}^{-3}$. The total thickness of one period of active/injection region is 679 Å. The overall structure is well strain-balanced with an overall average lattice constant $\langle a \rangle$ of 6.095 Å, corresponding to a small lattice mismatch (defined as $(\langle a \rangle - a_{\text{substrate}}) / a_{\text{substrate}}$) of 0.0014% to GaSb substrate.

4.2 The material parameters of the calculated type-II interband cascade lasers

The material parameters of the layers grown in the type-II interband cascade laser (#ICL 2200) are shown in Table 4-2 at 80K and Table 4-3 at 300K.

Table 4-2 The material parameters of the calculated type-II interband cascade lasers at 80K

	GaSb	$\text{Ga}_{0.7}\text{In}_{0.3}\text{Sb}$	InAs	AlSb	$\text{Al}_{0.7}\text{In}_{0.3}\text{Sb}$
m_e^*	0.04148 m_0	0.03019 m_0	0.02449 m_0	0.10201 m_0	0.07233 m_0
$m_{hh,z}^*$	-0.26738 m_0	-0.26611 m_0	-0.34130 m_0	-0.46949 m_0	-0.40759 m_0
$m_{lh,z}^*$	-0.04961 m_0	-0.03907 m_0	-0.02707 m_0	-0.15977 m_0	-0.11612 m_0
E_c (eV)	0.9559	0.8457	0.0	2.0999	1.6208

$E_{v,hh}$ (eV)	0.15790	0.20873	-0.39856	-0.25376	-0.09337
$E_{v,lh}$ (eV)	0.15790	0.08514	-0.34922	-0.28747	-0.21880
ϵ	15.7	16.03	15.15	12.04	13.47

Table 4-3 The material parameters of the calculated type-II interband cascade lasers at 300K

	GaSb	Ga _{0.7} In _{0.3} Sb	InAs	AlSb
m_e^*	0.03705 m_0	0.02620 m_0	0.02212 m_0	0.09841 m_0
$m_{hh,z}^*$	-0.26738 m_0	-0.26611 m_0	-0.34130 m_0	-0.46949 m_0
$m_{lh,z}^*$	-0.04354 m_0	-0.03317 m_0	-0.02412 m_0	-0.15311 m_0
E_c (eV)	0.89360	0.79910	0.0	2.03860
$E_{v,hh}$ (eV)	0.19320	0.24403	-0.35446	-0.21846
$E_{v,lh}$ (eV)	0.19320	0.12044	-0.30512	-0.25217
ϵ	15.7	16.03	15.15	12.04

m_e^* is the effective mass of electron. $m_{hh,z}^*$ & $m_{lh,z}^*$ are the effective mass of heavy hole and light hole, respectively. m_0 is the mass of free electron. ϵ is the dielectric constant. All the energy band values are relative to the conduction band edge of InAs.

Under a strained structure, the heavy hole valence energy band edge will split with the light hole valence energy band edge even at $k=0$. Table 4-1 and table 4-2 also give both of heavy hole ($E_{v,hh}$) and light hole's valence band ($E_{v,lh}$) edges

4.3 Threshold carrier density

4.3.1 Threshold carrier density and gain clamping

Before introducing the self-consistent modeling on the carrier transport of the type-II ICLs near the threshold operation, the concept of the threshold carrier density must be indicated. This is one of the important starting points of our model.

Lasing in semiconductor diodes can be described by the following coupled differential equations:

$$\frac{dN}{dt} = \frac{I}{q} - \frac{N}{\tau_c} - GP \quad (4-1)$$

$$\frac{dP}{dt} = GP + R_{sp} - \frac{P}{\tau_p} \quad (4-2)$$

In these equations, N is the number of electrons in the conduction band, I is the injection current, τ_c is the carrier lifetime, G is the net rate of stimulated emission, P is the number of photons emitted into the lasing mode, R_{sp} is the rate of spontaneous emission, and τ_p is the photon lifetime in the cavity. The stimulated emission rate G can be approximated as

$$G = G_N (N - N_0) \quad (4-3)$$

where $G_N = \Gamma v_g \sigma_g / V$, Γ is the mode confinement factor, V is the active volume, v_g is the photon group velocity, σ_g is the differential gain coefficient, and $N_0 = N_T V$ is the transparency carrier number (where $G = 0$) with N_T the threshold carrier density. Finally,

$$\tau_p = \frac{1}{v_g (\alpha_{\text{mirrors}} + \alpha_{\text{cavity}})} \quad (4-4)$$

is the photon lifetime in the cavity arising from absorption within the cavity and transmission through the mirrors. The loss due to the mirrors, with intensity reflectance coefficients R_1 and R_2 , is given by

$$\alpha_{\text{mirrors}} = -\frac{1}{2L} \ln(R_1 R_2). \quad (4-5)$$

At steady state, we can find the conditions for lasing and the output power. Setting the time derivatives to zero, we get

$$0 = GP + R_{sp} - \frac{P}{\tau_p} = G_N (N - N_0) P + R_{sp} - \frac{P}{\tau_p} \quad (4-6)$$

$$0 = \frac{I}{q} - \frac{N}{\tau_c} - GP = \frac{I}{q} - \frac{N}{\tau_c} - G_N (N - N_0) P. \quad (4-7)$$

Using the first equation, the carrier number at steady-state can be written

$$\begin{aligned} N &= N_0 + \frac{(P/\tau_p - R_{sp})}{G_N P} \quad \text{ignore } R_{sp} \\ &= N_0 + \frac{1}{G_N \tau_p} \\ &\equiv N_{th}. \end{aligned} \quad (4-8)$$

which means that the number of carriers is clamped such that gain equals loss. We can see this more clearly by considering the rate of spontaneous emission at steady-state,

$$G = G_N (N_{th} - N_0) = \Gamma v_g g, \quad (4-9)$$

where g is the gain.

$$\begin{aligned} g &= \frac{G_N (1/G_N \tau_p)}{\Gamma v_g} = \frac{1}{\tau_p \Gamma v_g} \\ &= \frac{\alpha_{\text{mirror}} + \alpha_{\text{cavity}}}{\Gamma} = \text{loss}. \end{aligned}$$

Figure 4-1 gives a schematic relationship of the carrier density (N), the gain (g) and the injection current (I). A good demonstration of the threshold carrier density and the gain clamping is also given in Figure 4.2 (a)(b).

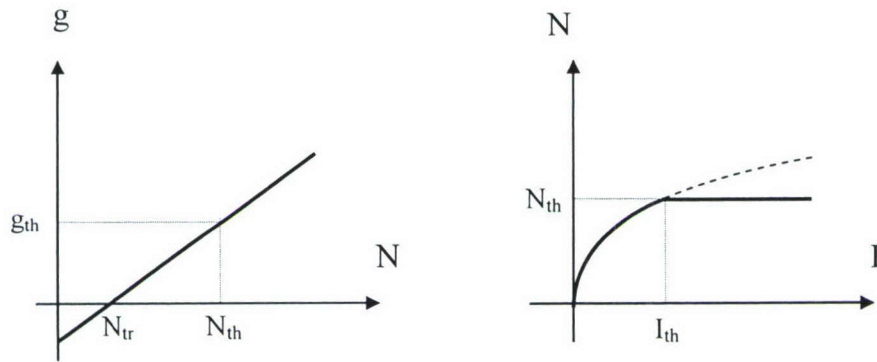


Figure 4-1 Schematic relationship of the carrier density (N), the gain (g) and the injection current (I)

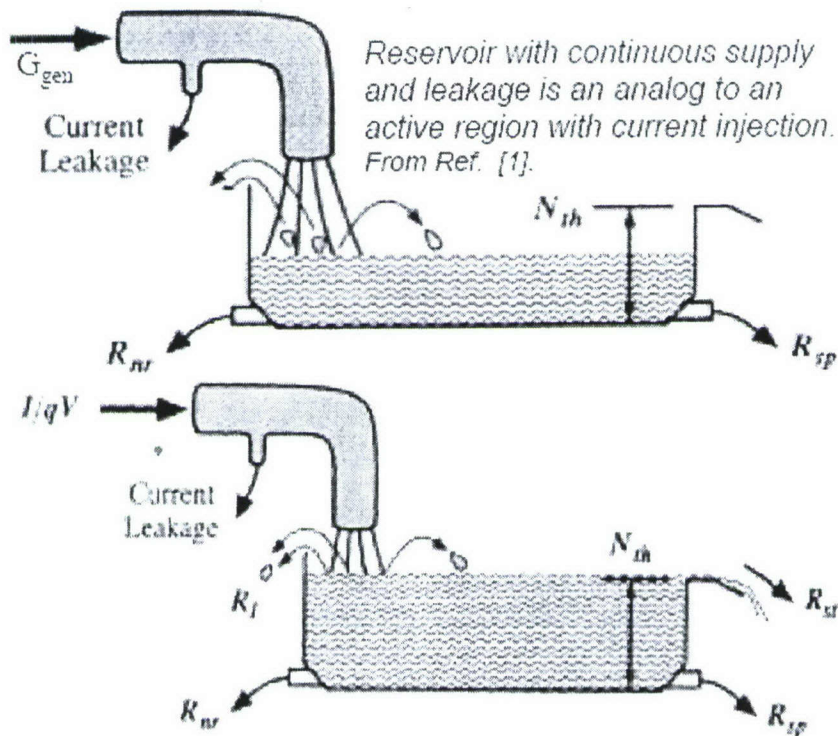


Figure 4-2 The schematics of the carrier density clamping: (a) below the threshold; (b) beyond the threshold

As long as the laser device remains below the lasing threshold, the carrier density increases with the injection rate if the injection rate is bigger than the sum of the leakage rate, the nonradiative recombination rate and the spontaneous emission rate. After the carrier density reaches the transparency carrier density, the stimulated emission occurs and the gain is not equal to zero any more. The gain increases as the increase the carrier density. When the gain exceeds the total losses, photon density increases exponentially so that the carrier density drops abruptly and the gain reduces back to the total loss. As a result, the gain is clamped to the saturated value to balance the total losses. And the carrier density is also still clamped to the threshold carrier density even though the injection rate (the injection current) increases beyond the threshold.

4.3.2 The threshold carrier density of #ICL 2200

The threshold carrier density of our calculated type-II $900\mu\text{m} \times 200\mu\text{m}$ gain-guided IC laser device was estimated as about $3.3 \times 10^{11} \text{cm}^{-2}$ and $1.3 \times 10^{12} \text{cm}^{-2}$ at $T=80\text{K}$ and $T=300\text{K}$, respectively.

4.4 Treatment of Fermi level E_F

In fact, the treatment of the fermi level E_F is critical to simulate the carrier distribution under an external bias in semiconductor devices. Equations (2-11, 2-12, 2-13) gave the electrical neutral condition which had to be satisfied in the whole type-II ICL structure. As described in these equations, the carrier population is strongly dependant on the Fermi level E_F .

In the real device's lasing operation, any bottlenecks during the transportation would result in the carrier accumulation. The accumulated carriers would produce the built-in electrical field and self-adjust the Fermi level & the carrier distribution until the condition of current continuity was satisfied.

It's well known that the current density would increase significantly after the threshold. Then all of the potential transport bottlenecks would be resolved through the carrier distribution and the built-in electrical field. In our calculation model, that could be realized by applying different Fermi level drops at those interfaces where the potential bottlenecks might occur, so that good carrier transports would be finally achieved and the current continuity condition could be satisfied in the whole structure as the increase of the external bias up to the threshold voltage.

The potential current bottlenecks in the carrier transport might occur at the following several places: (a) the interband transition at the interface of InAs/InGaSb, (b) the phonon-assisted resonant tunneling between InGaSb and GaSb wells, (c) the interband tunneling between light-hole state and the miniband of the injection region at the interface of GaSb and the InAs/Al(In)Sb injection regions, (d) the resonant tunnelling from the miniband to the electron ground quasi-bound state of InAs at the active region, (e) and some small Fermi level drops inside of the injection regions due to the imperfect design of the miniband.

Under the threshold bias, the energy levels in the InAs wells of the injection region line up to form a miniband, so we assume that a carrier transport channel is built up near the threshold and the fermi level drops among the InAs wells of the injection region can be ignored. As a result, an equivalent flat fermi level is assumed in the injection region during our calculation, then we will ignore the bottlenecks (d)(e) in the following. Next, we will discuss three fermi level drops

($\Delta E_{F,\text{InAs/InGaSb}}$, $\Delta E_{F,\text{InGaSb/GaSb}}$, $\Delta E_{F,\text{InGaSb-injection region}}$) for the bottlenecks (a),(b),(c), respectively, in detail.

(1) In order to obtain the population inversion, the most prominent bottleneck must exist at the interface of InAs/InGaSb in the active region. So most part of Fermi level drop per period would be distributed at the interface of InAs/InGaSb. Upon the experimentally measured data of this simulated laser device, the threshold carrier density was estimated as $3.3 \times 10^{11} \text{ cm}^{-2}$ [4.1][4.2], which should be clamped even after the lasing. In our simulation, it's found that this carrier density at InAs of active regions was mostly dependent on the difference of Fermi levels ($\Delta E_{F,\text{InAs/InGaSb}}$) beside of the interface of InAs/InGaSb. Thus, this $\Delta E_{F,\text{InAs/InGaSb}}$ would be fixed at 0.39V to achieve the threshold carrier density ($3.3 \times 10^{11} \text{ cm}^{-2}$) at the active region, and $\Delta E_{F,\text{InGaSb/GaSb}}$ & $\Delta E_{F,\text{InGaSb-injection region}}$ would be set as variables to satisfy the following conditions.

(2) Because the heavy-hole energy level of GaSb shouldn't be designed to align well with that of InGaSb in order to obtain a bigger coupling between e(InAs)&hh(InGaSb) states, the fast phonon-assisted resonant tunneling was expected to reduce the lifetime of electrons on the hh state of InGaSb during the carrier transport between InGaSb & GaSb wells so that the population inversion could be achieved. The AlSb-like LO phonon regarded as the main interface LO-phonon mode was about 41meV. So $\Delta E_{F,\text{InGaSb/GaSb}}$ would be tuned in our simulation to satisfy the energy separation of 41meV between the ground hh states of InGaSb (HH1) and GaSb (HH2). In fact, this condition can be easily understood from the standpoint of carrier distribution and the current continuity. If $\Delta E_{F,\text{InGaSb/GaSb}}$ is smaller than the interface LO-phonon, then the fast phonon-assisted resonant tunneling won't happen so that the carriers (electrons) can't be expelled from HH1 to HH2 fast enough to compensate the carrier (electrons) loss in GaSb well due to the interband tunneling between GaSb and the injection region. As a result, the heavy hole density on HH1 will decrease and the hole density on HH2 will increase under an injection current. Then $\Delta E_{F,\text{InGaSb/GaSb}}$ will become bigger until the fast phonon-assisted resonant tunneling occurs.

(3) As described in chapter 2, due to the weak coupling of heavy hole and electron states, the interband resonant tunnelling process between the ground light hole state LH1 of GaSb well and the miniband of the injection region would be dominated at the interface of GaSb well and the injection region. Thus, $\Delta E_{F,\text{InGaSb-injection region}}$ must be tuned to satisfy the condition that the ground light hole state LH1 should be above both of the bottom of the miniband and the ground electron state E_e of the InAs well at the active region in the next period. Otherwise, the carriers will face a wide barrier in the carrier transport. We also can understand this point similarly as the above. If LH1 is below the bottle of the miniband or the ground electron state of the next active region, then the carriers (electrons) will be blocked by the wide barrier and the interband resonant tunneling won't happen. As a result, the hole density on LH1 and HH2 will increase and electron density on the miniband will decrease under an injection current. Then, $\Delta E_{F,\text{InGaSb-injection region}}$ will become big until LH1 goes above the bottle of the miniband and the ground electron state of the next active region.

4.5 The self-consistent calculation results

A nonuniform mesh with 1084 nodes was used for the type-II ICL structure. Then four 1017×1017 matrix equations (three for Schrödinger equations, and one for Poisson equations)

were solved repeatedly until the results converged to certain accuracy. In the calculation, we had to include the first 50 eigenvalues (energy levels) and eigenvectors (wavefunctions) for electrons and the first 120 eigenvalues and eigenvectors for either of heavy holes and light holes. Because a large amount of nodes were adopted and total 290 eigenvalues (energy levels of e, hh, and lh) and 290 eigenvectors (the wavefunctions of e, hh, and lh) need to be solved at each step, we have to use a very small iteration coefficient λ (<0.05) to keep the calculation converging and stable. Due to the small λ , we set the tolerance of $\Delta E_F < 10^{-10}$ for convergence. The typical computation time for convergence is about 5 hours.

Figure 4-3 gave the self-consistent result when $\Delta E_{F, \text{InAs-InGaSb}} = 0.39\text{eV}$, $\Delta E_{F, \text{InGaSb-GaSb}} = 20\text{meV}$, $\Delta E_{F, \text{GaSb-injection region}} = 30\text{meV}$. From the energy level alignment shown in Figure.4-3, we can see a good alignment between the ground light hole state E_{lh} of GaSb and the ground electron state E_c of InAs well at the next active region. At the same time, we got the energy

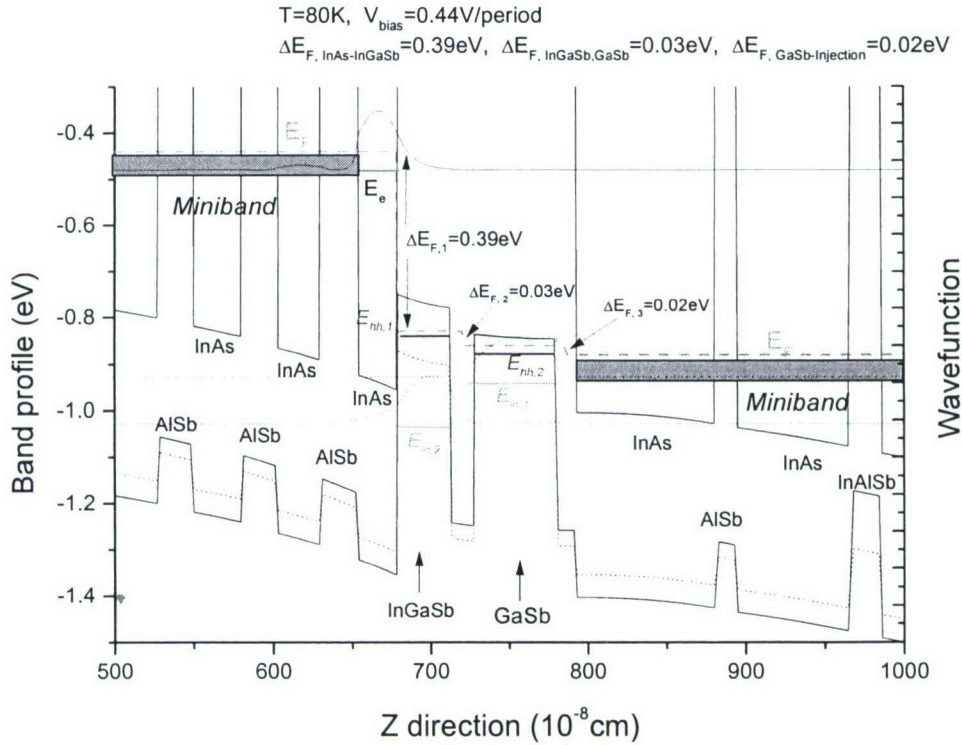


Figure 4-3. Energy levels alignment under 0.44V/period with $\Delta E_{F, \text{InAs/InGaSb}} = 0.39\text{eV}$, $\Delta E_{F, \text{InGaSb-GaSb}} = 20\text{meV}$, $\Delta E_{F, \text{GaSb-injection region}} = 30\text{meV}$ at 80K

separation ΔE_{hh-hh} (between the heavy hole states of InGaSb and GaSb) equal to 42meV. Then total bias = 0.44V/period. That would be the minimum bias required to turn on the fast carrier transport channel. In fact, in order to realize the lasing operation, more $\Delta E_{F, \text{InGaSb-injection region}}$ and more total bias should be required. The current density would increase as the increase of $\Delta E_{F, \text{InGaSb-injection region}}$, because more carriers could be involved into the tunnelling process.

As shown as Figure 4-4, when ΔE_F , GaSb-injection region increased up to 90meV, the energy separation ΔE_{hh-hh} (between the hh states of InGaSb and GaSb) had been equal to about 41meV even at $\Delta E_F, \text{InGaSb-GaSb} = 0\text{meV}$ (the total bias = 0.48V/period). And, at the same time, the ground lh state E_{lh} of GaSb well is a little bit below the top of miniband and E_e, InAs is close to the bottom the miniband. When ΔE_F , GaSb-injection region $> 90\text{meV}$, ΔE_{hh-hh} would be more than 42meV even when $\Delta E_F, \text{InGaSb-GaSb} = 0$. Then, the fast phonon-assisted resonant tunneling would get weak. Thus, 0.48V/period should be the bias where the maximum fast carrier transport would be achieved.

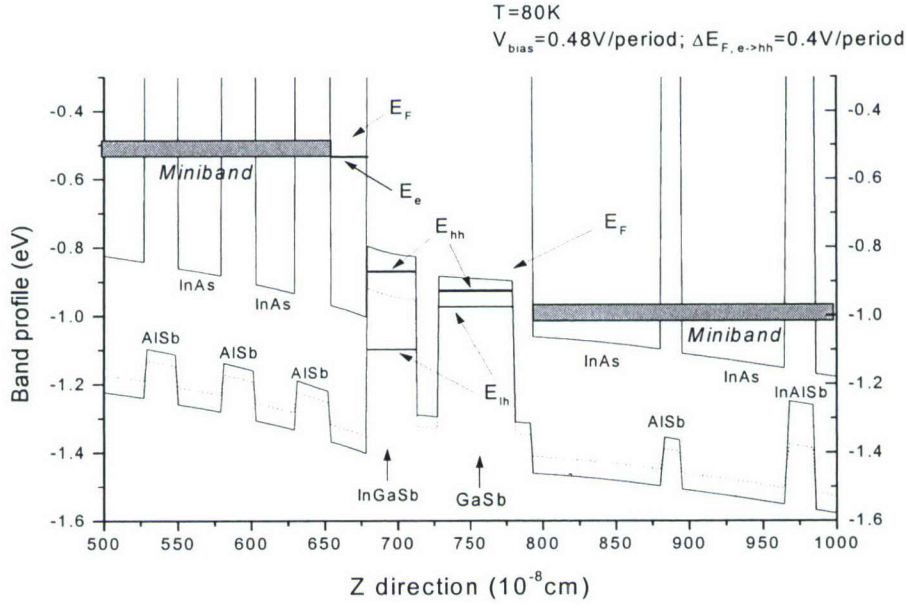


Figure 4-4. Energy levels alignment under 0.48V/period with $\Delta E_{F, \text{InAs/InGaSb}} = 0.4\text{eV}$,

The self-consistent results including the band profile and steady-state carrier distribution are shown in Figure. 4-5. In our calculation, the sign of electron and hole density is defined as + and -, respectively.

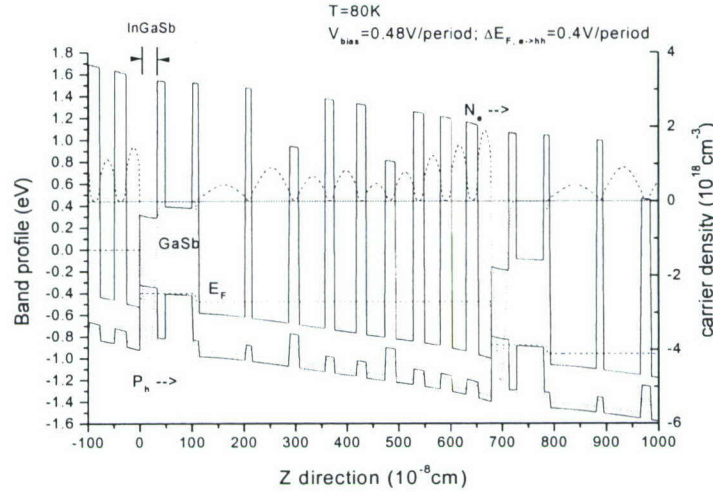


Figure 4-5 self-consistent band profile under 0.48V/period with $\Delta E_{F,InAs/InGaSb}=0.4\text{eV}$, $\Delta E_{F,InGaSb/GaSb}=0\text{eV}$ $\Delta E_{F,GaSb/miniband}=80\text{meV}$ at 80K

4.6 The I-V characteristics of the device of #ICL 2200 at 80K

The current-voltage (I-V) and the L-I characteristics of the device #ICL2200 excited with $1\mu\text{s}$ pulsed current at 1kHz repetition rate (0.1% duty cycle) at 80K are shown in Figure. 4-6. The demarcation point A on the I-V curve corresponds to the situation when the ground energy levels in all injection regions and active regions are lined up to provide a smooth transport path. In this case, the voltage drop is about 11V. The lasing threshold is about 522mA ($290\text{A}/\text{cm}^2$), corresponding to a higher voltage drop (about 14V) across the whole device, as shown as the point B in Figure. 4-6. The total voltage drop across the whole device is the sum of voltage drops across the active regions, the injection regions, the cladding layers, and ohmic contacts, therefore can be expressed as $\Delta V = \Delta V_{\text{active regions}} + \Delta V_{\text{injection regions}} + \Delta V_{\text{cladding}} + \Delta V_{\text{contact}}$

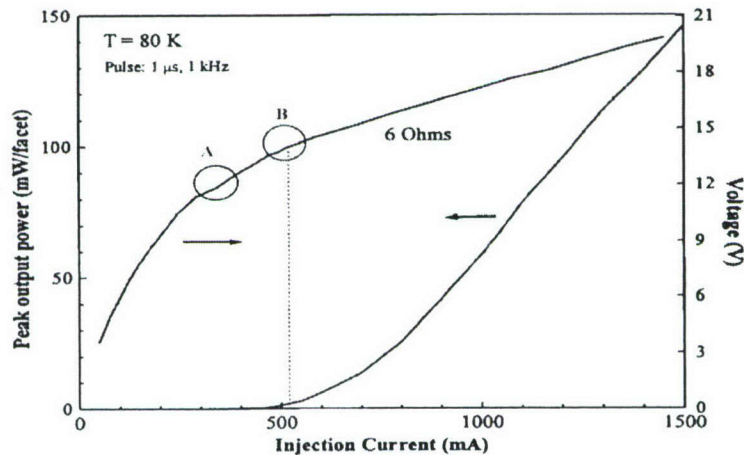


Figure 4-6 Current –Voltage (I-V) characteristics and peak output power .vs. injection current (L-I) curve for the $900\mu\text{m} \times 200\mu\text{m}$ gain-guided IC laser [4.3]

From the I-V characteristics, it's shown that the device's differential resistance (dV/dI) beyond the threshold point is about 6Ω at 80K. Actually, after the threshold, the differential resistance inside of the laser structure should be very small. If the differential resistance of 6Ω is approximately estimated as the fixed external resistance resulting from the cladding layers and the ohmic contacts, then we can get:

At the point A (figure 4-6), after removing the effect of the fixed external resistance, the voltage dropping across the active region and the injection region in each period can be estimated as:

$$(12-0.35 \times 6)/23 = 0.43 \text{ V/period}$$

Thus, the I-V characteristics shows that the smooth transport path start to build up under the bias of 0.43V/period, which matches well with our simulation result (0.44V/period)

And at the threshold point B (figure 4-6), the voltage dropping across the active region and the injection region in each period can be estimated as:

$$(14-0.52 \times 6)/23 = 0.47 \text{ V/period}$$

The bias applied on each period should be still clamped around 0.47V/period even when the total bias is still increased. The excess voltage mostly drops on the external resistance in the cladding layers and the ohmic contacts.

Actually, after the threshold, as the injection current increases, the bias on each period may be increase weakly. This weak increase can be attributed to the small increase of $\Delta E_{F, \text{InGaSb-injection region}}$ so that more current can be admitted to pass through the device. As we simulated, even as the injection current and the total bias increase, the bias on each period shouldn't be more than 0.48V, which gives a good explain for the I-V characteristics.

4.7 Carrier transport at T=300K

As we know, Type-II interband cascade lasers have poor performance as the operation temperature increases. In the following, we will give some discussion about the influence of temperature on the type-II IC lasers performance from the standpoint of carrier transport.

Usually, during designing a laser structure, people always mostly consider the wavelength shift due to the changed band gap and band-offset when the operation temperature increases. In fact, after our self-consistent calculation, we found the carrier transport channel might be destroyed when the operation temperature increases from 80K to near the room temperature.

Figure 4-7 showed the self-consistent result under a bias of 0.53V/period at 300K. And table 4-4 gave the energy separations of some energy levels relative to the ground heavy hole energy level of the active region.

At T=300K, the threshold carrier density of the active region was estimated as about $1.1 \times 10^{12} \text{ cm}^{-2}$ [4.1]. As calculated, the $\Delta E_{F, \text{InAs-InGaSb}}$ has to be fixed as 0.5eV to clamp the carrier density of the active region as this threshold value. And in order to align the ground light hole energy level $E_{lh,l}$ of the active region with the bottom of the miniband of the following injection region, $\Delta E_{F, \text{GaSb-injection region}}$ would be at least 0.03eV. However, it's found that the ground electron energy level $E_{e,l}$ of the next period's active region would be 79meV below the bottom of the miniband.

Then either the resonant tunneling process or phonon-assisted resonant tunneling between the miniband and $E_{e,1}$ of the next active region would be terminated. At the same time, the energy separation $\Delta E_{hh1-hh2}$ between the first two heavy hole energy levels $E_{hh,1}$ and $E_{hh,2}$ would be as big as 45meV, which is already bigger than the interface LO-phonon energy (41meV). Thus, the good carrier transport formed at $T=80K$ would be destroyed as the temperature increases up to near the room temperature (300K) in this laser device.

Why does this happen? The reason is that the higher threshold carrier density ($\sim 1.1 \times 10^{12} \text{cm}^{-2}$) in the active region is required to make this laser device lasing near the room temperature compared with the case of $T=80K$ where the threshold carrier density is about $3.3 \times 10^{11} \text{cm}^{-2}$. The higher carrier density will induce a higher built-in electric field in the InAs well of the active region ($\sim -286 \text{kV/cm}$) and several layers at the right end of the injection region. It's the higher built-in electric field that produces the 78meV energy separation between the miniband and $E_{e,1}$.

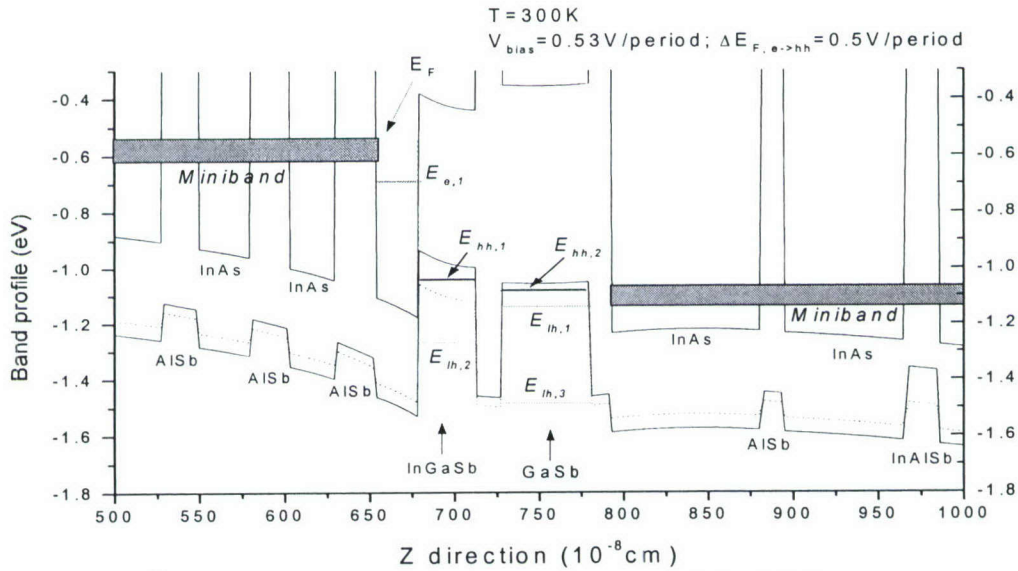


Figure 4-7. The self-consistent result under a bias of 0.53V/period at 300K

Table 4-4. The energy separation relative to the ground heavy hole energy level of the active region for the sample of #2200 (Unit: meV)

Layer	The Active region					Injection region	Next active region
Energy level	e_1	hh_1	hh_2	lh_1	lh_2	<i>miniband</i>	e_1
Self-consistent (0.53V) 300K	350	0	-45	-99	-229	-101 \rightarrow -23	-180
Self-consistent (0.44V) 80K	342	0	-41	-92		-105 \rightarrow -55	-98

Self-consistent (0.48V) 80K	344	0	-42	-93		-136→-90	-136
Linear approximation 80K	346	0	-59	-110		-215→-170	-154

Note: "next active region" represents the active region of the next period.

4.8 Laser structure optimization near the room temperature:

From the alignment of the energy levels in Figure 4-7, we can get some idea on how to optimize this laser device near the room temperature. Obviously, lowering the miniband relatively to $E_{e,1}$ (the ground electron level of the active region) will improve the carrier transport. On one hand, a lower miniband can reduce the big energy separation between the miniband and the ground electron energy level of the following active region. On the other hand, a lower miniband can require smaller $\Delta E_{F, \text{GaSb-injection region}}$ so that the interband tunneling process between $E_{lh,1}$ and the miniband can be more easily to be realized.

Thus, at the injection regions, the distribution of the InAs wells' width should be redesigned. We can obtain a lower miniband in the injection region by widening the InAs wells of the injection region.

4.8.1 Strain balance

In fact, during the structure optimization of the type-II ICLs, we also have to consider the strain balance firstly.

A normal type-II interband cascade laser structure composes of 20-30 periods, and each period has about 20 layers per each period. As known in figure 4-8, the lattice parameters of InAs, InGaSb and AlSb are different from the lattice parameter of GaSb substrate. Improvements in MBE growth technique make it feasible to grow complex structures. However, growth of uniform and dislocation-free multilayer structures is still a considerable challenge. A little lattice mismatch in each period will induce relaxation after growing several periods. In order to achieve pseudomorphic growth, there is a strain-balance requirement upon the whole structure during the laser structure design.

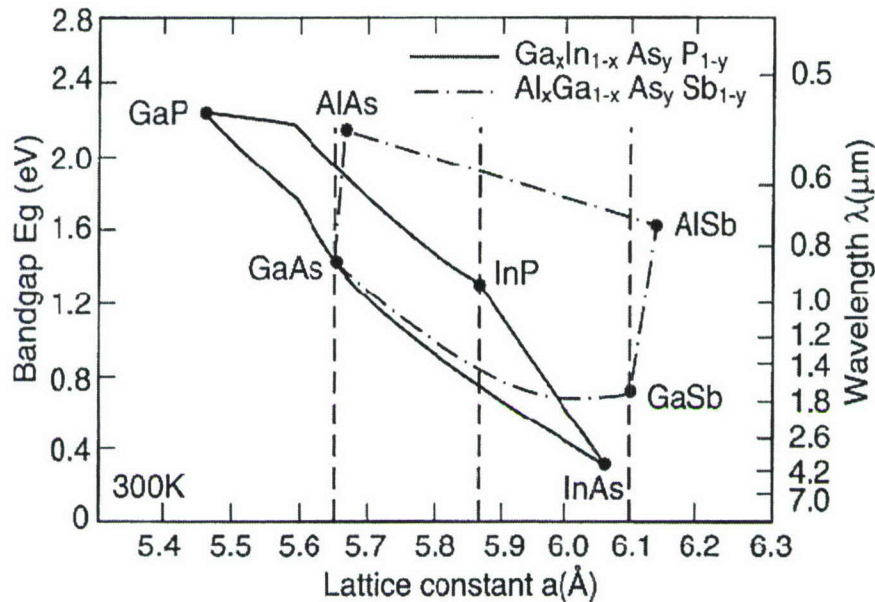


Figure 4-8: Plot showing how the band-gap is related to the lattice parameter for various III-V semiconductors and alloys

A strain balanced structure is one in which the composition of the laser device has been specifically chosen such that strained layers are compensated by the adjacent material, possessing exactly the opposite strain. Then it is possible to grow locally strained layers which are unstrained with respect to the GaSb substrate. The modulated structure may be repeated, without relaxation, until the desired thickness is grown.

Figure 4-9 shows two lattice mismatched materials 1 and 2 grown on a lattice mismatched substrate. The strain-balance condition is met when the average lattice parameter $\langle a \rangle$ across the modulated structure defined by equation (4-11) is equal to the substrate lattice parameter. Similarly, the average strain $\langle f \rangle$ between the MQW stack and neighbouring layers defined by equation (4-12) becomes zero when the structure is strain balanced.

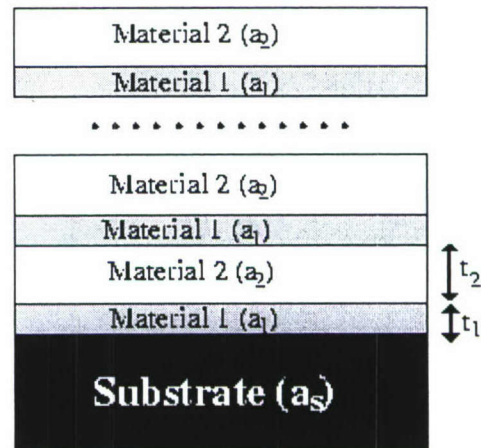


Figure 4-9: A modulated structure composed of materials 1 and 2, grown on an substrate of lattice parameter a_s

(4-11)

$$\langle a \rangle = \frac{\sum_{k=1}^n a_k l_k}{\sum_{k=1}^n l_k} = a_{\text{substrate}}$$

(4-12)

$$\langle f \rangle = \frac{\langle \frac{1}{a} \rangle - \frac{1}{a_{\text{substrate}}}}{a_{\text{substrate}}}$$

Table 4-5 gives the lattice constants of the epilayers grown in the type-II ICLs. In the type-II ICLs, the lattice constant of InAs, AlSb and GaSb are 6.0584, 6.1355 and 6.0959 Å, respectively. The compressive strain due to InAs quantum wells can be compensated by tensile AlSb barriers and the InGaSb wells. With a suitable choice of layer thicknesses and compositions, it is possible to make the average lattice parameter across each period equal to the GaSb substrate. In this way, the thick cascade epitaxy structure will remain unstrained with respect to the GaSb substrate and no relaxation will take place.

Table 4-5 The lattice constants of the epilayers grown in the type-II ICLs. (Unit: Å)

epilayer	GaSb	InAs	AlSb	InSb	In _{0.3} Ga _{0.7} Sb	In _{0.3} Al _{0.7} Sb
Lattice constant	6.0959	6.0584	6.1355	6.497	6.2162	6.244

4.8.2 Laser structure optimization near the room temperature based on the self-consistent results

From the self-consistent band profile at T=300K shown in Figure4-7, it's seen that the electrical fields near the right end of the injection region (like the 6th, 7th, 8th InAs wells) are much bigger than the left end of the injection region (like the 1st, 2nd, 3rd InAs wells). At T=300K, the energy band profiles bend much more than the band profiles did at T=80K. Upon this kind of distribution of the built-in electrical fields, the optimized ICL structure for the room temperature operation is given in table 4-6.

Table 4-6. The structure parameters of the layers in each period of the optimized type-II interband cascade laser for T=300K compared with #ICL 2200

Layer Role	#ICL 2200		Optimized structure for 300K	
	Layer name	Thickness	Layer name	Thickness
<i>electron well</i>	InAs	25 Å	InAs	25 Å
<i>hole well</i>	Ga _{0.7} In _{0.3} Sb	34 Å	Ga _{0.7} In _{0.3} Sb	34 Å
barrier	AlSb	15 Å	AlSb	15 Å
<i>hole well</i>	GaSb	53 Å	GaSb	53 Å
barrier	AlSb	12 Å	AlSb	12 Å
1 st <i>electron well</i>	InAs	90 Å	InAs	103 Å
barrier	AlSb	12 Å	AlSb	15 Å
2 nd <i>electron well</i>	n-InAs	73 Å	n-InAs	110 Å

barrier	$\text{Al}_{0.7}\text{In}_{0.3}\text{Sb}$	18 Å	$\text{Al}_{0.7}\text{In}_{0.3}\text{Sb}$	21 Å
3 rd electron well	n-InAs	51 Å	n-InAs	90 Å
barrier	AlSb	18 Å	$\text{Al}_{0.7}\text{In}_{0.3}\text{Sb}$	22 Å
4 th electron well	n-InAs	43 Å	n-InAs	68 Å
barrier	AlSb	19 Å	$\text{Al}_{0.7}\text{In}_{0.3}\text{Sb}$	23 Å
5 th electron well	n-InAs	37 Å	n-InAs	43 Å
barrier	$\text{Al}_{0.7}\text{In}_{0.3}\text{Sb}$	20 Å	AlSb	21 Å
6 th electron well	n-InAs	34 Å	Deleted	Deleted
barrier	AlSb	21 Å	Deleted	Deleted
7 th electron well	n-InAs	31 Å	Deleted	Deleted
barrier	AlSb	22 Å	Deleted	Deleted
8 th electron well	n-InAs	28 Å	Deleted	Deleted
barrier	AlSb	23 Å	Deleted	Deleted

In order to obtain the full strain-balance in every period□ three $\text{In}_{0.3}\text{Al}_{0.7}\text{Sb}$ barrier layers are used in the optimized ICL structure. The average lattice in each period is about 6.0959 Å which is equal to the lattice constant of GaSb substrate, so that it can be applied in the cascade structure.

Figure 4-10 shows the self-consistent band profiles and the alignment of the energy levels for this optimized ICL structure at 300K under a bias of $V_{\text{bias}} = 0.5 \text{ V} / \text{stage}$.

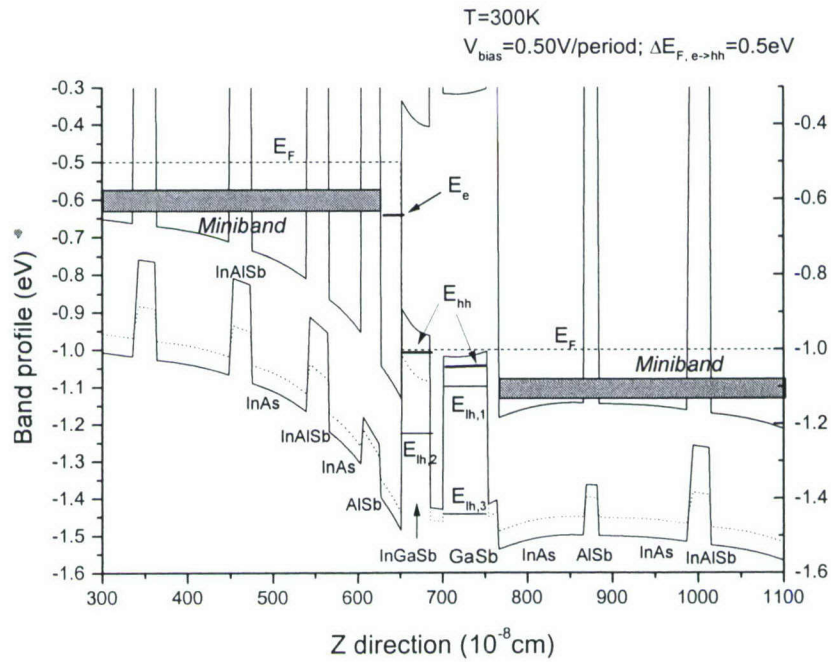


Figure 4-10 The self-consistent band profiles and the alignment of the energy levels for the optimized ICL structure at 300K under a bias of $V_{\text{bias}} = 0.5 \text{ V} / \text{stage}$.

Table 4-7 gives the energy separations of first several electron and hole energy levels relative to the ground heavy hole energy level ($hh1$) of the active region in both cases of the optimized ICL structure and the structure of #ICL 2200 for comparison at 300K. In the self-consistent calculation of the optimized ICL structure, the $\Delta E_{F,e \rightarrow hh}$ at the interface of the InAs and InGaSb is set as 0.5eV to clamp the carrier (electrons) density to $1.1 \times 10^{12} \text{cm}^{-2}$ at the InAs well of the active region. If any other ΔE_F at other interfaces is ignored, then the total bias applied on each period is also 0.5V. From the self-consistent result shown in Figure 4-10 and table 4-7, it's seen that the ground electron energy level $E_{e,1}$ is lift up close to the bottom of the miniband. $E_{e,1}$ is only 9meV below the miniband. That has been small enough to get the ground electron state e_1 coupling with the electron state in the miniband. And the electron states in the injection region line up well to form a 53meV wide miniband providing a smooth transport path between two adjacent active regions. At the same time, the energy separation ΔE_{hh-hh} between the first two heavy hole states $hh1$ & $hh2$ is equal to 42meV which matches well with the energy of the interface AlSb-like LO-phonon so that phonon-assisted resonant tunneling can occur between $hh1$ & $hh2$, and the ground light hole state $lh1$ align well with the miniband. Thus, all of these energy states are lined up to give a smooth path for carrier transport in the optimized ICL structure.

Table 4-7. Self-consistent result: The energy separation relative to the ground heavy hole energy level of the active region at 300K (Unit: meV)

Layer	The Active region					Injection region	Next active region
Energy level	e_1	hh_1	hh_2	lh_1	lh_2	<i>miniband</i>	e_1
#2200 ($V_{\text{bias}} = 0.53\text{V}/\text{stage}$)	350	0	-45	-99	-229	-101 \rightarrow -23	-180
Optimized structure ($V_{\text{bias}} = 0.5 \text{ V}/\text{stage}$)	365	0	-42	-92	-221	-126 \rightarrow -73	-135

Note: "next active region" represents the active region of the next period.

5 – EXPERIMENTAL STUDY OF CARRIER TRANSPORT IN TYPE-II STRUCTURE VIA INAS/ALSB/GASB RESONANT INTERBAND TUNNELING (RIT) DIODES

The ability of recycling carriers from the valence band back to the conduction band through the broken window by resonant or phonon-assisted interband tunneling and scattering is the most

unique feature of type-II IC lasers. Any carrier accumulated at this interface would enhance the inter-valence band and interband absorption and, therefore, the internal loss. As shown in Figure 1-4, the active region in the type-II interband cascade laser based on type-II heterostructures is made up of several resonant interband tunneling structures. Therefore, in my Ph.D research work, the resonant interband tunneling diodes (RITD) are investigated to get a better understand on the carrier transport in the type-II quantum well structures and IC lasers.

5.1 The introduction of resonant tunneling diodes

Figure 5-1 shows several different resonant tunneling structures based on GaSb. Figure 5-1 (d) structure is a kind of normal double-barrier resonant tunneling structure. The electron (or hole) tunneling occurs just inside the conduction (or valence) band. Different from figure 5-1 (d), the former three heterostructures in figure 5-1 (a)(b)(c) show an important feature: the valence band edge of the GaSb layer is higher than the conduction band of InAs contact layers, allowing electrons to tunnel from the conduction-band to the quasi-bound state in the valence-band quantum well. Such this kind of structure is so-called resonant interband tunneling (RIT) structure, where negative differential resistance (NDR) characteristics and high current peak-to-valley ratio (PVR) can be observed (which can be seen in Figure. 5-2).

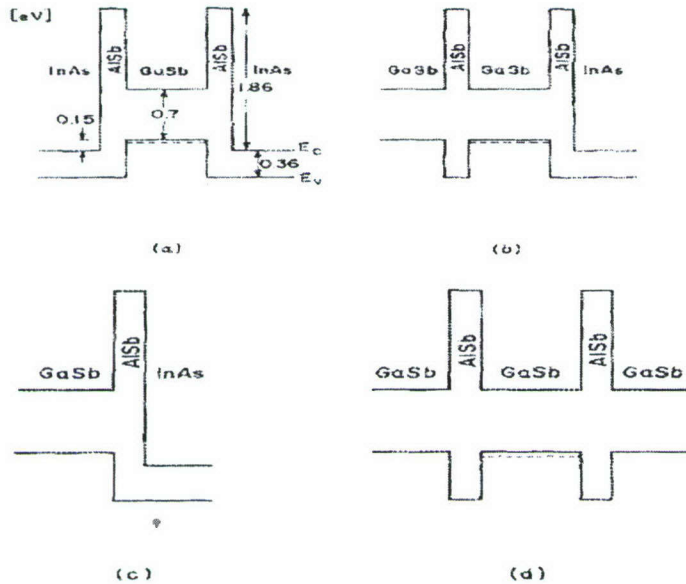


Figure 5-1 The band diagrams of (a) symmetric RIT- resonant interband tunneling (b) DBIT- double barrier interband tunneling (c) SBIT- single barrier interband tunneling (d) DBRT - double barrier resonant tunneling structures based on AlSb/GaSb heterostructures under flat-band conditions [5.1]

virtually eliminating the valley current contributions arising from tunneling. So NDR phenomenon will occur in the I-V characteristics. Figure 5-2 gives out the I-V characteristics of one of our sample (UH 3389) which has a similar structure with figure 5-1 (b), where a positive bias was applied on GaSb substrate and a negative bias was applied on InAs contact layer.

The current density can be given as the following formula [5.1]

$$J = A \int [F_i(E) - F_f(E)] T(E) n_i(E) n_f(E) dE \quad (5.1)$$

where A is a constant, T(E) is the tunneling probability between the initial state and the final state, $F_i(E)$ and $F_f(E)$ are the Fermi-Dirac distribution, and $n_i(E)$ and $n_f(E)$ are the densities of the initial states and final states.

The electron wave function in the InAs couples primarily to the light hole state in the GaSb quantum well. Coupling to the heavy holes is expected to be much weaker since, in a homogeneous bulk crystal, such coupling would be forbidden by symmetry.

In this dissertation, several RTD structures are designed and studied to observe resonant tunneling through the I-V characteristics and investigate the carrier transport in type-II structure.

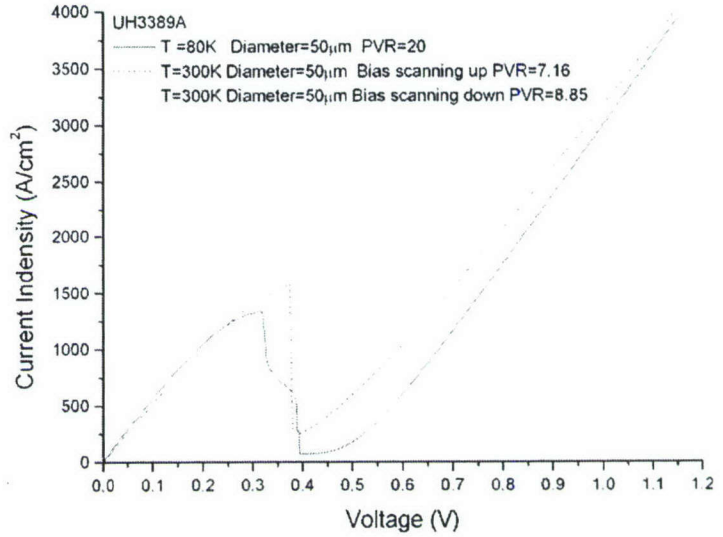


Figure 5-2: The I-V-characteristics of UH3389 at room temperature (T=300K) and low temperature (T=80K).

5.2 The fabrication of the RTDs

The experimental work done included all phases of fabrication and data acquisition except for the epitaxial growth. The Sb-based structures were grown by RIBER MBE 32 system. The details of the fabrication are given below.

The two-terminal InAs/AlSb/GaSb devices were fabricated using standard lithographic technique following the procedure below. All fabrication was done in the facility of Center for Advanced Material at University of Houston.

5.2.1. Mesa etching:

(a) Wafer cleaning: Clean with Acetone, IPA three times, and blow dry with N2 gas

(b) Lithography:

Spin on positive photoresist Shipley 1818 @ 5000rpm for 1 minute

Soft bake @ 110C for 1 minute with hotplates

14 seconds expose;

Post bake @ 120C for 1 minute with hotplates

65 seconds develop in the developer MF319

(c) Etching:

Etchant: Citric (5M):H₃PO₄:H₂O₂ (10:1:1)

Etch for about 30 seconds to have an etching depth about 1.6kÅ with etching rate of about 50 Å/ second

(d) Remove photoresist with Acton, clean the samples and blow dry.

(e) Mesa size:

8 circles/group with diameter - 10, 16, 24, 32, 44, 60, 100, 150 microns

5.2.2. SiO₂ insulating layer growth by PECVD (The total thickness of SiO₂ is about 3kÅ with the growth rate of 450Å/minute.):

- SiH₄: 100 sccm

- NO₂:250 sccm

- 6 minutes @ 200°C under 900 mTorr

- RF power: 15W

5.2.3 Open windows on the SiO₂ layer for metal contacts:

(a) Lithography:

Spin on negative photoresist NR9-1500P @ 3000rpm for 40 seconds

Soft bake @ 150C for 1 minute with hotplates

18 seconds expose;

Post bake @ 70C for 3 minute with hotplates

18 seconds develop in the developer RD6

(b) Hard bake @ 150C for at least 1 minute to dehydrate, and wait 4 minutes to cool down.

(c) Etch with BOE for 40 seconds (the etching rate is about 150~160 Å/second)

(d) Remove photoresist, clean samples and blow dry

5.2.4. E-Beam evaporation for metal contacts:

(a) Lithography for the contact pads:

Spin on negative photoresist NR7-1500PY @ 3000rpm for 40 seconds

Soft bake @ 150C for 1 minute with hotplates

18 seconds exposure;

Post bake @ 120C for 1 minute with hotplates

12 seconds develop in the developer RD6

(b) Oxide etching before the E-Beam evaporation

Etch with HCl (37%) : H₂O (1:10) for 20 seconds to remove native oxides on InAs & GaSb

(c) E-Beam evaporation

Deposit about 300Å Ti, then 3000Å Au for ohmic contact for both n-InAs contact layer and p-GaSb buffer layer.

(d) Lift off in acetone.

5.2.4 Mounting for low temperature measurement

(a) Cleave to individual pieces

(b) Mount on the sample holder with AB glue

(c) Bond gold wire to the contact pads with pure indium.

5.3 Self-consistent band profiles of InAs/AlSb/GaSb RIT Diode

Single well resonant interband tunneling (RIT) diodes based on InAs/AlSb/GaSb heterostructures (as shown in figure 5-5) with different well and barrier width were grown through Riber MBE system. In this section, the band profiles of RIT diodes will be simulated under different operation voltages. Figure 5-6 gives the structure parameter of a sample numbered as UH3416.

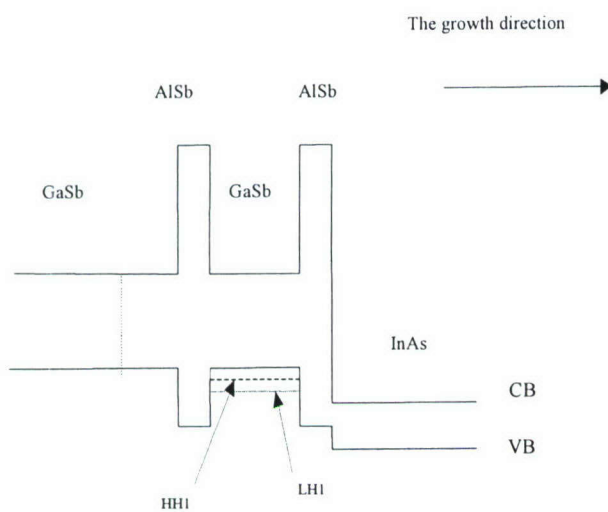


Figure 5-5: The structure of single-well resonant interband tunneling structure InAs/AlSb/GaSb/AlSb/GaSb (under a flat-band condition)

InAs : 197 Å	$n = 1 \times 10^{18} \text{ cm}^{-3}$
InAs: 99 Å	undoped
AlSb: 19 Å	undoped
GaSb: 60 Å	undoped
AlSb: 19 Å	undoped
GaSb: 100 Å	undoped
GaSb: 6096 Å	$p = 1 \times 10^{18} \text{ cm}^{-3}$
p-type	GaSb substrate

Figure 5-6: The structure parameter of the sample of UH3416

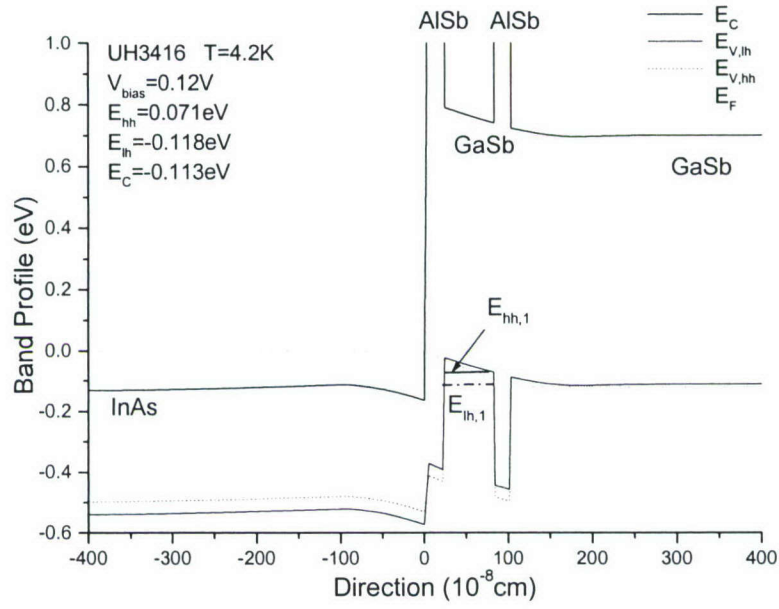


Figure5-7 (a) Self-consistent band profile of UH3416 under $V_{\text{bias}}=0\text{V}$ at $T=4.2\text{K}$

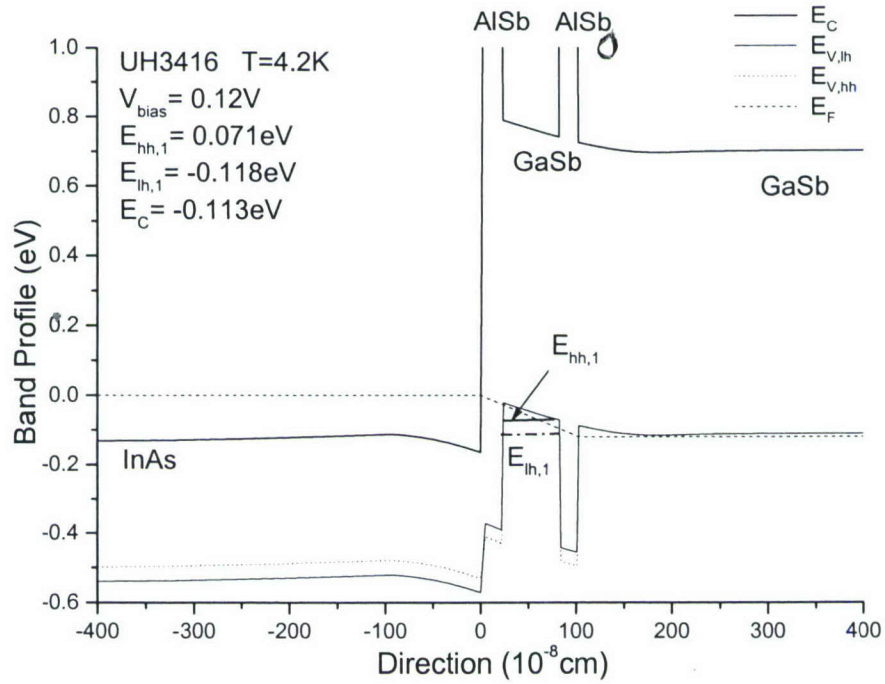


Figure5-7 (b) Self-consistent band profile of UH3416 under $V_{\text{bias}}=0.12\text{V}$ at $T=4.2\text{K}$

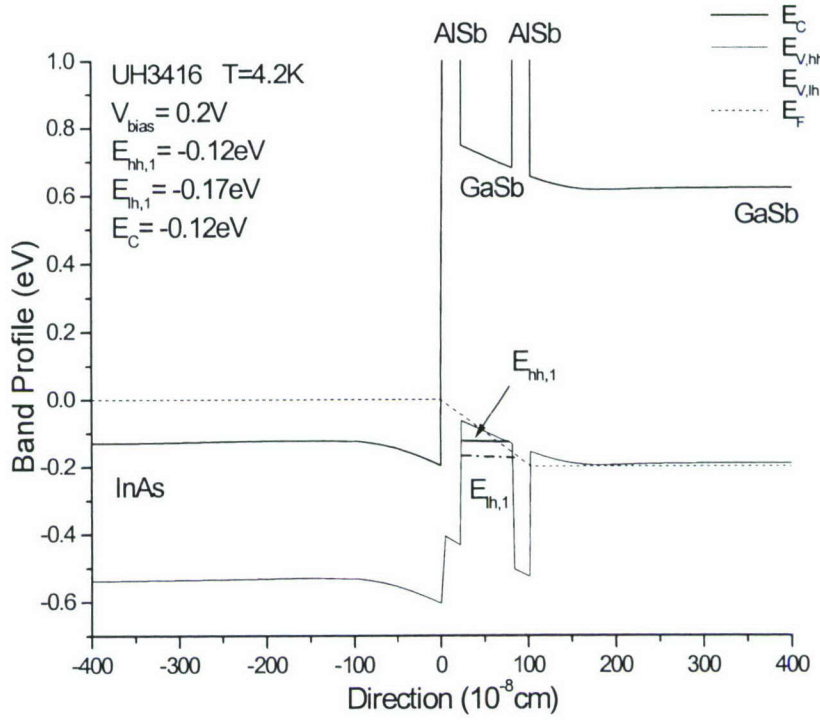


Figure 5-7 (c) Self-consistent band profile of UH3416 under $V_{\text{bias}}=0.2\text{V}$ at $T=4.2\text{K}$

After using the self-consistent method introduced in chapter 2, we give the self-consistent band profiles of UH3416 under external biases of 0V, 0.12V, 0.2V in Figure 5-7 (a) (b) (c), respectively. The thick solid lines are the conduction band edge, the solid lines are the heavy hole valence band edge, the dotted lines are the light hole valence band edge, and the dashed lines are the Fermi level. The thick short lines in the GaSb well represent the ground energy level of heavy hole $E_{\text{hh},1}$, and the dash-dotted short lines represent the ground energy level of light hole $E_{\text{lh},1}$.

When $V_{\text{bias}} = 0\text{V}$, the ground light hole energy level $E_{\text{lh},1}$ in the GaSb well is above the conduction band edge of InAs but below the fermi level (as shown in Figure 5-7a);

When $V_{\text{bias}} = 0.12\text{V}$, $E_{\text{lh},1}$ is aligning well with the conduction band edge of the InAs contact layer (as shown in Figure 5-7b).

After $V_{\text{bias}} > 0.12\text{V}$, the ground light hole state lh_1 in the GaSb well will sink below the conduction band edge of the InAs contact layer. And when $V_{\text{bias}} = 0.2\text{V}$, the ground heavy hole state hh_1 is aligning well with the conduction band edge of the InAs contact layer.

Based on the calculated electron wavefunction distribution, it's noted that no 2D electron state is observed at the InAs triangle well close to the InAs/AlSb interface. As a result, it's regarded that the resonant interband tunneling process only occurs between the 3D electron states of the InAs layer and the 2D ground light hole state of the GaSb well.

5.4 The resonant interband tunneling process

Based on the self-consistent results in Figure 5-7(a)(b)(c), the alignment of the energy levels (in k domain) during the electron tunneling from the conduction band of InAs to the light hole state of the GaSb well under the biases of 0V, 0.12V, 0.2V is drawn in Figure 5-8. The shadow area is the fermi sea which is almost fully occupied by electrons at 4.2K. The electrons tunneling direction is from the 3D electron energy states in the fermi sea (InAs layer) to the 2D ground light hole energy state lh_1 in GaSb well.

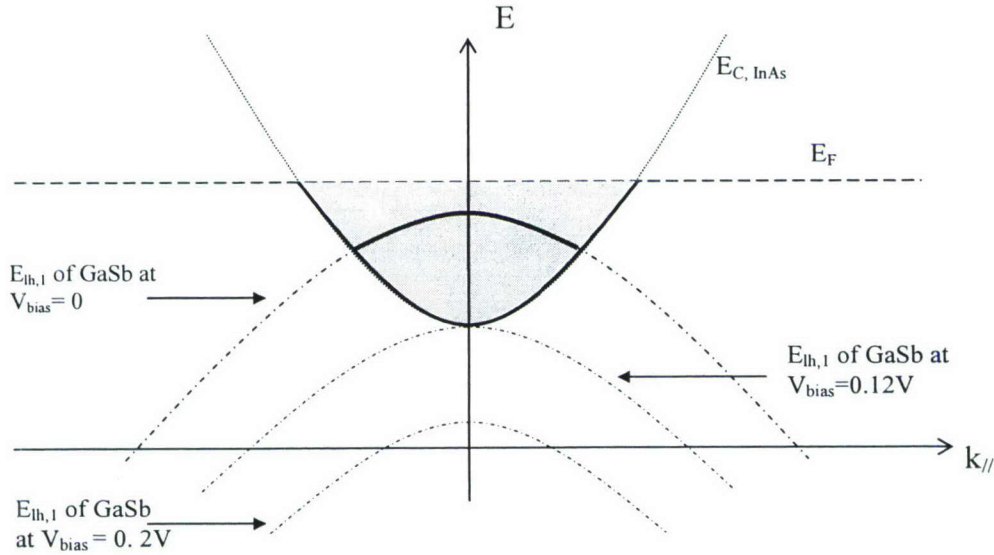


Figure 5-8. The alignment of energy levels during the tunneling from $E_{C, InAs}$ to $lh_{1, GaSb}$ in RIT diodes (UH3416) under the external biases of 0, 0.12V, 0.2V at $T=4.2K$. The shadow area is the fermi sea. The electrons tunneling direction is from the fermi sea to the ground light hole energy state lh_1 .

At the same time, in order to demonstrate the resonant interband tunneling process, the I-V characteristics of the RIT diode based on the sample of UH3416 at $T=4.2K$ is also given in Figure 5-9. The radius of the circle mesa of this RIT device is about $5\mu m$.

Initially, when no external bias is applied ($V_{bias} = 0V$), $E_{lh,1}$ is above the conduction band edge of InAs ($E_{C, InAs}$) and below the fermi level. It's obviously seen that $E_{lh,1}(k_{//})$ is crossing the fermi sea of InAs, as shown in Figure 5-8. Thus, the energy and lateral momentum conservation is easily satisfied between the initial tunneling states (the 3D electron states in the InAs fermi sea) and the final tunneling state (the 2D light hole state lh_1 of the GaSb well). Then, once a bias is applied, the resonant interband tunneling can occur easily between those states, corresponding to the point A of the I-V curve in Figure 5-9. As a result, compared with type-I resonant intraband tunneling diode, no threshold current is required in this type-II resonant interband tunneling diode.

From Figure 5-8, it's seen that, as the bias increases, the intersect part of $E_{lh,1}(k_{//})$ with the fermi sea reduces. This means that the electrons which are ready to be involved into resonant interband tunneling gradually become less on the initial state. But as the increase of the external bias, the fermi level will become more close to $E_{lh,1}$. Then, the light holes on the final states (lh_1) increase exponentially. As a result, the current will increase with the bias, which is corresponding to the point A of the I-V curve in Figure 5-9.

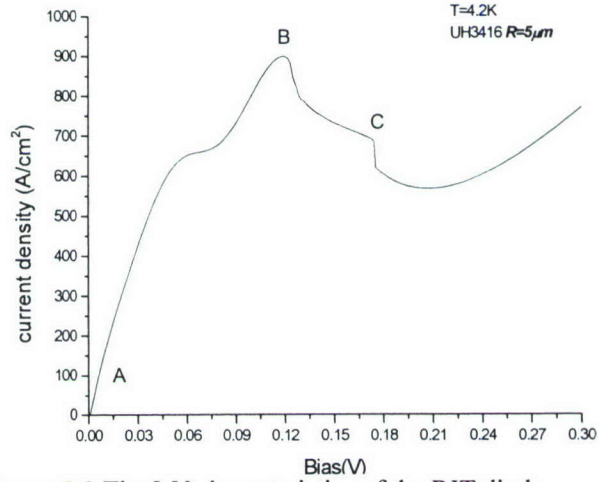


Figure 5-9 The I-V characteristics of the RIT diode based on the sample of UH3416 at $T=4.2K$.

As mentioned in section 5.3, when the bias increases up to more than 0.12V, $E_{lh,1}$ begins to sink below the conduction band edge of the InAs contact layer. Then, as shown in Figure 5.8, $E_{lh,1}(k_{//})$ has no intersection any more after $V_{bias} > 0.12V$. Then, no electrons in the fermi sea of InAs satisfy the condition of the energy and lateral momentum conservation any more so that the resonant interband tunneling process will be forbidden. The transmission coefficient decreases exponentially. As a result, the current decreases abruptly. Upon the I-V curve of the RIT diode (UH3416) in Figure 5-9, a sharp peak can be observed at the point B. The Bias V_{bias} at the peak is measured as 0.119V, which matches very well with our calculated peak voltage value (0.12V).

A “plateau-like” structure (at the point C of I-V curve) is seen following the resonant tunneling peak in Figure 5-9. Such a structure is also often observed in the I-V measurement of both of type-I resonant intraband tunneling diodes and type-II resonant interband tunneling diodes. Some external series inductance, capacitance and resistance always exist either in the contact regions or in the measurement circuit. These external series resistances have two effects on the characteristics of the negative differential conductance (NDC) device: circuit oscillation and current hysteresis. People believe that this “plateau-like” structure is a characteristic feature of current oscillations which average the high resonant and low off-resonant currents.

As seen in figure 5-9, a pronounced shoulder appears before the main resonant peak. Similar phenomenon was observed in resonant interband tunneling diode in previous reported works at $T=4.2K$. It's regarded that this shoulder probably indicates an interband tunneling through a heavy-hole state. The coupling between heavy hole and electron states is weak but not equal to zero at $k_{//} \neq 0$.

Figure 5-10 shows the energy alignment of heavy hole states and electron state at k domain under different bias. In the case of 1, the intersection points of E_{hh} and E_e is above the fermi sea so that no electrons can tunnel to heavy hole states due to the requirement for in-plane momentum ($k_{//}$) conversation. As the increase of bias, the intersection points of E_{hh} and E_e begin to enter the fermi sea (as shown as the case 2 in Figure 5-10). Then resonant tunneling through

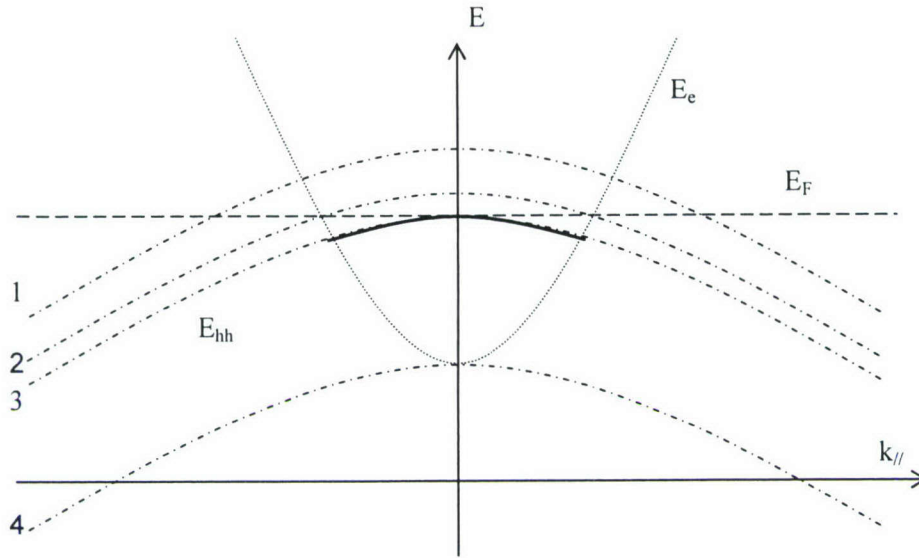


Figure 5-10 The energy alignment of heavy hole states and electron state at k domain under different bias. The dotted line represents the energy of electrons in the conduction band of InAs. The dash-dotted lines represent the energy of heavy hole in the quasi-bound state of GaSb well.

the heavy hole state begins as InAs electron states can transfer to HH state, conserving energy and $k_{||}$. The maximum resonant current through the heavy hole state is obtained at the case 3 where the number of InAs electrons satisfying the conservation of energy and $k_{||}$ reaches maximum. After that, as the increase of the bias, the number of InAs electrons satisfying the conservation of energy and $k_{||}$ reduces. At the same time, the in-plane momentum $k_{||}$ of those electrons also decrease so that the coupling of electron and heavy hole states become weaker. As a result, thereafter, the resonant current through HH decreases and vanishes as the overlap of the InAs electron states and the HH state ceases (as the case 4 in Figure 5-10).

And it's well known that the light-hole states play much more important role in the resonant tunneling than the heavy-hole states do. Thus, experimentally, the maximum resonant current through the HH state appears as a shoulder in the current-voltage curves prior to the main peak bias (as shown in Figure 5-9).

5.5 The influence of the AlSb barrier thickness on the I-V characteristics for resonant interband tunneling diodes

The thickness of AlSb barrier will definitely influence the I-V characteristics. Here two devices (#UH3388 and #UH3389) with different AlSb barrier thickness are fabricated and measured. The structures of #UH3388 and #UH3389 are shown in Figure 5-11 (a)(b). The AlSb barriers' thickness of #UH3388 and #UH3389 are about 19Å and 25 Å, respectively.

Figure 5-12 gives the I-V characteristics of UH3388 and UH3389 at $T=300\text{K}$. And Figure 5-13 give the influence of the barrier thickness on the peak & valley current density and the current peak/valley ratio (PVR). When the AlSb barrier thickness increases from 19Å to 25Å, the current density J_{Peak} and J_{Valley} decrease rapidly from 8551 to 1516 A/cm² and from 1150 to

175A/cm², respectively. That's because the thicker AlSb barrier reduces the coupling between the electron energy states and the light hole energy states at both sides of the AlSb barrier, which is similar to the case of type-I RTDs [5.12]. Thus, in the type-II ICL structure, in order to permit higher current density passing through the laser structure to achieve higher output light power, the AlSb barrier shouldn't be designed too thick.

InAs: 197 Å $n = 1 \times 10^{18} \text{ cm}^{-3}$	InAs: 197 Å $n = 1 \times 10^{18} \text{ cm}^{-3}$
InAs: 99 Å undoped	InAs: 99 Å undoped
AlSb: 25 Å undoped	AlSb: 25 Å undoped
GaSb: 67 Å undoped	GaSb: 67 Å undoped
AlSb: 25 Å undoped	AlSb: 25 Å undoped
GaSb: 100 Å undoped	GaSb: 100 Å undoped
GaSb: 6096 Å $p = 1 \times 10^{18} \text{ cm}^{-3}$	GaSb: 6096 Å $p = 1 \times 10^{18} \text{ cm}^{-3}$
p-type GaSb substrate	p-type GaSb substrate
(b) #3389	(b) #3389

Figure 5-11 (a) The structure parameter of #UH3388; (b) The structure parameter of #UH3389

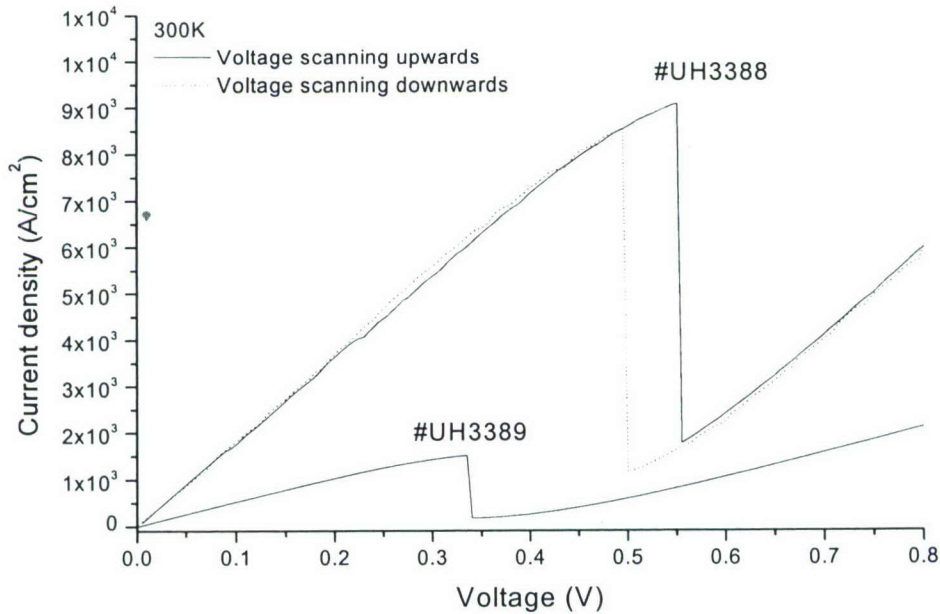


Figure 5-12 The I-V characteristics of UH3388 and UH3389 at T=300K

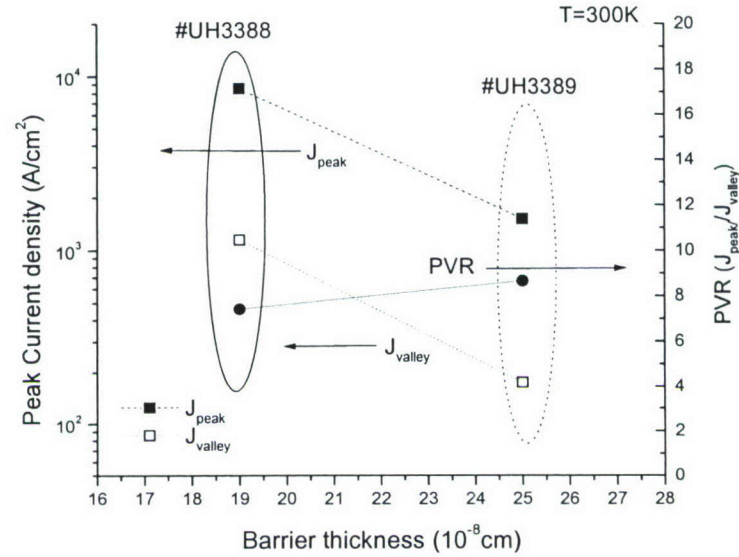


Figure 5-13 The influence of the barrier thickness on J_{Peak} & J_{Valley} and PVR

5.6 Further work

In type-I AlGaAs/GaAs RTD, LO-phonon-assisted resonant tunneling processing between 3D and 2D electron state was observed through the I-V characteristics measured under a magnetic field at low temperature $T=4.2\text{K}$. We have also done some similar research work on our InAs/AlSb/GaSb resonant interband tunneling diode. The phonon-assisted resonant tunneling processing between electron states and light-hole states is being investigated through the I-V characteristics measured under a magnetic field at low temperature $T=4.2\text{K}$. In our further research work, we propose to carry out some theoretical analysis on the measured data.

In addition, some more complicated type-II resonant interband tunneling structure will be studied. The two-hole-wells resonant interband tunneling structure shown in Figure 5-13 is more similar to the

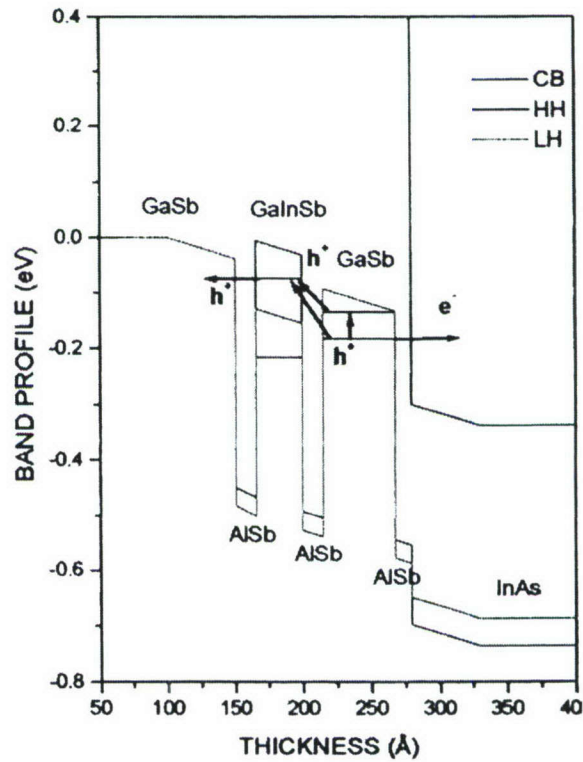


Figure 5-13 Double-well resonant interband tunneling structure

InAs/AlSb/GaSb/AlSb/Ga(In)Sb/AlSb/GaSb

active region of the type-II ICL. Upon this structure, the LO-phonon-assisted tunneling processing between the heavy hole energy states of two Ga(In)Sb wells will be investigated.

Task #4: Silicon Technology Compatible Devices Based on Phonon-Assisted Tunneling:
Project leader: A. Zaslavsky (Brown)

Participants: S. Luryi (phonon assisted tunneling theory), H. Maris (phonon propagation).
Industry Links: Lucent/Agere Systems Bell Laboratories; LETI-CEA (Electronics & Information Technology Laboratory–Atomic Energy Commissariat, France); IBM Yorktown

I. - INTRODUCTION

The principal aim of the research into phonon-assisted tunneling devices pursued by the combined Brown–Stony Brook team with the assistance of industry partners, both in the U.S. and in France, was to integrate the nonlinear current-voltage characteristics provided by interband or intraband (resonant) tunneling into devices that are compatible with the dominant silicon technology. While many tunneling devices were demonstrated over the past two decades in epitaxial heterostructures, usually in III-V semiconductors, their technological implementation has been hindered by their incompatibility with the real-world requirements of VLSI compatibility and room temperature operation. We have, instead, focused on devices that could, in principle, complement standard Si CMOS circuitry and provide new functionality.

Three classes of tunneling based devices, all operating at room temperature and hence involving phonon-assisted processes, were investigated during the course of the project. We began by working on multiemitter interband tunneling heterojunction bipolar transistors (HBTs), originally proposed theoretically by one of the participants (SL) and subsequently fabricated by team in collaboration with Agere Systems. As described in Section 2, these multiemitter Si/SiGe HBTs provided the high current gain available in standard HBTs, but with simplified processing as well as additional logic functionality. Subsequently, encouraged by the ascendance of silicon-on-insulator (SOI) technology, we investigated two classes of SOI-based tunneling transistors: the lateral interband tunneling transistor (LITT) and the vertical tunneling transistor (VTT).

The LITT, described in Section 3, is based on the gate control of interband tunneling in a heavily-doped source-drain *pn* junction. Since there is no inversion channel under the gate, unlike the usual CMOS FET, the LITT has little gate capacitance and is not subject to short-channel effects. This, combined with the fact that the source-drain junction is reverse biased and hence avoids minority carrier injection, makes the LITT very promising as a high-speed amplifier. Further, the LITT is not constrained by the diffusion-driven subthreshold current of a standard FET and hence can, in principle, be turned off more sharply than the ~60 mV/decade of current limit of the transistor. For this reason, it has attracted considerable interest lately in the Si device community, with several groups pursuing various implementations.

Unlike the two preceding devices that used interband tunneling, the VTT, described in Section 4, is based on resonant tunneling from the gate into a thin SOI channel, followed by lateral extraction of the tunneling current via the source and drain. The control over the tunneling

current via the backgate offers the intriguing possibility of negative transconductance. The VTT, initially conceived and demonstrated in III-V heterostructures and demonstrated for the first time in silicon by our team in collaboration with LETI-CEA, is ideally suited to SOI technology provided sufficiently thin and uniform Si channels can be integrated with well-controlled gate tunnel barriers – both are anticipated on the silicon technology roadmap.

The demonstration of tunneling into quantized 2D subbands in a thin SOI silicon channel, opened up an intriguing possibility of intersubband population inversion – and therefore an intersubband long-wavelength optical source – that was recently proposed by two of the team PIs (SL and AZ). Although this device requires much higher tunneling current densities than are presently available, the well-controlled high- κ dielectrics predicted by the silicon technology roadmap could make it a reality, as described in Section 5.

Finally, during the last months of the project, we began a collaboration on epitaxial germanium-on-insulator (GeOI) devices with IBM Yorktown. The eventual aim was to transfer the interband tunneling LITT concept to ultra-thin Ge channels, where the lower bandgap of Ge is expected to result in much higher tunneling currents. Development of GeOI tunneling devices would be particularly useful as the integration of Ge channels into silicon technology is now a major issue in silicon technology. The preliminary results obtained are described in Section 6.

The report concludes with a final Section 7 listing the publications and invited talks by the team members, as well as the graduate students supported with the help of the MURI program.

2. - MULTIEMITTER TUNNELING HBTs WITH ENHANCED LOGIC FUNCTIONALITY.

The essential idea of multiemitter Si/SiGe HBTs originally proposed and demonstrated[1] by some of the team members is to control the injected current in one (or more) emitters by the interband tunneling current in another – reverse-biased – emitter. A schematic cross-section of the device is shown in Figure. 1: two (or more) emitter contacts are fabricated in the *npn* Si/SiGe/Si HBT and then isolated from each other, so a current between any two emitter contacts can only flow via the base. There is no direct contact to the heavily doped *p*-SiGe base. Then, as in Figure. 1, we ground one emitter and apply a positive voltage V_{E2} to the other, as well as a positive collector voltage V_C . The emitter-base junction of the first emitter will be forward-biased and the usual injected electron current I_E will flow to the base-collector junction giving the collector current I_C . As in a standard HBT, a fraction of the injected electron current will recombine in the base, but instead of an ohmic base contact, the hole base current I_B is supplied by phonon-assisted interband tunneling in the second, reverse-biased emitter-base junction – see Figure. 1. The distribution of V_{E2} between the two junctions (i.e. the potential of the floating base) is determined by the current gain β :

$$I_{E1} \sim I_C = \beta I_B \quad (1)$$

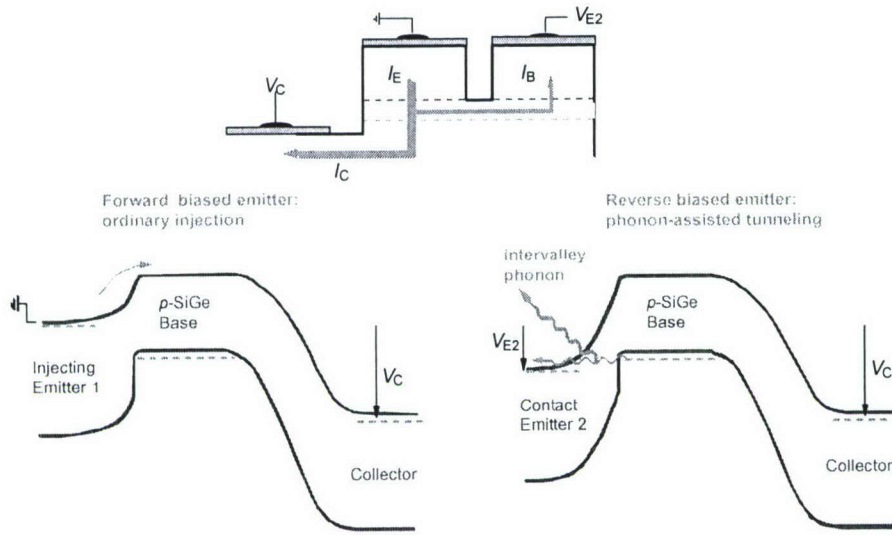


Fig. 1. Schematic layout of the multiemitter *npn* Si/SiGe/Si HBT (a) and corresponding band diagrams of the forward-biased (injecting) and reverse-biased (phonon-assisted tunneling contact) junctions.

The current gain β depends, as in a standard HBT, on the emitter-base doping and the additional valence band barrier due to the Si/SiGe heterojunction. The enhanced logic functionality arises from emitter contact symmetry: the collector current flows provided the emitter contacts are at a different potential, while biasing both emitters either high or low shuts off I_C .

In collaboration with Agere Systems we fabricated optimized *npn* Si/Si_{0.7}Ge_{0.3}/Si MT-HBTs. The best room-temperature transistor characteristics are shown in Figure 2. Figure 2(a) shows the $I_C(I_{E2}, V_C)$ characteristic, with $V_{E1} = 0$ (grounded) and I_{E2} stepped 0–5 μA through the second emitter. The current gain β is ~ 1300 , and the curves are unchanged from the case when $I_B = 0$ –5 μA is supplied through a true base contact instead. Figure 2(b) shows the $I_C(V_{E2}, V_C)$ characteristic of the same device, with $V_{E2} = 0.6$ –1 V. Given the high β , the device turns on as soon as V_{E2} exceeds the forward turn-on voltage of ~ 0.6 V and by the time $V_{E2} = 0.9$ V, I_C reaches 4 mA. Clearly, a power supply of < 1 V would be sufficient for many digital logic applications.[2]

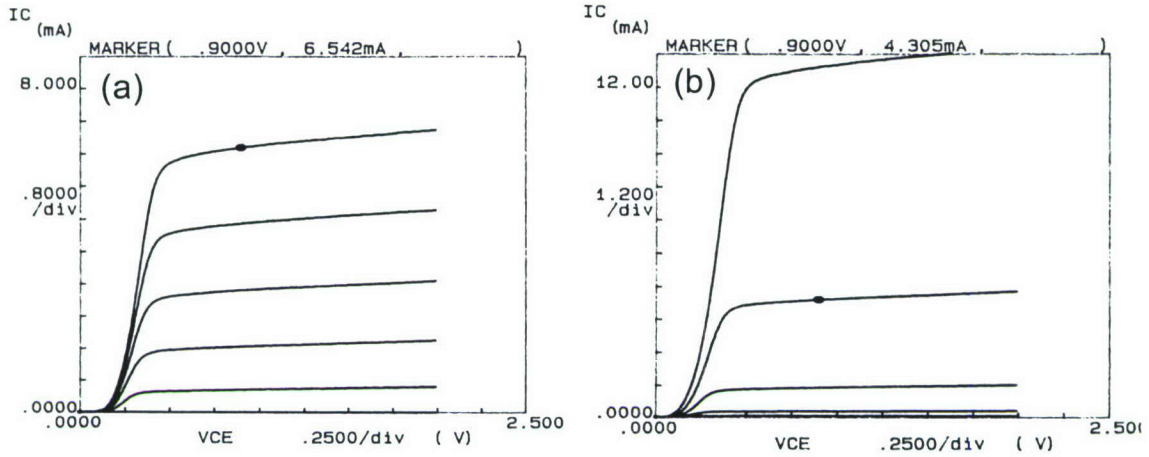


FIG. 2. (a) Room temperature $I_C(I_{E2}, V_{CE})$ characteristics, $I_{E2} = 0$ – 5 A in steps of 1 A. (b) $I_C(V_{E2}, V_{CE})$ characteristics, $V_{E2} = 0.6$ – 1.0 V in steps of 0.1 V.

The logic functionality of our MT-HBTs is illustrated in Figure 3. Figure 3(a) shows a two-emitter device acting as an *xor* gate as a function of the emitter voltages V_{E1} and V_{E2} , with logic levels defined as zero (low) and 0.9 V (high), with the collector kept high at $V_C = 0.9$ V. The collector current is zero when V_{E1} and V_{E2} are both high, and nearly zero (0.14 μ A) when V_{E1} and V_{E2} are both low. When V_{E1} and V_{E2} are at different logic levels, I_C is ~ 4 mA, with the difference attributable to slight process variations. The logic on/off ratio is well over 60 dB at room temperature. Figure 3(b) shows the *ornand* logic function in a three-emitter device: I_C is near zero if all three emitters are either high or low, otherwise I_C is high.

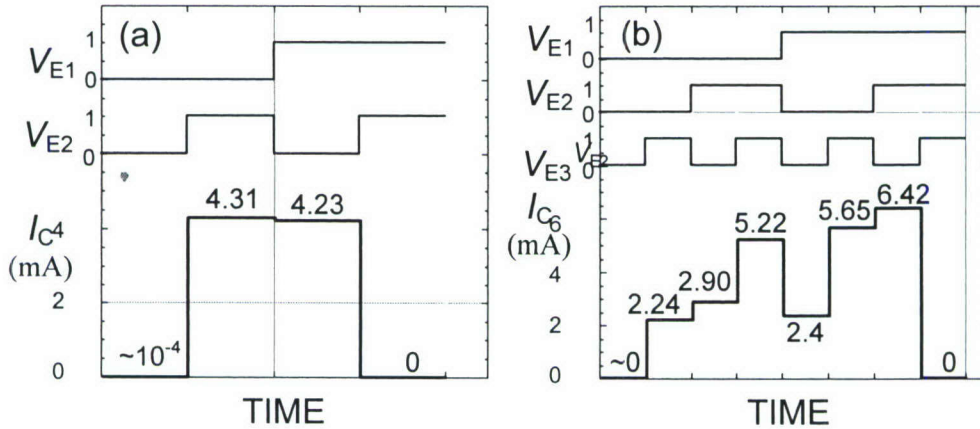


FIGURE 3. (a) Double-emitter *xor* logic and (b) triple-emitter *ornand* logic: in both cases the high and low logic input levels are $V_E = 0.9$ V and 0 , while V_C is at 0.9 V. The on/off ratio is > 60 dB at $T = 300$ K.

We then developed a fabrication sequence[2] for multiemitter SiGe HBTs compatible with a modular SiGe BiCMOS process developed by Agere, with the p -SiGe base and n -Si emitter are regrown by selective epitaxy. Our MT-HBT was to be fabricated opening two active windows

next to each other, with the selectively regrown p -SiGe material creating a continuous base, as shown in Figure 4.

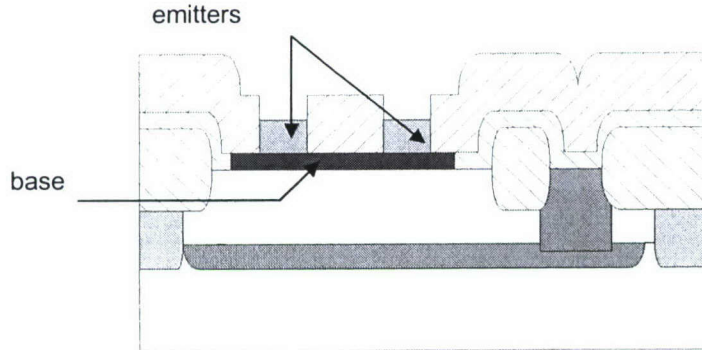


FIGURE. 4. Multiemitter HBT fabrication in a BiCMOS process with selective growth of a continuous p -SiGe base and separate emitters in adjacent active windows.

The next step in the MT-HBT project was fabrication on the industrial Si fab line at Agere. Unfortunately, while the masks for the MT-HBT fabrication in a $0.25\ \mu\text{m}$ process were designed in 2000-1, the fabrication never took place due to the difficulties experienced by Agere Systems in that period – including the eventual dismantlement of the Orlando fab running the BiCMOS process. The loss of the industrial collaborator, combined with the general ascendance of silicon-on-insulator (SOI) technology over bulk CMOS and BiCMOS,[3,4] the team proceeded to focus on interband and resonant tunneling transistors. Having realized the crucial need for industry-compatible fabrication, we pursued these devices in collaboration with LETI-CEA, a world-leading laboratory with a fully qualified 8" fab line. The resulting lateral interband and vertical tunneling transistors (LITT and VTT, respectively) are described in the next two Sections.

3. Lateral interband tunneling transistor (LITT)

The lateral interband tunneling transistor (LITT) based on gate-controlled source-drain tunneling in a heavily doped lateral pn junction in a thin Si channel on SOI. The original idea of a three-terminal gated tunneling structure dates back to a paper by Shockley and Hopper in the context of a pn avalanche process[5]. A number of groups subsequently fabricated FET-like tunneling devices, where the interband tunneling took place between an inversion channel and a counter-doped source, and demonstrated gate control of the tunneling current.[6]

We took a different approach to the LITT, dispensing with the inversion channel altogether (as it increases device area and adds capacitance). Instead, we start directly with a heavily-doped lateral pn junction in a thin Si film, with a gate electrode on top – see Figure. 5. The thin Si film reduces the source-drain capacitance and leakage current, while V_G (of either polarity) alters the maximum electric field \mathcal{E}_{MAX} by adding a vertical field component to the V_D -controlled lateral

field in the junction. Both forward and reverse source-drain bias operation are possible, but reverse-bias operation is better for high-speed applications due to the absence of minority carrier injection. A very short $L_G \sim 10$ nm gate could overlap the depletion region only, which minimizing the gate capacitance, but our proof-of-concept prototypes, fabricated in collaboration with LETI-CEA, had $L_G = 0.35\text{--}0.5$ μm defined by optical lithography – see Figure. 5.

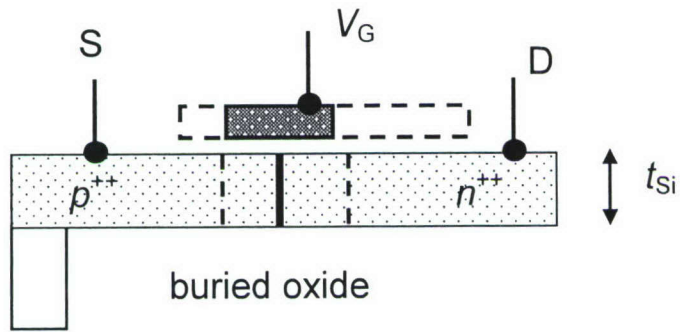


FIG. 5. Schematic LITT layout, bold line marks the pn junction, dashed lines indicate the lateral depletion region. Ideally, the gate overlaps depletion region only (hatched); in the first fabricated prototypes,[7] the gate also overlapped source and drain regions (dashed).

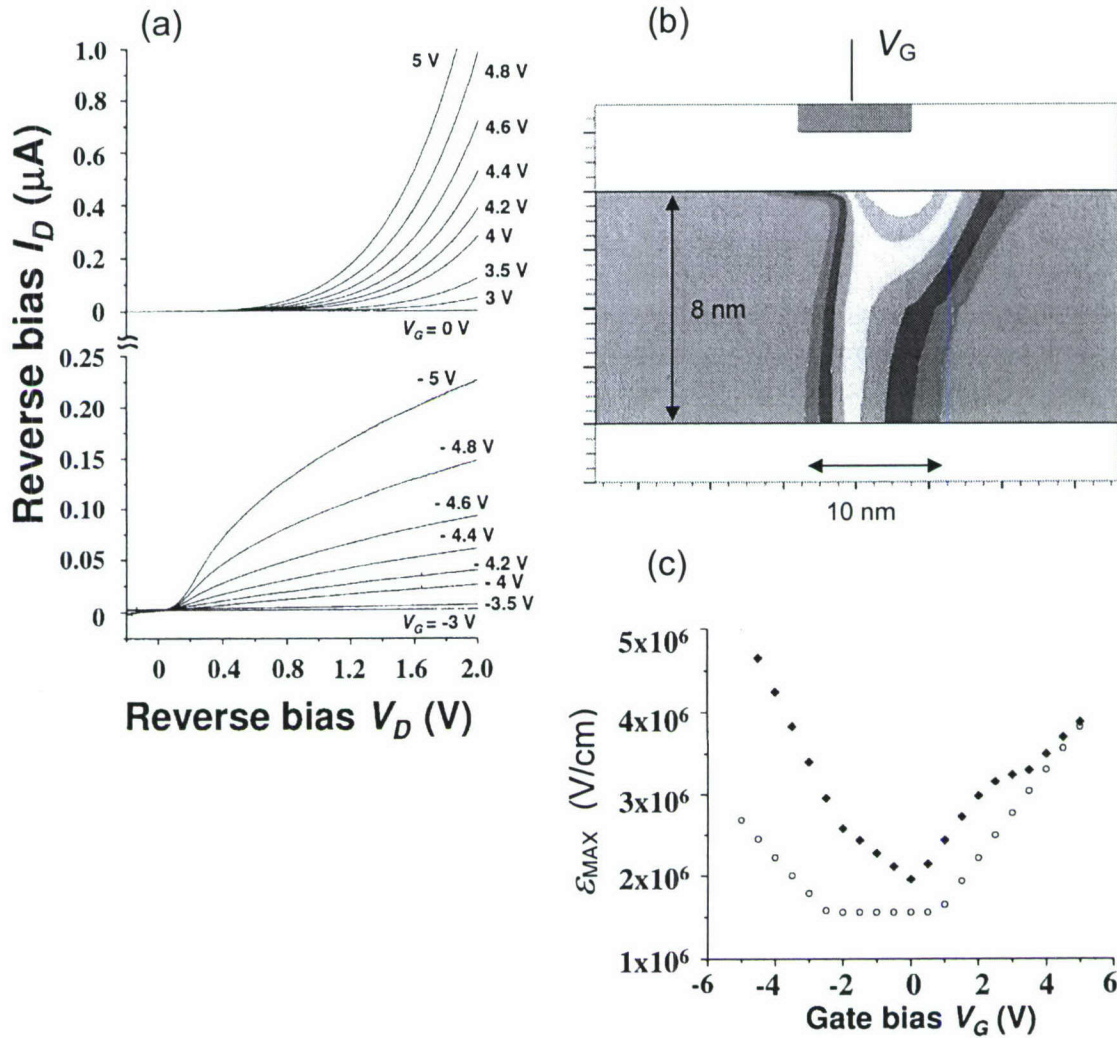


FIGURE. 6. (a) Reverse-bias $I_D(V_G, V_D)$ LITT curves at $T = 300$ K as a function of V_G (Si film thickness $t_{\text{Si}} \sim 40$ nm, gate oxide ~ 5 nm); (b) Silvaco simulation of the electric field in an ideally abrupt junction in a thin film $t_{\text{Si}} = 8$ nm with an aligned gate; (c) simulated maximum electric field ϵ_{MAX} vs. V_G at $V_D = -1$ V in the fabricated double-implanted prototype devices (circles) and an optimized device with a perfectly abrupt junction, thin silicon film $t_{\text{Si}} = 8$ nm, $L_G = 9$ nm, and 2 nm gate oxide (diamonds).⁷

Figure 6(a) shows the experimental $I(V)$ characteristics at room temperature. Gate control over interband tunneling is effective in producing transistor-like characteristics, although the gate voltages required are higher than ideal, at $V_G \sim 3$ –4 V. This is due to the insufficiently sharp and doped pn junction in the channel. In order to gauge the promise of the LITT, we simulated an optimized device with thinner Si channel, $t_{\text{Si}} = 8$ nm, with an ideally abrupt junction. The resulting electric field distribution in the channel at $V_D = -1$ V and $V_G = 2$ V is shown in Figure. 6(b), and the maximum simulated ϵ_{MAX} of the fabricated and ideally abrupt junction devices are

shown in Figure. 6(c). Clearly, in the simulated abrupt junction device, the field \mathcal{E}_{MAX} that controls the phonon-assisted tunneling in the transistor is much higher, so such a device would operate with much higher transconductance at lower V_G . It should be emphasized that with source and drain contacts of opposite polarity, the LITT is not affected by short channel effects and does not obey the scaling limitations of a MOSFET, at least not in any obvious way. This may become critical for future devices and there is currently quite a bit of interest in such tunneling structures, as exemplified by recent publications from other groups.[6,8]

4. Vertical tunneling transistor (VTT)

The devices described in the preceding sections were based on interband tunneling. The miniaturization of SOI structures, with available Si channel and gate thicknesses dropping to the nanoscale, also make it possible to envision devices based on intraband resonant tunneling. In collaboration with LETI-CEA, we realized a prototypical Si-based vertical tunneling transistor (VTT)[9]. This device layout is essentially identical to a normal transistor, but the Si channel is thinned down under the gate to the geometrical quantization regime (< 5 nm) and the gate oxide is kept sufficiently thin (down to 0.8 nm) to allow gate to channel tunneling. This gate-to-channel tunneling current is controlled with a backgate voltage V_{BG} that alters the alignment between the occupied electron states in the gate and the quantized subbands in the channel, see Figure. 7. The current is extracted laterally via the source and drain contacts. The device was originally invented by one of the PI's decades ago in the III-V heterostructure context,[10] but is ideally suited for SOI devices, where the buried oxide provides perfect isolation between the substrate gate and the Si channel. When operated as a gate-controlled VTT, with source shorted to drain and I_G originating from tunneling from the gate to the channel, we observe structure in the $I_G(V_{\text{BG}})$ due to resonant tunneling into the quantized channel subbands. At the same time, our SOI transistors show excellent room-temperature transistor characteristics. In the future, as SOI fabrication advances and the buried oxides are reduced, these quantum effects will become stronger and appear at lower V_{BG} , offering the prospect of ULSI-compatible devices with standard transistor operation or quantum functionality depending on electrode biasing.

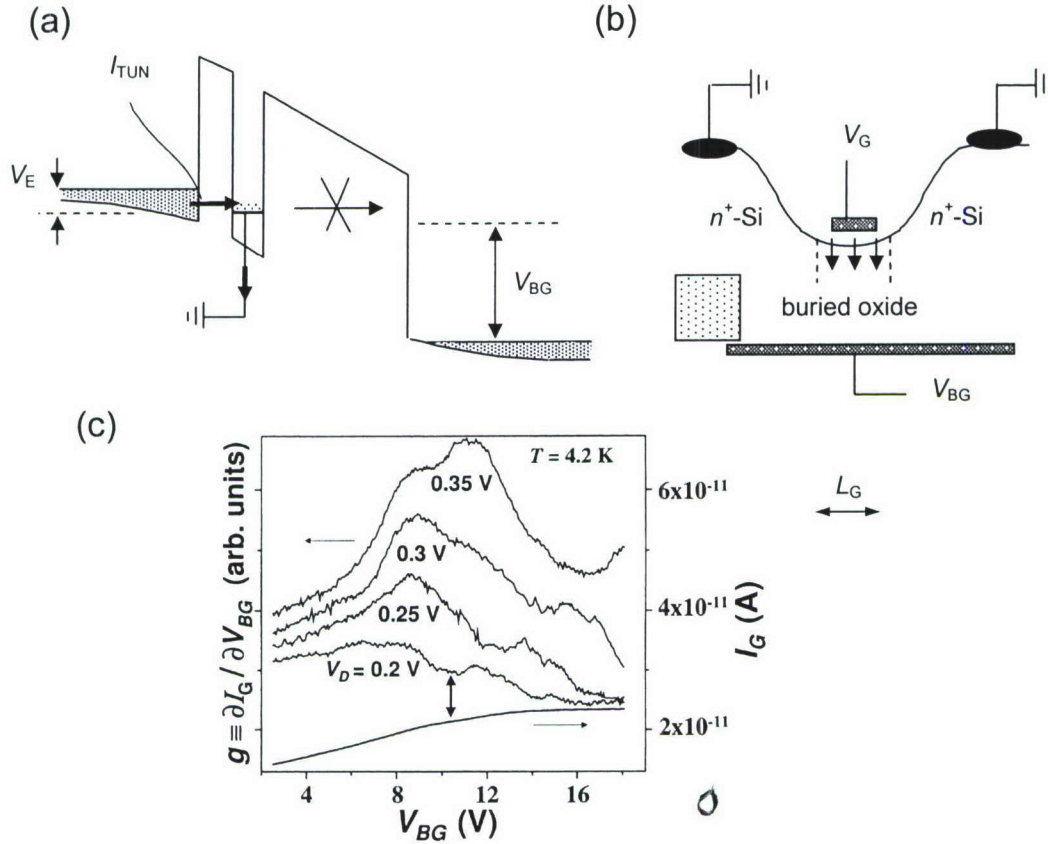


FIGURE 7. (a) Vertical tunneling transistor band diagram: the tunneling current from emitter to the quantized channel is controlled by the substrate gate V_G and extracted laterally via an independent contact to the channel; (b) SOI realization of this device, with the current tunneling from the poly-Si gate into the ultra-thin (< 5 nm) Si channel; (c) tunneling $I_G(V_{BG})$ and transconductance $g(V_{BG})$ characteristics, showing features due to tunneling into the channel subbands.⁹

In looking at the tunneling current and transconductance data of Figure 7(c), it is clear that the tunneling current in this proof-of-concept device is small – a consequence of the unacceptable high tunnel barrier arising from the use of SiO_2 as the barrier material. When the alternative high- κ dielectrics required for further downscaling of silicon transistors become available, all of the main candidates (like HfO_2 and La_2O_3) have much lower conduction band barriers than SiO_2 , which would increase the tunneling I_G by orders of magnitude. Significantly, the transconductance at higher $V_D = 0.35$ V contains two features, corresponding to tunneling into the lowest and the second subbands of the Si QW. As described in the following section, the selective tunneling into the second QW subband, combined with lateral extraction of the current, raises the intriguing possibility of subband population inversion in the Si QW – potentially a route to a long-wavelength Si-based optical source.

5. Population inversion and the possibility of a Si-based intersubband laser.

Provided a sufficiently uniform and more transmissive tunneling barrier becomes available, a slightly modified VTT structure could enable an intersubband laser compatible with dominant SOI technology.[11] The fundamental operating principle involves preferentially filling a higher-energy subband E_2 in a quantum well via tunneling and extracting the carriers from a lower subband E_1 , producing stimulated emission at $\hbar\omega = (E_2 - E_1)$. Population inversion requires that once carriers relax radiatively to E_1 they should leave the active region faster than E_2 is filled. An intersubband source involving resonant tunneling for both filling E_2 and emptying E_1 in a double-well structure was originally proposed for GaAs/AlGaAs;[12] and the same mechanism underpins the rapidly developing of III-V quantum cascade lasers (QCLs). Since the radiative transition is intersubband, no direct bandgap is required and a Si quantum well can also be used for the gain medium. The proposed SOI-based intersubband laser is based on a modified VTT structure of Figure. 8, where the poly-Si gate thickness is kept down to ~ 20 nm (to minimize free carrier absorption) and the substrate should be undoped, with only a thin, heavily doped layer near the buried oxide interface to which V_{BG} can be applied.

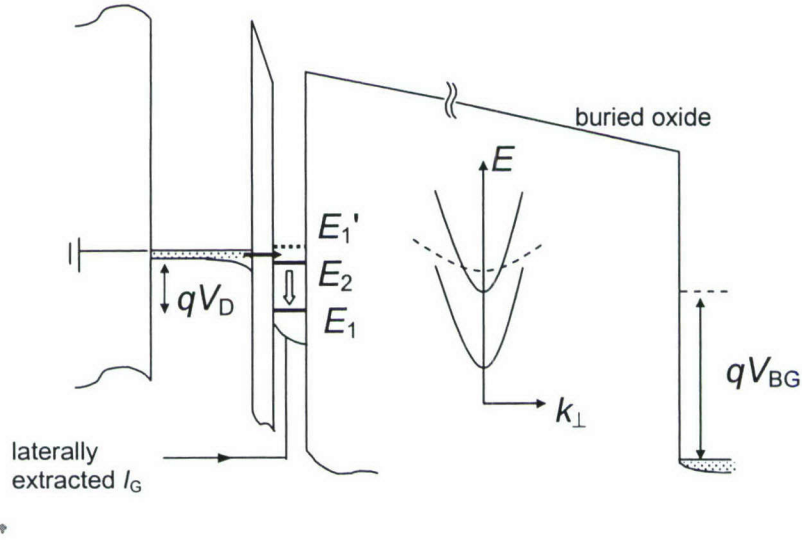


FIGURE. 8. Modified VTT structure for achieving intersubband population inversion. The radiative transition is shown with an open arrow, the in-plane dispersions of the 2D subbands are shown in the inset.

Exactly as in the VTT, electrons tunnel from the gate electrode into the E_2 subband in the Si QW and are extracted laterally at the contacts. The in-plane dispersions of the relevant subbands in the Si QW are shown schematically in the inset of Figure 8. Doubly-degenerate subbands E_1 and E_2 correspond to the heavy electron mass in the quantization direction and are light in the plane, whereas the fourfold-degenerate subband E_1' corresponds lies above E_2 and is heavy in the plane. Coupling between E_2 and E_1' reduces the in-plane diffusivity in the E_2 subband.

Once injected into the E_2 subband, electrons diffuse laterally towards the contacts with a diffusion constant D_2 . They will relax to the lowest E_1 subband with a characteristic lifetime τ

and there also diffuse towards the contacts, with a different diffusion coefficient D_1 . As long as the energy separation $(E_2 - E_1)$ lies below the Si optical phonon energy, nonradiative relaxation to E_1 is suppressed. Assuming uniform injection from the gate, the diffusion equation in the QW can be solved, leading to carrier densities n_2 and n_1 for the upper and lower subband, respectively. Defining $L_D \equiv (D_2\tau)^{1/2}$ as the diffusion length in the upper subband with respect to relaxation to E_1 and setting $L = L_G/2$, where L_G is the gate length of the transistor (see Figure. 7(b)) one obtains in the limit of $L_D > L$:

$$\frac{n_2(x)}{n_1(x)} = \frac{D_1}{D_2} \left(\frac{12L_D^2}{5L^2 - x^2} - 1 \right) \quad (1)$$

Thus, Eq. (1) predicts population inversion even for equal diffusion coefficients $D_1 = D_2$, because the electrons do not have time to relax from E_2 to E_1 during their diffusion towards the contacts. The ratio D_1/D_2 increases the inversion further, as the in-plane diffusivity D_2 is expected to be markedly smaller because of the interaction with the nearby E_1' subband that has a heavy in-plane mass and a large density of states.

Several other necessary conditions are needed of an effective infrared source, using a typical vertical III-V QCL design for comparison. Given the intersubband nature of the $E_2 \rightarrow E_1$ transition, the optical matrix element in our Si QW is, in principle, quite similar to that in a GaAs QW. In order to avoid competing nonradiative relaxation via phonon emission, the Si QW in Figure. 8 should not be too narrow, *e.g.* if $t_{Si} = 6$ nm we have $(E_2 - E_1) \sim 30$ meV $< \hbar\omega_{LO}$ in Si. Our structure is based on a single QW and cannot easily be repeated, due to the SOI substrate fabrication technology. As a result, the optical confinement Γ at $\lambda = 40$ μm is very weak for the TM mode, despite the large refractive index discontinuity between Si and SiO_2 :

$$\Gamma = 2\pi^2 (d/\lambda)^2 (\epsilon_{\text{SiO}_2}/\epsilon_{\text{Si}}) (\epsilon_{\text{Si}} - \epsilon_{\text{SiO}_2}) \sim 10^{-3} \quad (2)$$

where $d \sim 25$ nm is the total thickness of the active structure (thin 20 nm poly-Si gate, tunneling dielectric, and $t_{Si} = 6$ nm SOI channel). Consequently, there is no significant difference between the optical field intensity in the Si QW gain region and the doped poly-Si gate and substrate regions, which are the regions of optical loss due to free-carrier absorption. To overcome the free-carrier absorption losses we need to get the sheet density n_2 in the upper E_2 subband to reach at least $3 \times 10^{11} \text{ cm}^{-2}$. The tunneling current densities measured in the VTT of Figure. 7(c) were far too small to achieve such a charge density in the well, but an alternative dielectric barrier with a smaller barrier height could be used to increase the current density. As a result, operation at $\lambda = 40$ μm may be feasible.

6. Germanium-on-insulator tunneling devices.

Finally, during the last months of the MURI project, we embarked on a collaboration with IBM Research at Yorktown, where an epitaxy group led by S. Guha has developed a technique for

growing all-epitaxial Ge/high- κ dielectric heterostructures lattice-matched to Si(111).[13] The eventual aim was to use the smaller bandgap and hole effective mass of Ge to increase the interband tunneling currents in the LITT and to use the lower epitaxial LaYO dielectrics as tunnel barriers in the VTT. It is worth noting that current technology is trending away from Si/SiO₂-based transistors, so new material combinations, including GeOI channels with high- κ dielectrics, are predicted to enter mainstream technology.

However, before proceeding with quantum effect devices, we needed to demonstrate acceptable field-effect transistor performance in ultrathin GeOI channels. Figure 9 illustrates the preliminary transistor characteristics of an ultrathin (5 nm) single-crystal Ge-OI transistor using 15 nm of LaYO as the gate dielectric.[14] The measurements on large devices show high on/off current ratio ($>10^6$ at $T = 77$ K, $\sim 10^3$ at $T = 300$ K). Furthermore, the channel can be inverted from hole to electron operation – the transistor curves in Figure. 9 are of the same device! Given this starting material, we plan to fabricate VTT and LITT transistors in the coming year or two.

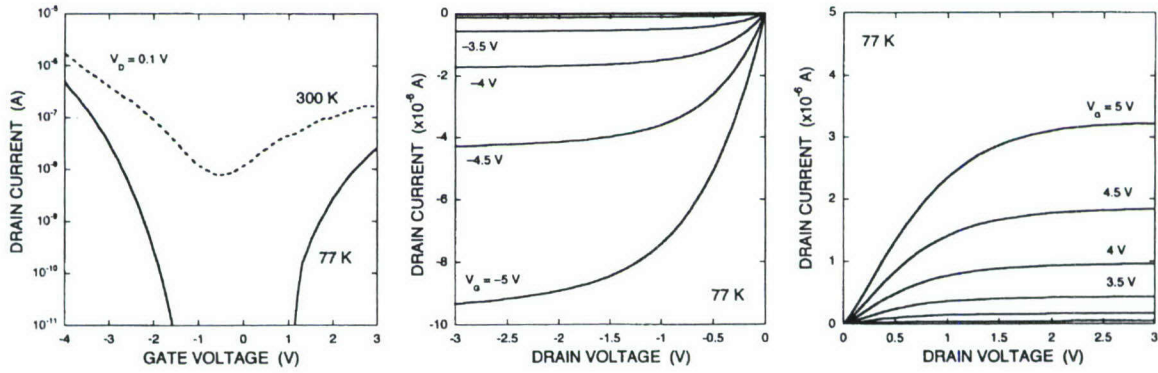


FIGURE. 9. Complementary transistor characteristics of the same ultrathin all-epitaxial GeOI device at $T = 300$ and 77 K. The Ge channel is ~ 5 nm, LaYO insulator is ~ 15 nm, source-drain separation $L = 10$ μm , layout is shown in the inset. Note the complete shut off and inversion of the channel carriers by backgate voltage V_G at $T = 77$ K.

Task #5: Gallium Nitride FETs – Strain, Giant Piezoelectric Fields, Electronic Confinement, and Coherent Phonons: Project Leader: Arto Nurmikko (Brown)

Co-participants: H. Maris (ballistic phonons), S. Luryi (heterostructure physics) Industry/Gov't Lab Link: QinitiQ Ltd (England), Sandia National Laboratory

We have applied an optical probing technique on AlGaN/GaN field-effect transistors to demonstrate that coherent GHz phonons are generated copiously under large signal operation. The phonon generation originates from time varying electron screening of the piezoelectric polarization fields in the active region, and may provide a non-diffusive means of energy dissipation for high power devices. The unintentionally doped AlGaN/GaN heterointerface in an FET supports a high density 2-dimensional (2D) electron gas up to densities on the order of 10^{13} cm^{-2} . Due to the wurtzite crystal structure and lattice mismatch strain, such heterostructures are profoundly influenced by built-in spontaneous and piezoelectric polarization fields and associated charges. The piezoelectric component implies a coupling between the electronic and lattice degrees of freedom whose role we investigate experimentally in this letter. Specifically, in the dynamical case, i.e. a HEMT operating at microwave frequencies, the time varying density changes in the 2D electron channel are expected to induce a synchronous time dependent strain, i.e. launching of coherent acoustic phonons due to dynamical screening of the large piezoelectric fields ($> 1 \text{ MV/cm}$). If so, such a mechanism raises a question of its potential importance when considering how problems of energy dissipation by conventional diffusive heat transport might be superseded by propagating nonthermal lattice excitations in future, very high power, nitride HEMTs.

In the present experiments, we have studied the coherent phonon generation mechanism in GaN/AlGaN microwave HEMTs, operating in a large signal regime near 1 GHz. We detect the phonons by using a local reflective optical probe at near normal incidence to the active device, tightly focused and scanned in the vicinity of the source-gate-drain region. The devices were based on undoped heterojunction consisting of 28 nm of AlGaN (23% Al) on 1.2 μm thick GaN, grown by metalorganic vapor phase epitaxy (MOVPE) in a close-coupled showerhead reactor on insulating SiC (0001) substrates. HEMTs were fabricated using a conventional mesa-isolated device technology with Ti/Al/Ti/Au ohmic contacts and Ni/Au Schottky gates. The particular devices used in our proof-of-concept experiments had a center-fed gate 200 μm in width and the source-to-drain length about 5 μm , giving the device a typical operating frequency near 1 GHz

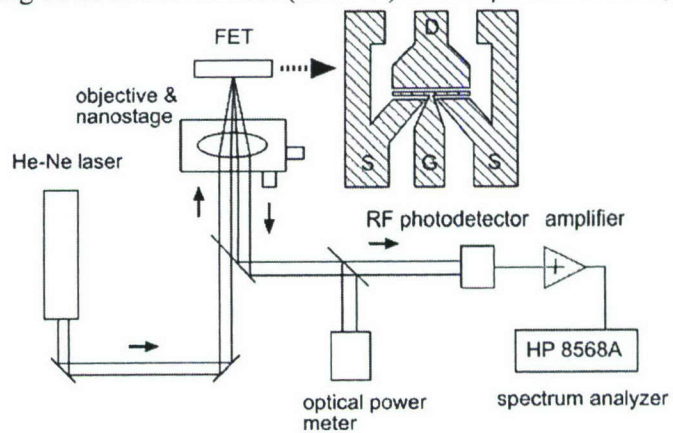
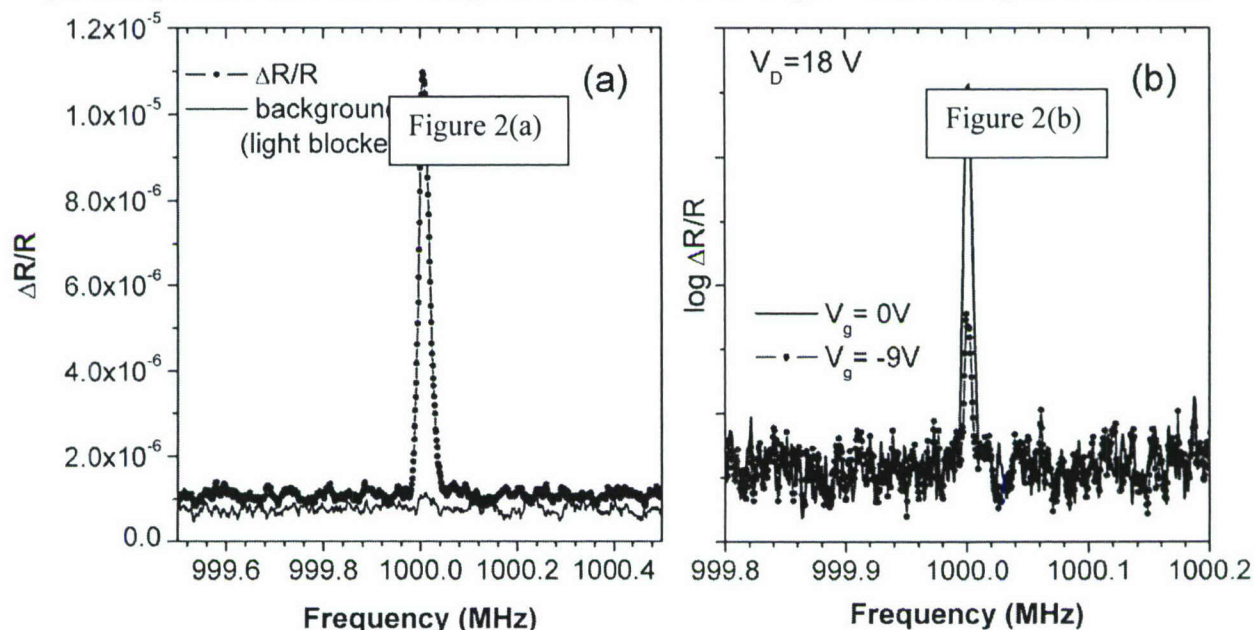


Figure 1

Figure 1 shows the optical experimental diagram and a plan view of the transmission line electrode layout for the source, gate, and drain contacts of the HEMTs, which were contacted through standard microwave probes and operated by a network analyzer. A stable cw He-Ne laser was used as the probe and was focused by a long working distance microscope objective (NA 0.55) onto the devices with a spot size of 1 μm . The changes in the intensity of the reflected

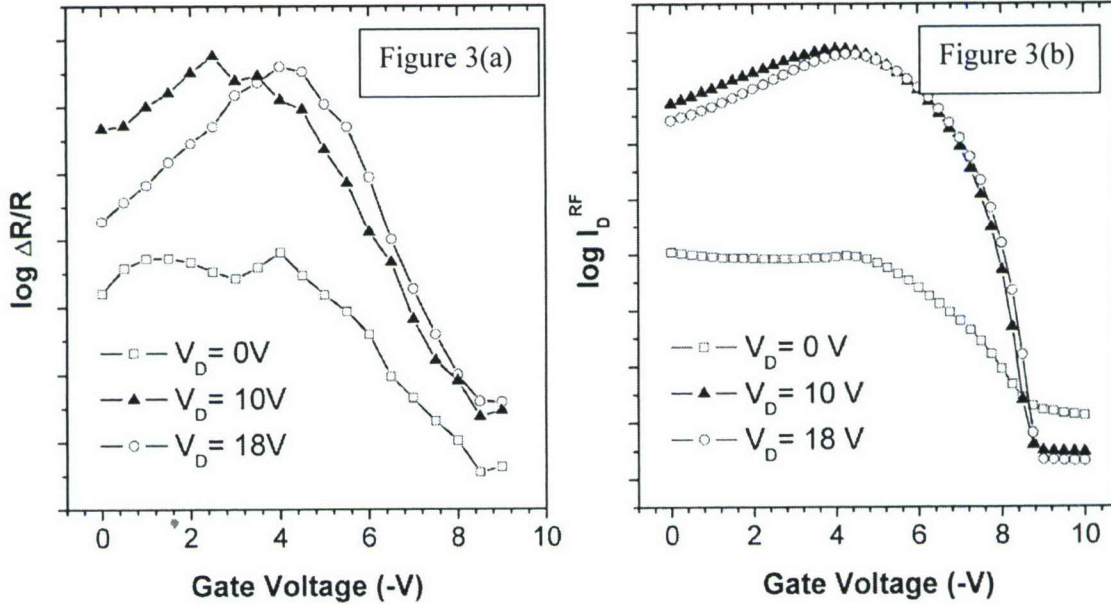


beam (ΔR) were frequency analyzed following detection by an rf shielded fast photodiode, while the average reflected power was monitored so as to normalize the measured ΔR to account for possible local reflectance variations of the device surface.

With the HEMTs biased in operation near 1 GHz, we readily found modulated reflectivity signals $\Delta R/R$ at the corresponding frequency, while focusing the probe beam either on the metallic electrodes or in the space between them where the AlGaIn surface was exposed (see Figure. 1). A wide spatial area of signal presence is expected, given the long mean free path for \sim GHz phonons in GaN (several mm), and the dominance of the photoelastic effect which modulates the index of refraction in proportion to the phonon amplitude. **Figure 2(a)** shows an example of the frequency spectrum of modulated reflectance $\Delta R/R$ with a peak precisely at the HEMT's operating frequency, with the probe beam focused on the drain electrode, a few μm away from the junction. Such modulated reflectance formed the basis of studying the physics of the optical effect including its dependence on the transistor bias conditions and details of the location of the probe spot on the device as a function of the rf amplitude. The signal $\Delta R/R$ (here at 1.00002 GHz) vanishes as the laser beam is blocked; this and other checks unambiguously establish that its origin is due to the reflectivity modulation induced by the electrical excitation of the HEMT. **Figure 2(b)** shows a "snapshot" of the variation of the optical signal $\Delta R/R$ for two values of the gate bias voltage at 1.2 V input rf amplitude.

The magnitude of the measured modulated reflectivity was in the range of $\Delta R/R \sim 10^{-5}$. Its origin can in principle involve electro-optic, thermal, or photoelastic effects. While an electro-optic effect (i.e. direct electric field induced changes of refractive index), is possible with the probe beam directly incident on the AlGaIn/GaN material, this is forbidden to first order when the probe is reflected from the metal electrode (as free electron metals possess inversion symmetry). Diffusive thermal effects are, of course, too slow to make a contribution in our microwave frequency range. Hence the photoelastic effect, namely the changes in the index of refraction at the metal/air or nitride/air interface due to coherent strain launched within the HEMT must dominate the optical response, as expected. We note in passing that these types of high frequency strains, that is coherent acoustic phonons, are routinely used as a materials diagnostic technique in so-called “picosecond ultrasonic” experiments where a thin film metallic transducer deposited atop the material of interest is used both to generate and “read out” dynamical strains via the photoelastic effect in the all-optical pump-probe experiments.

The amplitude of ΔR was studied systematically as a function of device bias conditions over a wide range of the HEMTs operation. **Figure 3** shows an example of such a dependence, which



compares the measured $\Delta R/R$ (Figure. 3 (a)) with the output rf current I_D^{RF} (Figure. 3 (b)), both as a function of the gate bias voltage for various source to drain voltages. The input rf amplitude was 1.2 V in both cases and the probe spot for the ΔR measurement was positioned at the drain metallic electrode. The two sets of data show qualitative consistency in terms of the optimal operating point and, notably, the pinch-off behavior of the HEMT, lending further support to the argument that the photoelastic optical signal, and thus the coherent GHz phonons are driven by the dynamically varying the 2D electron density within the HEMT channel. Comprehensive details of the bias dependence in these measurements will be presented elsewhere.

In contrast to the all-optical coherent phonon experiments mentioned above, the geometry and boundary conditions in the HEMT devices are complex in terms of the spatial “shape” of the coherent phonon source and its radiation pattern. Given the micrometer sized spot of the optical

probe beam and the wavelength of the acoustic phonon in the structure (i.e., $\sim \mu\text{m}$ for $\sim 1\text{GHz}$ waves in GaN), we have acquired two-dimensional spatial images of $\Delta R/R$ by scanning the laser probe across the device, under fixed bias conditions. The strongest signal is measured in the region between the gate and the drain contacts. This is where the pinch-off occurs in the channel and, therefore, modulation of the electron density and local generation of the phonons should be maximized. In fact, we have found that such maps, covering areas of tens of μm^2 (i.e. well beyond the immediate source-gate-drain) and being frequency dependent, exhibit distinct local “hot spots”, whose location varies with bias conditions. In our interpretation, these local maxima in phonon amplitude may well be produced by phonon focusing effects, which have been dramatically demonstrated in anisotropic materials in the GHz frequency range. Since our optical maps give only a surface profile of the vibrational energy density generated and propagating within the device, open questions remain as to the sensitivity of our experiment to device inhomogeneities and possible anisotropies associated with phonon focusing and scattering in the full three dimensions.

Task #6: Phonons and Nonthermal Cooling In Heterostructure Devices: Project Leader: Humphrey Maris (Brown)

Participants: G. Belenky (QC lasers), Q. Hu (THz lasers), A. Nurmikko (nitride devices), S. Pei (IC lasers). Industry/Gov't Lab Link: Dow Chemical (low-k dielectric material characterization); Intel (Thermal management of microelectronic chips); Rudolph Technologies (Semiconductor wafer characterization equipment).

We collaborated with Intel and with Rudolph Technologies throughout the course of the MURI program. The flow of heat across interfaces and within small structures is of critical importance to both of these industrial companies.

Work within this task was performed in the following areas:

1.) Thermal transport through multilayer nanostructures: The thermal transport through multilayer semiconductor heterostructures is of great importance for the operation of many opto- and microelectronic devices. The thermal conductivity in superlattices has been measured to be substantially reduced relative to the conductivity of the component materials. In short period GaAs/AlAs superlattices, for example, the conductivity is as much as a factor of ten smaller than in bulk GaAs. A part of this reduction can be attributed to the modifications of the phonon dispersion relation that arise from zone folding. Zone folding reduces the average group velocity of phonons propagating in the direction normal to the superlattice planes. However, the effect of this zone-folding is predicted to give a reduction in conductivity that is greatest for layer thickness around 10 monolayers. Based on the zone-folding effect the conductivity of superlattices would be expected to increase for shorter period superlattices. However, experimental measurements show that the conductivity decreases monotonically as the layer thickness is reduced in the range 1 to 10 monolayers, and thus disagree with the expectations based on zone folding.

To achieve a more complete understanding of how heat flows through a superlattice, we constructed a molecular dynamics simulation program to model heat flow in multilayered structures. The motion of atoms in a section of the structure with dimensions 3200 atoms by 20 atoms by 20 atoms is simulated (1.3×10^6 atoms), with the temperature gradient in the x-direction (long direction). To find the thermal conductivity we first gave each atom a random velocity consistent with a local temperature. The initial temperature distribution was taken to vary with x as

$$T(x) = T_0 + \Delta T_0 \cos(2\pi x / L)$$

where L is the length of the sample in the x -direction, T_0 is considered to be the ambient temperature and ΔT_0 is small compared to T_0 . The variation of the temperature distribution with time was found and from this the thermal conductivity was determined.

The simulations were run on an array of Pentium personal computers. In order to test for the convergence of the results, some calculations for even larger structures were performed on the Hitachi SR8000 supercomputer at the University of Hokkaido, Sapporo, Japan.

We investigated the variation of the conductivity with superlattice layer thickness for a simplified model of GaAs/AlAs. For structures with ideal smooth interfaces, the results of the simulations were in qualitative agreement with the trend expected from zone folding as shown in Figure. 1. We then studied the effect of atomic scale roughness at the interfaces. We found that even a small amount of disorder had a significant effect on the thermal conductivity of short period superlattices. With the inclusion of roughness, the results of the simulations (see Figure. 2) are in very good agreement with the experimental data.

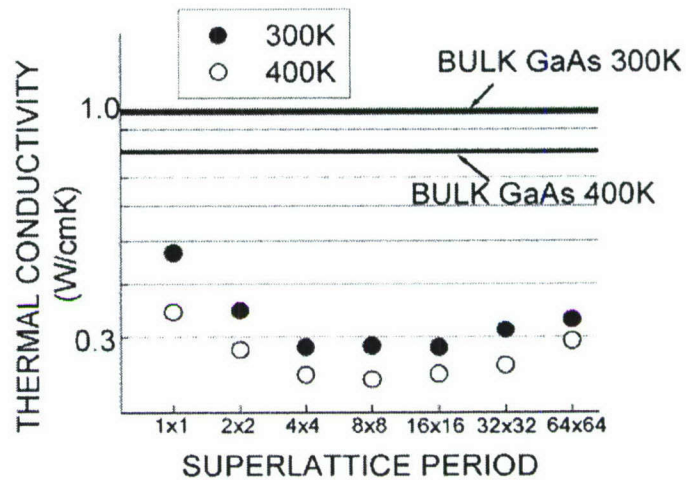


Fig. 1. Results of molecular dynamics calculations of the thermal conductivity of GaAs/AlAs

We then extended this work to include a study of heat flow in the direction parallel to the superlattice layers. We found that the conductivity in this direction is also reduced compared to the bulk materials, by a smaller amount. The results are shown in Figure. 3. This work was performed in collaboration with the group of Professor S. *Tamura at the University of Hokkaido.

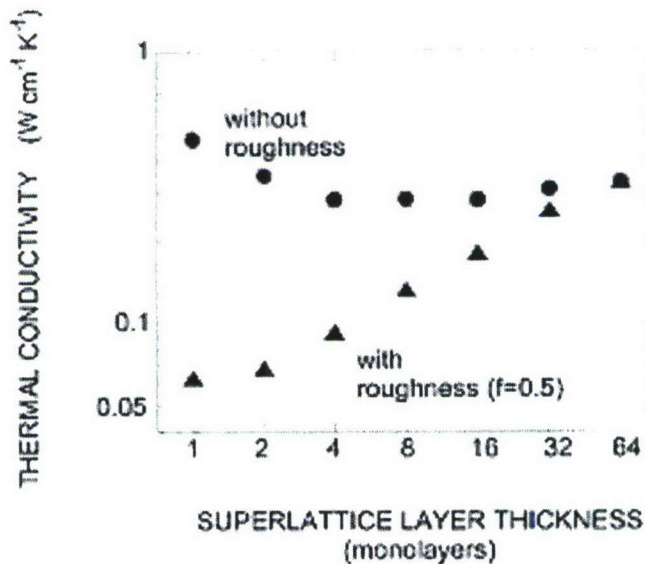


Fig. 2. Results of molecular dynamics calculations of the thermal conductivity of GaAs/AlAs superlattices showing the effect of roughness of the interfaces.

A significant part of the research effort in this general area was directed towards achieving an understanding of the accuracy limitations of molecular dynamics simulation of heat flow in nanostructures. This effort included studies of how the result obtained for the thermal conductivity depended on the dimensions of the structure that was simulated. In addition, comparison was made between the results obtained using the method just described in which the decay of a temperature distribution

was monitored, and methods in which a hot and cold reservoirs were attached to the ends of the sample.

The majority of the simulation work that was performed at Brown was performed by Brian Daly. On graduation, Daly took a postdoctoral position at the University of Michigan and is now an Assistant Professor in the physics department at Vassar College.

We also performed some analytical calculations of phonon scattering rates. Low energy longitudinal phonons play an especially important role in thermal conductivity. The scattering rate of these phonons is the result of a particular phonon-phonon scattering mechanism first considered by Herring. The scattering rate is strongly influenced by crystal symmetry and elastic anisotropy. We performed a detailed investigation of this mechanism in tellurium oxide.

2.) Thermal conductivity measurement in structures and materials of technical interest:

Measurement of the thermal conductivity of thin films and nanostructures is a key element of the MURI research effort. Conventional methods for measuring thermal conductivity are not easily employed on the nanoscale. We developed an all optical technique to make this type of measurement. A thin metal film was deposited on top of the nanostructure and this was heated using a picosecond light pulse. The rise in temperature of the metal film caused a small change in the optical reflectivity which was measured using a time-delayed probe light pulse. From the rate of cooling of the metal film the heat conduction of the structure that it was

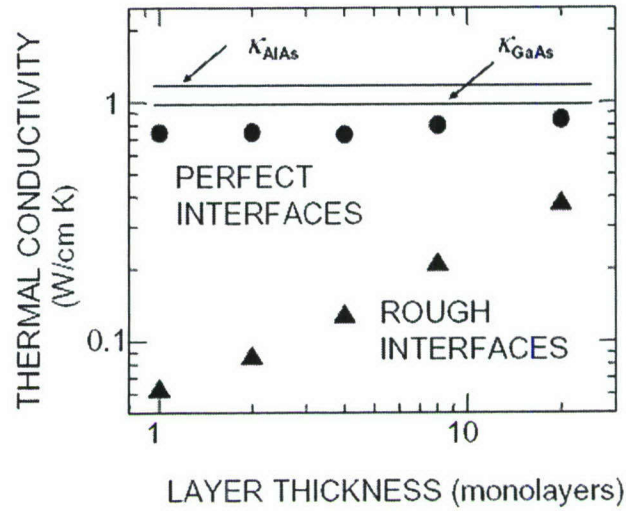


Fig. 3. Results of molecular dynamics calculations of the thermal conductivity in the in plane direction for GaAs/AlAs superlattices

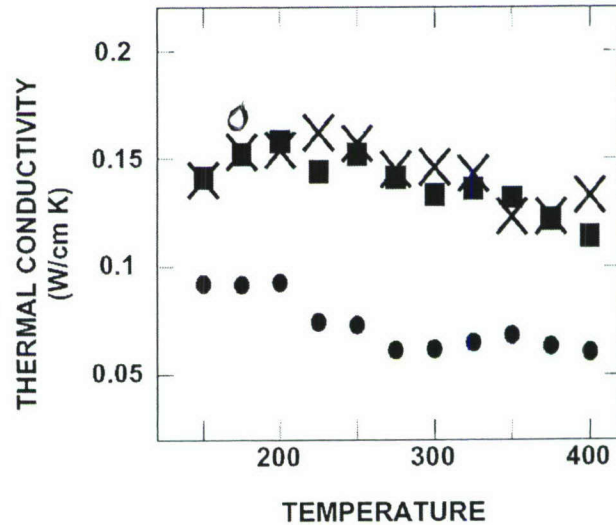


Figure 4. Thermal conductivity of $\text{Al}_{0.18}\text{Ga}_{0.82}\text{N}$ (\times), $\text{Al}_{0.20}\text{Ga}_{0.80}\text{N}$ (\blacksquare), and $\text{Al}_{0.44}\text{Ga}_{0.56}\text{N}$ (\bullet) versus temperature.

attached to could be reliably determined. Measurements were made of the thermal conductivity of low- k dielectric films that are currently being used as insulation in computer chips at Intel and other companies. We also made an investigation of the thermal conductivity of GaN and Ga thin films grown by our collaborators.

The status of heat flow studies in nanostructures was summarized in an extensive review article written in collaboration with other leading scientists working in this field.

3.) *Coherent phonon experiments:* In heat flow experiments the transport arises from an incoherent distribution of phonons. The study of coherent phonons is also an important topic. Studies of coherent phonons can provide key information about the mechanisms of phonon transport and scattering. Coherent phonons can also be used as probes of both the geometry and mechanical properties of nanostructures. For example, Rudolph Technologies employ coherent phonons to measure the thickness and other properties of thin metal films in computer and memory chips.

Coherent phonons are also used in acoustic microscopes which have found many practical applications. In these microscopes coherent phonons are first generated in a solid, then cross an interface into a liquid and are brought to a focus. Most microscopes use water as the coupling fluid because of its low attenuation. We measured this attenuation using coherent phonons generated and detected with ultrafast optical techniques.

A coherent phonon pulse can be generated optically. In this type of experiment, a metal film is deposited onto the surface of a sample. When a sub-picosecond light pulse is absorbed in the film a thermal stress is suddenly set up. The relaxation of this stress launches a coherent phonon (strain pulse) into the sample. When this strain pulse enters a second metal film on the other side of the sample, it causes a small change in the optical reflectivity of the film which can be detected by means of a probe light pulse. In this way, it is possible to generate and detect phonons with frequency up to about 1 THz. When these phonons propagate through a crystal the shape of the strain pulse changes because of phonon dispersion and elastic non-linearity. The dispersion broadens the pulse and the non-linearity generates harmonics and sharpens the pulse. For a certain range of initial pulse shapes and amplitudes the pulse can break up into a number of acoustic solitons. These are acoustic pulses of fixed shape each traveling through the crystal with a different velocity that is slightly larger than the velocity of sound. We fabricated a specially-designed sample with metal and dielectric films deposited onto a magnesium oxide crystal in a way such that it was possible to generate a strain pulse with an initial shape that was accurately known. By varying the intensity of the ultra-fast light pulse used for generation, we could control the amplitude of the initial strain pulse while keeping its shape constant. The number of solitons that were produced increased as the amplitude of the initial strain pulse was raised as shown in Figure. 5. Since all relevant parameters entering in the experiment were reliably known, it was possible to construct a detailed theory of the velocity of the solitons and their number (see Figure. 6). The agreement between theory and experiment was excellent.

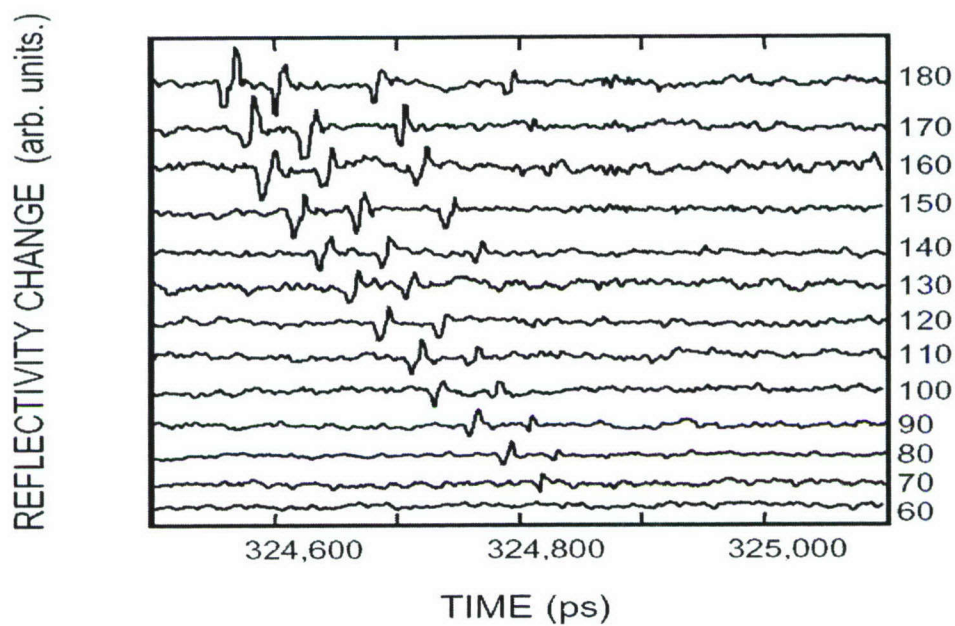


Figure 5. Results of an experiment to study acoustic solitons propagating in a crystal of MgO. The different curves are labeled by the power in mW of the laser used to generate the strain pulses.

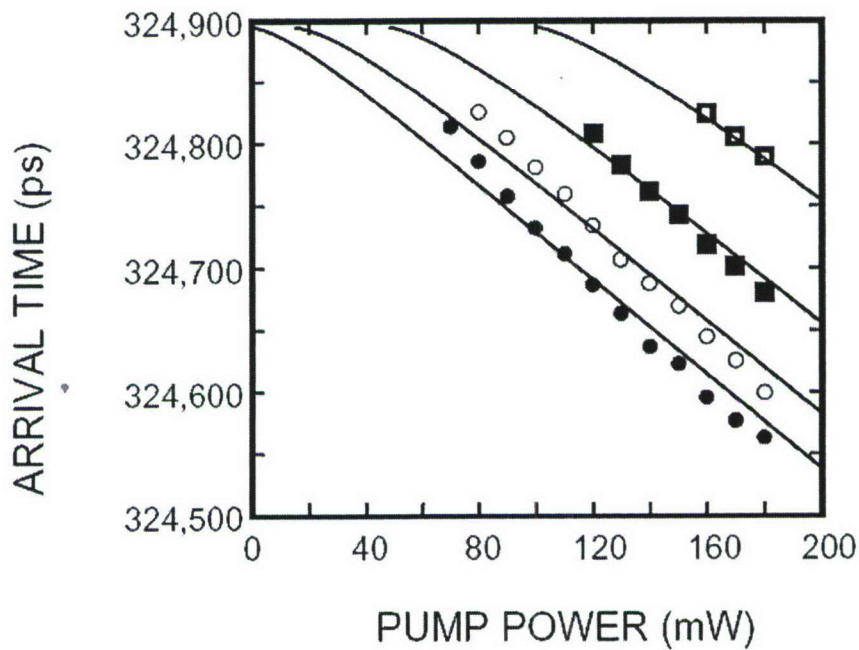


Figure 6. Arrival time of the different solitons as a function of the power in mW of the laser used to generate the strain pulses. The time for low amplitude sound to travel across the sample is approximately 324,900 ps.

4. PERSONNEL SUPPORTED

TASK #1

Faculty: Q. Hu (MIT)

Staff: Benjamin S. Williams (Postdoctoral associate)

Graduate Students (partial support): Benjamin S. Williams

Kostas Konistis

Hans Callebaut

Sushil Kumar (MIT)

TASK #2

Faculty: Serge Luryi, Professor.

Gregory Belenky, Professor

Staff: Mikhail Kisin, Research Scientist.

Sergey Suchalkin, Research Scientist.

Levon Asryan, Visiting Research Scientist

Graduate Students: Leon Shterengas, PhD student.

David Westerfeld, PhD student.

Thomas Cummings, Undergraduate Student

TASK #3

Faculty: Shin-Shem Steven Pei (U. of Houston)

Staff: C.H. Hsiang

Graduate Students: R. Yang

D. Zhang

TASK #4

Faculty: A. Zaslavsky (Brown)

Graduate Students: Jun Liu, Ph.D. student
Cagri Aydin, Ph.D.
Dimitrios Kazazis, Ph.D. student

TASK #5

Faculty: Arto Nurmikko (Brown)

Staff: J. Song (Postdoctoral Associate)

Graduate Students: Eleni Makarona, Ph.D. student
Lu Chen, Ph.D. student

TASK #6

Faculty: H.J. Maris (Brown).

Graduate Students (partial support): Brian Daly
Peter Zannitt
Madhavi Chand
Leslie Shelton.

5. REFERENCES CITED

Task #1

No References Cited

Task #2

- [1] J.R.Meyer, C.A.Hoffman, and F.J.Bartoli, L.R.Ram-Mohan, *Appl.Phys.Lett.*, 67, 757 (1995).
- [2] R.Q. Yang, J.M. Xu, *Appl. Phys. Lett.* 59, 181 (1991).
- [3] M.V. Kisin, M.A. Stroschio, S. Luryi, and G. Belenky, *Physica E* 10, 576 (2001).
- [4] Yu. B. Lyanda-Geller, J.-P. Leburton, *Appl. Phys. Lett.* 67, 1423 (1995).
- [5] J. Faist, F. Capasso, C. Sirtori, D.L. Sivco, A.L. Hutchinson, M.S. Hybertsen, A.Y.Cho, *Phys. Rev. Lett.* 76, 411 (1996).
- [6] M.A. Stroschio, M.V. Kisin, G. Belenky, S. Luryi, *Appl. Phys. Lett.* 75, 3258 (1999).
- [7] W.W.Bewley, H.Lee, I.Vurgaftman, R.J.Menna, C.L.Felix, R.U.Martinelli, D.W.Stokes, D.Z.Garbuzov, J.R.Meyer, M.Maiorov, J.C.Connolly, A.R.Sugg, and G.H.Olsen, *Appl. Phys. Lett.*, 76, 256 (2000).
- [8] C.L.Felix, W.W.Bewley, I.Vurgaftman, R.E.Bartolo, D.W.Stokes, J.R.Meyer, M.J.Yang, H.Lee, R.J.Menna, R.U.Martinelli, D.Z.Garbuzov, J.C.Connolly, M.Maiorov, A.R.Sugg, and G.H.Olsen, *Appl. Optics*, 40, 806 (2001).
- [9] R.Q.Yang, J.L.Bradshaw, J.P.Bruno, J.T.Pham, *IEEE J. Quantum Electron.*, 37, 282 (2001).
- [10] H.Q.Le, C.H.Lin, and S.S.Pei, *Appl. Phys. Lett.*, 72, 3434 (1998).
- [11] W.W.Bewley, I.Vurgaftman, C.L.Felix, J.R.Meyer, C.-H.Lin, D.Zhang, S.J.Murry, S.S.Pei, and L.R.Ram-Mohan, *J. Appl. Phys.*, 83, 2384 (1998).
- [12] W.W.Bewley, C.L.Felix, I.Vurgaftman, D.W.Stokes, J.R.Meyer, H.Lee, and R.U.Martinelli, *IEEE Phot. Tech. Lett.*, 12, 477 (2000).
- [13] D.V.Donetsky, G.L.Belenky, D.Z.Garbuzov, H.Lee, R.U.Martinelli, G.Taylor, S.Luryi, J.C.Connolly, *Electronic Lett.*, 35, 298 (1999).
- [14] N.Tessler and G.Eisenstein, *Appl. Phys. Lett.*, 62, 10 (1993).
- [15] V.B.Gorfinkel and S.Luryi, *Journal of Lightwave Technology*, 13, 252 (1995).
- [16] L.V.Ašryan, N.A.Gun'ko, A.S.Polkovnikov, G.G.Zegrya, R.A.Suris, P-K Lau and T.Makino, *Semicond. Sci. Technol.*, 15, 1131 (2000).
- [17] Garbuzov, M.Maiorov, H.Lee, V.Khalfin, R.Martinelli, and J.Connolly, *Appl. Phys. Lett.*, 74, 2990 (1999).
- [18] W.W.Bewly, C.L.Felix, E.H.Aifer, I.Vurgaftman, L.J.Olafsen, J.R.Meyer, H.Lee, R.U.Martinelli, J.C.Connolly, A.R.Sugg, G.H.Olsen, M.J.Yang, B.R.Bennett, and B.V.Shanabrook, *Appl.Phys. Lett.*, 73, 3833 (1998).
- [19] R.Q. Yang, J.L. Bradshaw, J.D. Bruno, J.T. Pham, and D.E. Wortman, *IEEE Journal of Quantum Electronics*, 37, 282 (2001).
- [20] B.H. Yang, D. Zhang, Rui Q. Yang, C.-H. Lin, S.J. Murry, and S.S. Pei, *Appl. Phys. Lett.*, 72, 2220 (1998).
- [21] E.V. Arzhanov, A.P. Bogatov, V.P. Konyaev, O.M. Nikitina, and V.I. Sheikin, *Quantum Electron.*, 24, 581 (1994).
- [22] E.P. O'Reilly, A.I. Onischenko, E.A. Avrutin, D. Bhattacharyya and J.H. March, *Electron. Lett.*, 34, 2035 (1998).

- [23] M. V. Kisin, S. D. Suchalkin, G. Belenky, J. D. Bruno, R. Tober, and S. Luryi, *Appl. Phys. Lett.*, 85, 4310 (2004).
- [24] D. Westerfeld, S. Suchalkin, M. Kisin, G. Belenky, J. Bruno, R. Tober, *IEE Proc.- Optoelectron.*, 150, 293 (2003).
- [25] J. Bruno, G. Belenky, S. Suchalkin, R. Tober “Recent Performance Advances in Type II Interband Cascade Lasers”, International Workshop on Quantum Cascade Lasers, Seville, Spain, 4-8 Jan. 2004.
- [26] J.L. Bradshaw, N.P. Breznay, J.D. Bruno, J.M. Gomes, J.T. Pham, F.J. Towner, D.E. Wortman, R.L. Tober, C.J. Monroy, K. Olver, *Photonic Spectra*, 20, 479 (2004)
- [27] R.Q. Yang, *Proceedings of the 27th International Conference on Physics of Semiconductors*, Flagstaff, 2004.
- [28] W.W. Bewley, I. Vurgaftman, C.S. Kim, M. Kim, C.L. Canedy, J.R. Meyer, *Appl. Phys. Lett.*, 85, 5544 (2004).
- [29] J.G. Kim, L. Sterengas, R.U. Martinelli, G.L. Belenky, *Appl. Phys. Lett.*, 83, 1926 (2004).
- [30] A. Evans, J.S. Yu, S. Slivken, M. Razeghi, *Appl. Phys. Lett.*, 85, 2166 (2004).
- [31] S. Suchalkin, D. Donetski, D. Westerfeld, R. Martinelli, I. Vurgaftman, J.R. Meyer, S. Luryi, G. Belenky, *Appl. Phys. Lett.*, 80, 2833 (2002).
- [32] I. Vurgaftman, J.R. Meyer, L.R. Ram-Mohan, *J. Appl. Phys.*, 89, 5815 (2001).
- [33] A. Ongstad, R. Kaspi, J.R. Chavez, G.C. Dente, M.L. Tilton, d.M. Guarandi, *J. Appl. Phys.*, 92, 5621 (2002).
- [34] R. Kaspi, A. Ongstad, C. Moeller, G.C. Dente, J. Chavez, M.L. Tilton, D. Guarandi, *Appl. Phys. Lett.*, 79, 302 (2001).
- [35] D. Westerfeld, S. Suchalkin, R. Kaspi, A. Ongstad, G. Belenky, *IEEE Journ. Of Quant. Electron.*, 40, 1657 (2004).
- [36] M. Gurioli, J. Martinez-Pastor, M. Colocci, C. Deparis, B. Chastaingt, J. Massies, *Phys. Rev. B*, 46, 6922 (1992).
- [37] J.R. Botha, A.W.R. Leitch, *Phys. Rev. B*, 50, 18147 (1994).
- [38] L. Shterengas, G.L. Belenky, J.G. Kim, and R.U. Martinelli, *Semicond. Sci. Tech.* 19, 655 (2004).
- [39] M.I. Dyakonov, V. Yu. Kachorovskii, *Phys. Rev. B*, 49, 17130 (1994).
- [40] G.G. Zegrya, A.S. Polkovnikov, *Phys. Rev. B*, 86, 315 (1998).
- [41] L.A. Coldren, S.W. Corzine, *IEEE J. Quantum Electron.*, QE-23, 903 (1987).
- [42] S. Kobayashi, Y. Yamamoto, M. Ito, T. Kimura, *IEEE J. Quantum Electron.*, QE-18, 582 (1982).
- [43] K. Ploog and G.H. Dohler, *Advances in Physics* 32, 285 (1983).
- [44] H. Kroemer and G. Griffiths, *IEEE Electron Device Letters* EDL-4, 20 (1983).
- [45] J. Faist, F. Capasso, C. Sirtori, D.L. Sivco, A.L. Hutchinson and A.Y. Cho, *Nature* 387, 777 (1994).
- [46] N. Le Thomas, N.T. Pelekanos, Z. Hatzopoulos, E. Aperathitis, R. Hamelin, *Appl. Phys. Lett.* 83, 1304 (2003).
- [47] L.V. Asryan and S. Luryi, *IEEE J. Quantum Electronics* 37, 905 (2001), *Solid State Electronics* 47, 205 (2003).
- [48] L.V. Asryan, S. Luryi, US Pat. 6,870,178
- [49] G. Walter, J. Elkow, N. Holonyak, Jr., R. D. Heller, X. B. Zhang, and R. D. Dupuis, *Appl. Phys. Lett.* 84, 666 (2004).
- [50] S. Pradhan, S. Ghosh, and P. Bhattacharya, *Electron. Lett.*, 38, 1449 (2002)

Task #3

- [5.1] L. Yang, J. F. Chen, and A. Y. Cho, J. Appl. Phys., Vol 68, Issue 6, pp. 2997, 1990
- [5.2] J. Goldman, D. C. Tsui and J. E. Cunningham, Phys. Rev.Lett., 58, p1256, 1987
- [5.3] R. Magno, A.S.Bracker, B.R.Bennett, B.Z.Nosho and L.J.Whitman, J. Appl. Phys. Vol.90, p6177, 2001
- [5.4] J. Foster, M. L. Leadbeater, et al., Phys. Rev., B39, p6205, 1989
- [5.5] R. Nogaret, M.A.Maldonado, R.E.Carnahan, K.P. Martin, A.Y.Cho, et al., Physical Review B, vol.47, p13872, 1993
- [5.6] R.Bennett, A.S.Bracker, R. Magno, J.B.Boos, R.Bass and D.Park, J. Vac. Sci. Technol. B, vol.18, p1650, 2000
- [5.7] F.Chen, A.Y.Cho, J. Appl. Phys. Vol.72, p960, 1992
- [5.8] F. Young, B. M. Wood, H. C. Liu, M. Buchanan, and D. Langheer, A. J. Spring Thorpe and P. Mandeville, Appl. Phys. Lett., 52 (17), P25,1988
- [5.9] Y. belhadj, K. P. Martin, S. Ben Amor, et al., Appl. Phys. Lett., 57, p58,1990
- [5.10] A. Nogaret, M.A.Maldonado, R.E.Carnahan, K.P. Martin, R.J. Higgins, A.Y.Cho, et al., J. Appl. Phys. Vol.74, p6443, 1993
- [5.11] E.E. Mendez, J. Nocera, and W.I.Wang, Phys. Rev. B, Vol.45, p3910, 1992
- [5.12] M.P.Houng, Y.H.Wang, and C.L.Shen, J.Appl.Phys., Vol 70, Iss. 8, p4640-4642, 1991

Task #4

- [1.] Proposed by Z. S. Gribnikov and S. Luryi, "Article comprising a bipolar transistor with a floating base", U.S. patent #5,461,245 (1994); demonstrated by A. Zaslavsky, S. Luryi, C. A. King, and R. W. Johnson, "Multiemitter Si/Ge_xSi_{1-x} hetero-junction bipolar transistor with no base contact and enhanced logic functionality", *IEEE Electron Dev. Lett.* **EDL-18**, 453 (1997).
- [2.] A. Zaslavsky, D. Mariolle, S. Deleonibus, D. Fraboulet, S. Luryi, J. Liu, C. Aydin, M. Mastrapasqua, C. A. King, and R. Johnson, "Interband tunneling-based ULSI-compatible silicon devices", in: H. R. Huff, L. Fabry, and S. Kishino, eds., *Semiconductor Silicon 2002* Vol 2 (Proc. 9th Intern. Symp. Silicon Mater. Sci. Technology), Pennington, NJ: Electrochemical Society, 2002, pp. 956-967.
- [3.] G. K. Celler and S. Cristoloveanu, "Frontiers of silicon-on-insulator", *J. Appl. Phys.* **93**, 4955 (2003).
- [4.] S. Luryi and A. Zaslavsky, "Blue sky in SOI: new opportunities for quantum and hot-electron devices", *Solid State Electronics* **48**, 877 (2004).
- [5.] W. Shockley and W. W. Hooper, "The surface controlled avalanche transistor", *Proc. WESCON* 1964, p. 12.1; see <http://www.ece.sunysb.edu/~serge/Shockley-Hooper-1964.pdf> for this hard-to-find reference.
- [6.] See, for example, T. Nirschl *et al.* "Scaling properties of the tunneling field effect transistor (TFET): Device and circuit", *Solid State Electronics* **50**, 44 (2006) and references therein.
- [7.] C. Aydin, A. Zaslavsky, S. Luryi, S. Cristoloveanu, D. Mariolle, D. Fraboulet, and S. Deleonibus, "Lateral interband tunneling transistor in silicon-on-insulator", *Appl. Phys. Lett.* **84**, 1780 (2004).

- [8.] Since the LITT publication of 2004, the number of Si interband tunneling devices in the literature has been considerable, including industrial R&D labs; the latest European Solid State Device conference (ESSDERC 2006) had several presentations on the topic.
- [9.] A. Zaslavsky, C. Aydin, S. Luryi, S. Cristoloveanu, D. Mariolle, D. Fraboulet, and S. Deleonibus, "Ultrathin silicon-on-insulator vertical tunneling transistor", *Appl. Phys. Lett.* **83**, 1653 (2003).
- [10] S. Luryi, "Mechanism of operation of double-barrier resonant-tunneling oscillators", *Tech. Digest IEDM* (1985), pp. 666-669.
- [11] S. Luryi and A. Zaslavsky, "On the possibility of an intersubband laser in silicon-on-insulator", *Intern. J. High Speed Electronics Systems* **16**, 411 (2006); also as a chapter in: H. Iwai, Y. Nishi, M. S. Shur, and H. Wong, eds. *Frontiers in Electronics* (Proc. Workshop Frontiers Electronics 2004), Singapore: World Scientific, 2006.
- [12] A. Kastalsky, V. J. Goldman, and J. H. Abeles, "Possibility of infrared laser in resonant-tunneling structure", *Appl. Phys. Lett.* **59**, 2636 (1991).
- [13] N. A. Bojarczuk, M. Copel, S. Guha, V. Narayanan, E. J. Preisler, F. M. Ross, and H. Shang, "Epitaxial
- [14] E. J. Preisler, S. Guha, B. R. Perkins, D. Kazazis, and A. Zaslavsky, "Ultrathin all-epitaxial germanium on insulator devices", *Appl. Phys. Lett.* **86**, 223504 (2005).

Task #5

No References Cited

Task #6

No References Cited

6. PUBLICATIONS & BOOK CHAPTERS

Task #1

- J.L. Adam, I. Kašalynas, J.N. Hovenier, T.O. Klaassen, J.R. Gao, E.E. Orlova, B.S. Williams, S. Kumar, Q. Hu, and J. L. Reno, "Beam pattern of Terahertz quantum cascade lasers with sub-wavelength cavity dimensions," *Appl. Phys. Lett.* **88**, 151105 (2006).
- J.L. Adam, I. Kašalynas, J.N. Hovenier, T.O. Klaassen, J.R. Gao, E.E. Orlova, B.S. Williams, S. Kumar, Q. Hu, and J. L. Reno, "Beam pattern of Terahertz quantum cascade lasers with sub-wavelength cavity dimensions," *Appl. Phys. Lett.* **88**, 151105 (2006).
- Baryshev, J. N. Hovenier, A. J. L. Adam, I. Kasalynas, J. R. Gao, T. O. Klaassen, B. S. Williams, S. Kumar, Q. Hu, and J. L. Reno, "Phase-lock and free-running linewidth of a two-mode terahertz quantum cascade laser," *Appl. Phys. Lett.* **89**, 031115 (2006).
- Baryshev, J. N. Hovenier, A. J. L. Adam, I. Kasalynas, J. R. Gao, T. O. Klaassen, B. S. Williams, S. Kumar, Q. Hu, and J. L. Reno, "Phase-lock and free-running linewidth of a two-mode terahertz quantum cascade laser," *Appl. Phys. Lett.* **89**, 031115 (2006).
- L. Betz, R. T. Boreiko, B. S. Williams, S. Kumar, Q. Hu, and J. L. Reno, "Frequency and Phaselock Control of a 3-THz Quantum Cascade Laser," *Opt. Lett.* **30**, 1837 (2005).
- H. Callebaut, S. Kumar, B. S. Williams, and J. L. Reno, "Analysis of transport and thermal properties of THz quantum cascade lasers," *Appl. Phys. Lett.* **83**, 207 (2003).

- H. Callebaut, S. Kumar, B. S. Williams, Q. Hu, and J. L. Reno, "Importance of electron-impurity scattering for electron transport in THz quantum-cascade lasers," *Appl. Phys. Lett.* **84**, 645 (2004).
- H. Callebaut and Q. Hu, "Importance of coherence for electron transport in terahertz quantum cascade lasers," *J. Appl.* **98**, 104505 (2005). Also published in *Virtual Journal of Nanoscale Science & Technology*, **12**(24), December 12, (2005).
- J. R. Gao, J. N. Hovenier, Z. Q. Yang, J. J. A. Baselmans, A. Baryshev, M. Majenius, T. M. Klapwijk, A. J. L. Adam, T. O. Klassen, B. S. Williams, S. Kumar, Q. Hu, and J. L. Reno, "A terahertz heterodyne receiver based on a quantum cascade laser and a superconducting bolometer," *Appl. Phys. Lett.* **86**, 244104 (2005). Also published in *Virtual Journal of Nanoscale Science & Technology*, **11**(24), June 20 (2005).
- Q. Hu, B. S. Williams, S. Kumar, H. Callebaut, and J. L. Reno, "Terahertz quantum cascade lasers based on resonant phonon scattering for depopulation," *Phil. Trans. R. Soc. London* **A362**, 233-249 (2004).
- Q. Hu, B. S. Williams, S. Kumar, H. Callebaut, and J. L. Reno, "Phonon-Depopulated THz Quantum Cascade Lasers," pp. 319-329, *Future Trend in Microelectronics: The Nano, the Giga, and the Ultra*, S. Luryi, J. Xu, A. Zaslavsky, eds., John Wiley & Sons, New York, 2004.
- Q. Hu, B. S. Williams, S. Kumar, H. Callebaut, S. Kohen, and J. L. Reno, "Resonant-phonon-assisted THz Quantum Cascade Lasers with Metal-metal Waveguides," a Topical Issue on TERAHERTZ TECHNOLOGY, *Journal of Semiconductor Science and Technology*, **20**, S228-S236 (2005).
- S. Kohen, B. S. Williams, and Q. Hu, "Electromagnetic modeling of terahertz quantum cascade laser waveguides and resonators," *J. Appl. Phys.* **97**, 053106 (2005).
- S. Kumar, B. S. Williams, Q. Hu, and J. L. Reno, "1.9-THz quantum-cascade lasers with one-well injector," *Appl. Phys. Lett.* **88**, 121123 (2006).
- S. Kumar, B. S. Williams, S. Kohen, Q. Hu, and J. L. Reno, "Continuous-wave operation of terahertz quantum-cascade lasers above liquid-nitrogen temperature," *Appl. Phys. Lett.* **84**, 2494 (2004).
- W. M. Lee and Q. Hu, "Real-Time, Continuous-Wave Terahertz Imaging using a Microbolometer Focal-Plane Array," *Opt. Lett.* **30**, 2563 (2005). Also reported in *Opto&Laser Europe*, page 14, December (2005).
- H. C. Liu, M. Wächter, D. Ban, Z. R. Wasilewski, M. Buchanan, G. C. Aers, J. C. Cao, S. L. Feng, B. S. Williams, and Q. Hu, "Effect of doping concentration on the performance of terahertz quantum-cascade lasers," *Appl. Phys. Lett.* **87**, 141102 (2005).
- E. Orlova, J. N. Hovenier, T. O. Klassen, I. Kasalynas, A. J. L. Adam, A. Baryshev, J. R. Gao, T. M. Klapwijk, B. S. Williams, S. Kumar, Q. Hu, and J. L. Reno, "Antenna model for wire lasers," *Phys. Rev. Lett.* **96**, 173904 (2006).
- M. S. Vitiello, G. Scamarcio, B. S. Williams, S. Kumar, Q. Hu, and J. L. Reno, "Measurement of subband electronic temperatures and population inversion in THz quantum cascade lasers," *Appl. Phys. Lett.* **86**, 111115 (2005).
- B. S. Williams, H. Callebaut, S. Kumar, Q. Hu, and J. L. Reno, "3.4-THz quantum cascade laser based on LO-phonon scattering for depopulation," *Appl. Phys. Lett.* **82**, 1015 (2003). Also published in *Virtual Journal of Nanoscale Science & Technology*, **7**(8), February 24 (2003).
- B. S. Williams and Q. Hu, "Optimized energy separation for phonon scattering in three-level terahertz intersubband lasers," *J. Appl. Phys.* **90**, 5504 (2001).

- B. S. Williams, S. Kumar, H. Callebaut, Q. Hu, and J. L. Reno, "3.4 THz quantum cascade laser operating above liquid nitrogen temperature," *Electro. Lett.* **39**, 915 (2003).
- B. S. Williams, S. Kumar, H. Callebaut, Q. Hu, and J. L. Reno, "Terahertz quantum cascade laser at $\lambda \approx 100 \mu\text{m}$ using metal waveguide for mode confinement," *Appl. Phys. Lett.* **83**, 2124 (2003).
- B. S. Williams, S. Kumar, H. Callebaut, Q. Hu, and J. L. Reno, "Terahertz Quantum Cascade Lasers Operating up to 137 K," *Appl. Phys. Lett.* **83**, 5142 (2003).
- B. S. Williams, S. Kumar, Q. Hu, and J. L. Reno, "Resonant-phonon terahertz quantum-cascade laser operating at 2.1 THz ($\lambda \approx 141 \mu\text{m}$)," *Elect. Lett.* **40**, 431 (2004).
- S. Williams, S. Kumar, Q. Hu, and J. L. Reno, "High-power terahertz quantum-cascade lasers," *Elect. Lett.* **42**, 89 (2006).
- S. Williams, S. Kumar, Q. Hu, and J. L. Reno, "Operation of terahertz quantum-cascade lasers at 164 K in pulsed mode and at 117 K in continuous-wave mode," *Optics Express*, **13**, 3331-3339 (2005). Also published in *Virtual Journal of Nanoscale Science & Technology*, **11**(25), June 27, (2005).
- S. Williams, S. Kumar, Q. Hu, and J. L. Reno, "Distributed-feedback terahertz quantum-cascade lasers using laterally corrugated metal waveguides," *Opt. Lett.* **30**, 2909 (2005).

Task #2

- L. V. Asryan, S. Luryi and R.A. Suris, "Intrinsic nonlinearity of the light-current characteristic of semiconductor lasers with a quantum confined active region", *Appl. Phys. Lett.*, **81**, 2154 (2002).
- L. V. Asryan, S. Luryi and R.A. Suris, "Internal efficiency of semiconductor lasers with a quantum confined active region", *IEEE Journal of Quantum Electronics* **39**, 404 (2003).
- L. V. Asryan and S. Luryi, "Temperature insensitive semiconductor quantum-dot laser", *Solid State Electronics*, **47**, 205 (2003).
- L. V. Asryan and S. Luryi, "Effect of internal optical loss on threshold characteristics of semiconductor lasers with a quantum-confined active region", *IEEE Journal of Quantum Electronics*, **40**, 833 (2004).
- L. V. Asryan and S. Luryi, "Two lasing thresholds in semiconductor lasers with a quantum-confined active region", *Applied Physics Letters*, **83**, 5368 (2003).
- L. V. Asryan and S. Luryi, "Tunneling-injection quantum dot laser: ultrahigh temperature stability", *IEEE Journal of Quantum Electronics* **37**, 905 (2001).
- M. Kisin, S. Suchalkin, G. Belenky, J. Bruno, R. Tober, S. Luryi, "Analysis of the temperature performance of type-II interband cascade lasers", *Appl. Phys. Lett.*, **85**, 4310 (2004).
- M. V. Kisin and S. Luryi, "Piezoacoustic modulation of gain and distributed feedback for quantum cascade lasers with widely tunable emission wavelength", *Appl. Phys. Lett.* **82**, 847 (2003).
- M. V. Kisin, M. A. Strosio, G. Belenky, S. Luryi, "Resonant phonon-assisted depopulation in type-I and type-II intersubband laser heterostructures", *Institute of Physics, Conference Series*, No 174, 443 (2003).
- M.V. Kisin, M.A. Strosio, G. Belenky, S. Luryi, "Interband Phonon-Assisted Tunneling in InAs/GaSb Heterostructures", *Physica B*, **316**, 223 (2002).
- S. Suchalkin, M.Kisin, G.Belenky, S.Luryi; F.Towner, J.Bruno, C.Monroy, R.Tober, "Widely tunable mid-IR interband cascade laser", *Appl. Phys. Lett.*, in press.

- S. Suchalkin, L. Shterengas, M. Kisin, S. Luryi, G. Belenky, R. Kaspi, A. Ongstad, J.G. Kim, R.U. Martinelli, "Mechanism of the temperature sensitivity of mid-infrared GaSb-based semiconductor lasers" *Appl.Phys.Lett.* 87, Art. No. 041102 (2005).
- S. Suchalkin, M.Kisin, G.Belenky, S.Luryi; Yu.Vasilyev, F.Towner, J.Bruno, R.Tober, "Electrically tunable cascaded mid-IR type II light source", *Proceedings of SPIE*, v.5738, 130 (2005).
- S. Suchalkin, J. Bruno, R. Tober, D. Westerfeld, M. Kisin, G. Belenky, "Experimental study of the optical gain and loss in InAs/GaInSb interband cascade lasers", *Appl.Phys.Lett.* 83, 1500 (2003).
- S. Suchalkin, D. Westerfeld, D. Donetski, S. Luryi, G. Belenky, R.U. Martinelli, I. Vurgaftman, J. Meyer, "Optical gain and loss in 3 μ m diode "W" quantum-well lasers", *Appl.Phys.Lett.*, 80, 2833 (2002).
- D. Westerfeld, S. Suchalkin, R. Kaspi, A. Ongstad, G.Belenky, "Absorption and single-pass gain measurements in optically pumped type-II midinfrared laser structures", *IEEE Journal of Quantum Electronics*, 40,1657 (2004).
- D. Westerfeld, S. Suchalkin, M. Kisin, G. Belenky, J. Bruno, R. Tober, "Experimental study of optical gain and loss in 3.4-3.6 μ m interband cascade lasers" IEE Proceedings-Optoelectronics, 150, 293 (2003).

Book Chapters

- L. V. Asryan and S. Luryi, "Quantum Dot Lasers: Theoretical Overview", Chap 4 in *Semiconductor Nanostructures for Optoelectronic Applications*, Todd Steiner, Editor, Artech House, Inc., Boston (2004) pp. 113-158.

Task #4

- C. Aydin, A. Zaslavsky, S. Luryi, S. Cristoloveanu, D. Mariolle, D. Fraboulet, S. Deleonibus, "Lateral interband tunneling transistor in SOI", *Appl. Phys. Lett.* 84, 1780 (2004).
- D. Kazazis, A. Zaslavsky, E. Tutuc, N. A. Bojarczuk, and S. Guha, "Negative differential resistance in ultra-thin Ge-on-insulator FETs", to appear in *Semicond. Sci. Technol.* (2007).
- S. Luryi and A. Zaslavsky, "Blue sky for SOI: New opportunities for quantum and hot-electron devices", invited paper, *Solid State Electronics* 48, 877 (2004).
- S. Luryi and A. Zaslavsky, "On the possibility of an intersubband laser in silicon-on-insulator", *Intern. J. High Speed Electronics Systems* 16, 411 (2006); also as a chapter in: H. Iwai, Y. Nishi, M. S. Shur, and H. Wong, eds. *Frontiers in Electronics (Proc. Workshop Frontiers Electronics 2004)*, Singapore: World Scientific, 2006.
- S. Luryi and A. Zaslavsky, "Nonclassical devices in SOI: Genuine or copyright from III-V", invited paper, to appear in *Solid State Electronics* (2007)
- E. J. Preisler, S. Guha, B. R. Perkins, D. Kazazis, and A. Zaslavsky, "Ultrathin all-epitaxial germanium on insulator devices", *Appl. Phys. Lett.* 86, 223504 (2005).
- A. Zaslavsky, D. Mariolle, S. Deleonibus, D. Fraboulet, S. Luryi, J. Liu, C. Aydin, M. Mastrapasqua, C. A. King, and R. Johnson, "Interband tunneling-based ULSI-compatible silicon devices", in: H. R. Huff, L. Fabry, and S. Kishino, eds., *Semiconductor Silicon 2002 Vol 2 (Proc. 9th Intern. Symp. Silicon Mater. Sci. Technology)*, Pennington, NJ: Electrochemical Society, 2002, pp. 956-967.

- A. Zaslavsky, C. Aydin, S. Luryi, S. Cristoloveanu, D. Mariolle, D. Fraboulet, and S. Deleonibus, "Ultrathin silicon-on-insulator vertical tunneling transistor", Appl. Phys. Lett. **83**, 1653 (2003).

Task #5

- B. C. Daly, H. J. Maris, A. V. Nurmikko, M. Kuball, and J. Han, J., "Optical Pump-and-Probe Measurement of the Thermal Conductivity of Nitride Thin Films", Appl. Phys. **92**, 3820 (2002)
- Yiping He, Lu Chen, Y.-K. Song, and A.V. Nurmikko, S.-R. Jeon, Z. Ren, M. Gherasimova, and J. Han "Optical Properties of Sub-100nm Diameter Nanoposts with Embedded InGaN Quantum Well Heterostructures", , Phys. Stat. Sol. (c) **2**, 2740 (2005)
- K. Jasim, Q. Zhang, A.V. Nurmikko, Aram Mooradian, Glen Carey, Wonill Ha, and Erich Ippen, "A Passively Mode-locked Vertical Extended Cavity Surface Emitting Diode Laser", Electronics Letters **39**, 373 (2003)
- Lu Chen and A.V. Nurmikko, "Fabrication and Performance of Efficient Blue Light Emitting III-Nitride Photonic Crystals", Appl. Phys. Lett. **85**, 3663 (2004)
- E. Makarona, B. Daly, J.-S. Im, , H. Maris, A. Nurmikko, and J. Han, "Coherent Generation of 100 GHz Acoustic Phonons by Dynamic Screening of Piezoelectric Fields in AlGaN/GaN Multilayers", Appl. Phys. Lett. **81**, 2791 (2002)
- J.-H. Song, Q. Zhang, W. Patterson III, A.V. Nurmikko, M. J. Uren, K. P. Hilton, R. S. Balmer and T. Martin, "Generation of Coherent Acoustic Phonons in AlGaN/GaN Microwave Field Effect Transistors", Appl. Phys. Lett. **83**, 1023 (2003)

Task #6

- G. A. Antonelli, W.K. Ford, C.J. Morath, R.J. Stoner, G. Tas and H.J. Maris, "Non-destructive Testing Using Picosecond Ultrasonics", *Review of Progress in Non-Destructive Evaluation*, Volume **25B**, editors D.O. Thompson and D.E. Chimenti, p. 210, (2005).
- B.C. Daly and H.J. Maris, "Calculation of the Thermal Conductivity of Superlattices by Molecular Dynamics Simulation", in the Proceedings of the 10th International Conference on Phonon Scattering in Condensed Matter, Physica **B 316-317**, 247 (2002).
- B.C. Daly, H.J. Maris, K. Imamura and S. Tamura, "Molecular Dynamics Calculation of the Thermal Conductivity of Superlattices", Phys. Rev. **B 66**, 024301 (2002).
- B.C. Daly, H.J. Maris, A.V. Nurmikko, M. Kuball, and J. Han, "Optical Pump-and-Probe Measurement of the Thermal Conductivity of Nitride Thin Films", Appl. Phys. Lett. **92**, 380 (2002).
- B.C. Daly, H.J. Maris, W.K. Ford, G.A. Antonelli, L. Wong and E. Andideh, "Optical Pump and Probe Measurement of the Thermal Conductivity of Low- k Dielectric Thin Films", J. Appl. Phys. **92**, 6005 (2002).
- B.C. Daly, H.J. Maris, Y. Tanaka and S. Tamura, "Molecular Dynamics Calculation of the In-Plane Thermal Conductivity of Superlattices", Phys. Rev. **67**, 033308, (2003).
- K. Imamura, Y. Tanaka, N. Nishiguchi, S. Tamura and H.J. Maris, "Molecular Dynamics Calculations of Lattice Thermal Conductivity in Superlattices", J. Phys. C. **15**, 8679 (2003).

- E. Makarona, B.C. Daly, J.-S. Im, H.J. Maris, A.V. Nurmikko and J. Han, "Coherent Generation of 100 GHz Acoustic Phonons by Dynamic Screening of Piezoelectric Fields in AlGaIn/GaN Multilayers", *Appl. Phys. Lett.* **81**, 2791 (2002).
- H.J. Maris, M. Chand, W. Singhomroje, and P. Zannitto, "Studies of Very Small Structures Using Picosecond Ultrasonics", invited paper to appear in the *Proceedings of the 5th World Congress on Ultrasonics*, Paris, September 7-11, 2003.
- D.G. Cahill, W.K. Ford, K.E. Goodson, G.D. Mahan, A. Majumdar, H.J. Maris, R. Merlin and S.R. Phillpot, "Nanoscale Thermal Transport", *J. Appl. Phys.* **93**, 793 (2003).
- L.J. Shelton, F. Yang, W.K. Ford and H.J. Maris, "Picosecond ultrasonic measurement of the velocity of phonons in water", *Physica Status Solidi* **242**, 1379 (2005).
- W. Singhomroje and H.J. Maris, "Generating and Detecting Phonon Solitons in MgO using Picosecond Ultrasonics", *Phys. Rev.* **B69**, 174303 (2004).
- W. Singhomroje and H.J. Maris "Picosecond ultrasonic experiments to study phonon solitons", *Physica Status Solidi* **241**, 3463 (2004).
- S. Tamura, A. Sangu and H.J. Maris, "Anharmonic Scattering of Longitudinal Acoustic Phonons: Herring processes in Tetragonal TeO₂", *Phys. Rev.* **B68**, 014302 (2003).

7. INTERACTIONS/TRANSITIONS

Task #1

- a. Many invited presentations at general and topical meetings such as American Physical Society, Conference on Lasers and Electro-Optics (CLEO), and IEEE LEOS.

Task #2

- a. Conference Presentations

- M.V.Kisin, M.A.Stroscio, G.Belenky, S.Luryi "Interband Phonon Assisted Tunneling in InAs-GaSb Heterostructures" submitted for The Tenth International Conference on Phonon Scattering in Condensed Matter, August 12, 2001, Dartmouth College, Hanover, New Hampshire, USA
- M.V.Kisin, M.A.Stroscio, G.Belenky, S.Luryi "Intersubband Phonon Assisted Transitions in type-II InAs-GaSb Heterostructures" submitted for The Sixth International Conference on Intersubband Transitions in Quantum Wells, September 10, 2001, Asilomar, California, USA
- S. Luryi, L. Asryan, "Temperature insensitive quantum dot laser", International Workshop on Frontiers in Electronics (WOFE), January 6, 2002, St Croix, VI.
- S. Suchalkin, D.Westerfeld, D.Donetski, R.Martinelli, I.Vurgaftman, J.Meyer, S.Luryi, and G.Belenky, "Optical gain and loss in 3 μ m diode W-quantum-well lasers", Photonics West, January 21, 2002, San Jose, California, USA
- D. Westerfeld, S. Suchalkin, M. Kisin, G. Belenky, J. Bruno, R. Tober, "Experimental Study of Optical Gain and Loss in 3.4-3.6 μ m Interband Cascade Lasers", 5th International Conference on Mid-Infrared Optoelectronic Materials and Devices, MIOMD-V, September 2002, Annapolis, USA.

8. NEW DISCOVERIES, INVENTIONS, PATENTS (PENDING)

Task #1

Metal Waveguides for Mode Confinement in Terahertz Lasers and Amplifiers, Qing Hu and Benjamin S. Williams, M.I.T. Case No. 10279 (2003).

Terahertz Lasers and Amplifiers Based on Resonant Optical Phonon Scattering to Achieve Population Inversion, Qing Hu and Benjamin S. Williams, M.I.T. Case No. 10280 (2003).

Terahertz Imaging Devices, Qing Hu and Alan Wei Min Lee, M.I.T. Case No. 11528 (2005).

Task #2

Semiconductor light source with electrically tunable emission wavelength, G.Belenky, J. Bruno, M.V. Kisin, S. Luryi, L. Shterengas, S. Suchalkin, R. Tober, US provisional patent application No 60/602,750 filed 08/19/04, full US Patent application filed Aug 2005.

Widely tunable laser, S. Luryi and M.V. Kisin, US Patent application No. 0/775860, filed 02/10/2004.

Semiconductor laser with reduced temperature sensitivity, L.V.Asryan, S.Luryi, US Pat. 6,870,178, filed Feb 2002, issued March 2005.

Intersubband cascade lasers with enhanced subband depopulation rate, G.L.Belenky, M. Dutta, M.V. Kisin, S. Luryi and M.A. Strossio, US Patent # 6,819,696, filed Sept 2001, issued Nov 2004.

9. HONORS/AWARDS

Task #1

Qing Hu is elected to Fellow of Optical Society of America for "for pioneering contributions to the development of long-wavelength terahertz (THz) quantum-cascade lasers"